Università degli Studi di Firenze
Scuola di Ingegneria
DIEF - Department of Industrial Engineering of Florence

PhD School: *Energetica e Tecnologie Industrali Innovative*
Scientific Area: ING-IND/08 - *Macchine a Fluido*

Film Cooling Modelling for Gas Turbine Nozzles and Blades: Validation and Application

PhD Candidate: Ing. Luca Andrei

Tutor: Prof. Ing. Bruno Facchini

Academic Supervisor: Dr. Ing. Antonio Andreini

Industrial Supervisor: Dr. Ing. Luca Innocenti

PhD School Coordinator: Prof. Ing. Maurizio De Lucia

XXVI PhD School Cycle - 2011-2013

To those who are no longer with us...

Acknowledgements

First of all, I would like to thank Prof. Bruno Facchini to the offered opportunity to study and work under his guidance, his patience and also to have created a wonderful and challenging team.

A very special thank to Antonio, supervisor of this thesis, who during these years has always been the best mentor, ready to give me the wisest advice.

I am sincerely grateful to Luca, the other supervisor, for the chance offered to work with him and for trusting in me during the time we worked together.

Many thanks to present and past colleagues (or I should say friends) of the HTC group: Ale Inno (thank for your whistles!), Alessio, Andrea, the legendary Bonini (and his cigarettes after 7 p.m.!), Carlo, Daniele, Ema, Gianlu (the winter is coming...), Leo, Leopoldo, Maio, Marchino, Riccardo B., Riccardo F., Sabrina, Tommy. A special thank to Lore M. e Lore W.: I'm serious when I say that without you this years would have been more difficult, less enjoyable and certainly without "best papers"!

Where HTC group would be without the "old" guard? So, thanks to the ERGON "guys": Cosimo, Lorenzo, Mirko e Ricca, always ready to support and provide useful advices.

I'm really grateful to my family for their patience and support up to know. I know that I can always rely on you!

If I start thanking all my friend and remembering all the beautiful moments spent together, I think there wouldn't be enough space in these pages... You know you are very special and fundamental for what I have

become.

A special thought to Giacomo, each passing day more a brother than a friend.

A last but (obviously!) not least thank to Martina for helping me to correct my English and for his constant presence by my side. You know you're special to me...

Ci fu una grande battaglia di idee
e alla fine non ci furono né vincitori, né vinti, né idee.
Stefano Benni, Elianto

Abstract

The use of Computational Fluid Dynamics (CFD) for modern turbine blade design requires the accurate representation of the effect of film cooling. However, including complete cooling hole discretization in the computational domain requires a substantial meshing effort and leads to a drastic increase in the computing time. For this reason, many efforts have been made to develop lower order approaches aiming at reducing the number of mesh elements and therefore computational resources. The simplest approach models the set of holes as a uniform coolant injection, but it does not allow an accurate assessment of the interaction between hot gas and coolant. Therefore higher order models have been developed, such as those based on localized mass sources in the region of hole discharge.

It is here proposed an innovative injection film-cooling model (which can be embedded in a CFD code) to represent the effect of cooling holes by adding local source terms at the hole exit in a delimited portion of the domain, avoiding the meshing process of perforations. The goal is to provide a reliable and accurate tool to simulate film-cooled turbine blades and nozzles without having to explicitly mesh the holes.

The validation campaign of the proposed model is composed by two phases. During the first one, results obtained with the film cooling model are compared to experimental data and to numerical results obtained with the full meshing of the cooling holes on a series of test cases, ranging from single row to multi row flat plate, at varying coolant conditions (in terms of blowing and density ratio). Though details of the flow structure downstream of the holes cannot be perfectly captured, this method allows

an accurate prediction of the overall flow and performance modifications induced by the presence of the cooling holes, with a strong agreement to complete hole discretization results. In the second phase, a complete film-cooled vane test case has been studied, in order to consider a real injection system and flow conditions. In this case, film cooling model predictions are compared to an in-house developed correlative approach and full CHT 3D-CFD results.

Finally, a comparison between film cooling model predictions and experimental data was performed on an actual nozzle of a GE Oil & Gas heavy-duty gas turbine as well, in order to prove the feasibility of the procedure.

Contents

List of Figures

List of Tables

Nomenclature

Acronyms

BC	Boundary Condition	
BEM	Boundary Element Method	
BR	Blowing Ratio	[−]
CCT	Conjugate Calculation Technique	
CD	Coefficient of Discharge	[−]
CFD	Computational Fluid Dynamics	
CHT	Conjugate Heat Transfer	
DNS	Direct Numerical Simulations	
DR	Density Ratio	[−]
FC	Film Cooling	
FEM	Finite Element Method	
FVM	Finite Volume Method	
GT	Gas Turbine	
HD	Heavy-Duty	
HT	High turbulence level condition	
JCF	Jet in Crossflow	
LE	Leading Edge	
LES	Large Eddy Simulations	
LT	Low turbulence level condition	
$NHFR$	Net Heat Flux Reduction	[−]
NVA	Normalized Variable Approach	
PS	Pressure side	

PSP	Pressure Sensitivity Paint	
$RANS$	Reynolds-Averaged Navier-Stokes equations	
SGS	Sub Grid Scale	
SH	Shower Head	
SS	Suction Side	
SST	Shear Stress Transport	
$SSTA$	Anisotropic SST	
TE	Trailing Edge	
TL	Two-Layer model	
TLA	Anisotropic TL	
$URANS$	Unsteady RANS	
VR	Velocity ratio	$[-]$
WHL	Steady WHLU	
$WHLU$	Unsteady model by Walters, Holloway and Leylek	

Greeks

α	Perforation angle	$[^\circ]$
α_k	k diffusion coefficient	$[-]$
β	Heat load	$[-]$
β	Local effectiveness location	$[-]$
β_p	Peak effectiveness location	$[-]$
γ	Anisotropic factor	$[-]$
γ	Heat capacity ratio	$[-]$
δ	Kronecker delta	
ε	Turbulent kinetic energy dissipation	$[m^2\ s^{-3}]$
η_{ad}	Adiabatic effectiveness	$[-]$
η_p	Peak η_{ad}	$[-]$
Θ	Dimensionless temperature	$[-]$
λ	Thermal conductivity	$[W\ m^{-1}\ K^{-1}]$
μ	Dynamic viscosity	$[Pa\ s]$
μ_t	Turbulent viscosity	$[Pa\ s]$

ν	Kinematic viscosity	$[m^2\ s^{-1}]$
ρ	Density	$[kg\ m^{-3}]$
τ	Shear stress	$[Pa]$
ϕ	Cooling effectiveness	$[-]$
ω	Turbulence frequency	$[s^{-1}]$

Letters

a	Constant	
A	Area	$[m^2]$
Ax_{Ch}	Axial chord	$[m]$
C_f	Friction coefficient	$[-]$
c_p	Specific heat at constant pressure	$[J\ kg^{-1}\ K^{-1}]$
Cr	Constant	$[-]$
$d,\ D$	Diameter	$[m]$
D_h	Hydraulic diameter	$[m]$
e	Specific internal energy	$[J\ m^3\ kg^{-1}]$
E	Total energy	$[J]$
elm/D	Number of elements per diameter	$[-]$
f	Friction factor	
$h,\ HTC$	Heat transfer coefficient	$[W\ m^{-2}\ K^{-1}]$
I	Momentum flux ratio	$[-]$
k	Turbulent kinetic energy	$[m^2\ s^{-2}]$
k	Thermal conductivity	$[W\ m^{-1}\ K^{-1}]$
Le	Lewis number	$[-]$
l	Perforation length	$[m]$
Ma	Mach number	$[-]$
$\dot{m}$	Mass flow rate	$[kg\ s^{-1}]$
Nu	Nusselt number	$[-]$
p	Pressure	$[Pa]$
P	Pitch	$[m]$
Pr	Prandtl number	$[-]$
$\dot{q}$	Heat flux	$[W]$
R	Gas constant	$[J\ kg^{-1}\ K^{-1}]$

Re_{xy}	Isotropic stram-span	
	Reynolds stress	$[kg\ m^{-1}\ s^{-2}]$
Re	Reynolds number	$[-]$
St	Stanton number	$[-]$
s_x	Streamwise pitch	$[m]$
s_z	Spanwise pitch	$[m]$
$\mathcal{S}_h$	Enthalpy source term	$[kg\ m^{-1}\ s^{-3}]$
$\mathcal{S}_k$	Turbulent kinetic energy source term	$[kg\ m^{-1}\ s^{-3}]$
$\mathcal{S}_{MS}$	Mass source term	$[kg\ m^{-3}\ s^{-1}]$
$\mathcal{S}_u$	Streamwise momentum source term	$[kg\ m^{-2}\ s^{-2}]$
$\mathcal{S}_w$	Spanwise momentum source term	$[kg\ m^{-2}\ s^{-2}]$
t	Time	$[s]$
T	Temperature	$[K]$
Tu	Turbulence intensity	$[-]$
$u,\ v,\ w$	Velocity components	$[m\ s^{-1}\ ]$
V	Velocity magnitude	$[m\ s^{-1}]$
$x,\ y,\ z$	Generic directions	
y^+	Dimensionless wall distance	$[-]$
W	Coolant consumption	$[-]$

Subscripts

ad	Adiabatic
aw	Adiabatic wall
$c,\ cool$	Coolant
ext	External
f	With film cooling
g	Gas
in	Inlet
int	Internal
is	Isentropic
j	Jet
m	Metal
out	Outlet

ref	Reference
s	Surface
t	Turbulent
tot	Total
w	Wall
0	Without film cooling
	Initial
	Total

Superscripts

eq	Equivalent
$'$	Fluctuating

Introduction

The thermal efficiency and specific output of a gas turbine are primarily dependent on two major cycle parameters: the pressure ratio and the turbine inlet temperature [1]. In an ideal Brayton cycle, thermal efficiency increases up to stoichiometric temperatures and high-pressure ratios, without considering losses, particularly, those associated with turbine cooling. Since turbine airfoil materials degrades at temperatures much lower than the stoichiometric temperatures, hot gas-path components, such as turbine airfoils, must be cooled and attention must be given to cycle parasitic losses.

The recognition of material temperature limitations has led to the continuous turbine development programs for cooling technologies, material development, and related multi-disciplinary disciplines of fluid dynamics, heat transfer, aerodynamic performance, and structures, all aimed at the durability of turbine hot-gas-path components. The pursuit of improved turbine materials began long ago when the initial temperature limitations were found to be at about 800° [1]. Following this initial period, an intensive development period took place when nickel-based alloys were developed and characterized as having high creep resistance characteristics. Material improvements relaxed temperature limitations by about 170° [1]. Further development of turbine airfoil manufacturing techniques, such directionally-solidification castings and single-crystal castings led to higher metal temperature capability. More recently, numerous testing evaluations have been conducted to characterize new hot-gas path material super-alloys in terms of tensile, rupture, fatigue, creep,

toughness, corrosion and oxidation resistances, producibility, processing, and other thermophysical properties [2, 3, 4, 5, 6]. Following extensive laboratory testing, actual operating experience is gained with engine testing subject to real operational environments culminating in mature levels of technology readiness levels for production.

Today, many modern turbine airfoils use single crystal superalloys. These are two-phase alloys with a large volume fraction of γ precipitates, based on the intermetallic compound (Ni_3Al), interspersed in a coherent face-centered cubic γ matrix comprised of nickel (Ni), with smaller weight percent of various other elements in solid solution [7]. These elements include: cobalt (Co), aluminum (Al), chromium (Cr), tungsten (W), molybdenum (Mo), tantalum (Ta), hafnium (Hf), rhenium (Re), and ruthenium (Ru). The elements Re and Ru are introduced in the latest generation of single crystal alloys. All these elements have different attributes which can be summarized as follows: Cr, Al, and Hf are used as surface protection elements, Mo, W, and Ta are used in solid solution strengthening, and Re and Ru are used for high creep strength [8].

Two of the most relevant parameters for measuring and assessing cooling performance of turbine airfoils are the *cooling effectiveness* parameter and *heat load* parameter. By definition, the first parameter is a dimensionless temperature ratio of gas-to-metal temperature difference over the gas-to-coolant temperature difference [9]:

$$\phi = \frac{T_g - T_m}{T_g - T_{c,int}} \tag{1}$$

where $T_{c,int}$ is the coolant temperature inside the internal cooling passages of the turbine airfoil. Clearly, if the cooling effectiveness is non-existent, or zero, there is no cooling effect; whereas, if the cooling effectiveness is equal to unity, the airfoil metal and coolant temperature are the same. These two extreme values of either zero or unity are considered as outer limits for cooling effectiveness parameter. In general, the cooling effectiveness lies in-between these two limits and characterizes the cooling circuit performance inside the turbine airfoil.

The other parameter, denoted as the *heat load* parameter, is defined as the ratio of internal heat to the external heat fluxes as follows [9]:

$$\beta = \frac{(m\ c_p)_c}{(h\ A)_g} \tag{2}$$

Figure 1 illustrates cooling effectiveness for typical cooling configurations as a function of heat load parameter simplified here just by the variable in cooling [1]. The cooling effectiveness is naturally a function of many design variables, that is, the cooling configuration, and the coolant ejection requirements. It also a strong function of the amount of cooling medium used, usually measured as percentage of the mainstream gas. As illustrated in Figure 1, the cooling effectiveness increases rapidly with small amounts of coolant. Then, the cooling effectiveness increases monotonically at a lower rate. This implies that for demanding thermal applications, where the thermal load parameter is high, large amounts of coolant may be required. For state-of-the-art engines, turbine cooling air and leakage may be as high as $25 - 30\%$ of engine mainstream flow. In terms of efficiency, and since the cooling air is drawn from the compressor,

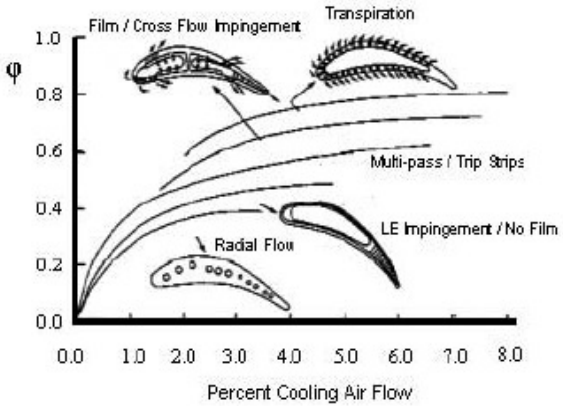

Figure 1: Cooling effectiveness for different cooling schemes (Source [1])

which is driven by the turbine, it represents a direct loss of efficiency. In general, a very approximate rule-of-thumb of 1% cooling air may represent a loss of a fraction of that percentage in specific fuel consumption. This leads to the obvious conclusion that turbine cooling needs to be minimized. Clearly, this is not the only loss mechanism in the engine. Other losses may include mixing and aerodynamic losses, such as profile drag, skin-friction, gas diffusion, secondary flows, tip clearance, boundary-layer separation, shocks, losses due to off-design airfoil incidence angles, trailing edge vortex shedding, and blockage losses [10]. All these losses of engine cycle and turbine efficiencies have to be set against the gains in running the engine at higher turbine inlet temperatures for maintaining required output. Therefore, it is always necessary to reduce and optimize the cooling air requirements for a gas turbine engine design.

In Figure 1, the simplest cooling configuration is characterized by the lowest cooling effectiveness. For instance, the radial cooling holes in the middle of the airfoil cross-section will not permit air to eject from the airfoil walls into the gas mainstream, avoiding film cooling and corresponding ejection mixing losses. However, forced convection through the radial holes may not be sufficient for high thermal load applications, and even at low thermal loads, this simple cooling arrangement is likely to induce high temperature gradients between the airfoil surface and the cooling hole locations. An improved cooling arrangement over the radial cooling hole arrangement is the multi-pass serpentine cooling configuration. In serpentine cooling arrangements, coolant enters the airfoil through the blade root inlet; passes though multiple circuits, cooling the mid-body of the airfoil before ejecting out of the airfoil through main body film holes or trailing edge slots. The leading edge, with high thermal loads, may be cooled with dedicated cooling circuits. If the leading edge and the mid-body circuits are combined and coupled together, one can refer to these arrangements as *cold-bridge* or *warm-bridge* designs depending on the feed source. If the feed coolant comes from the mid-body with freshly supplied coolant, we have a cold-bridge cooling design; whereas, if the feed comes from the mid-body with warmed coolant, naturally after heat pick-up from

the mid-body serpentine arrangement, we have a warm-bridge cooling design. Since the serpentine cooling circuits have large wet perimeters in the turbine airfoil cross-section, it is possible to introduce rips on the airfoil internal wall to promote turbulence and enhance internal coolant heat pick-up. Many rip configurations have been designed throughout the years of cooling technology development. These include normal rips, skewed rips, and angled *chevron* rips with different orientations relative to the flow, different rip heights, different height-to-pitch ratios, different relative positioning with respect to each other, either in a staggered or in-line arrangements. These different arrangements lead to different heat transfer characteristics enhancing heat pick-up by the coolant flowing in the serpentine passages tailored to minimize the effects of local external heat loads.

Further cooling improvements are obtained by the introduction of peripherally cooled airfoil designs. Peripheral cooling circuits are basically an array of vortex generators, designed to produce sustained longitudinal vortices in the bulk flow and thereby promote a global mixing capability in the cooling channel [11]. In addition, the coolant can be ejected at many points around the surface of the airfoil. This concept leads to an increase of convective cooling efficiency by means of cooling circuits. This new parameter can also be regarded as a dimensionless temperature ratio of the difference between the exit coolant to inlet coolant temperatures relative to the difference of metal to coolant inlet temperatures [9]:

$$\eta_c = \frac{T_{c,out} - T_{c,in}}{T_m - T_{c,in}} \tag{3}$$

If this ratio is non-existent, or zero, it is implied that exit coolant temperature and inlet temperature are the same, and thus, no heat pick-up in the circuit. If the ratio is unity, then the exit coolant temperature and the metal temperature are the same. In this case, it is said that the cooling circuit is 100% efficient convectively. In general, serpentine cooling may be in the order of $15 - 30\%$ efficient. However, dedicated airfoil peripheral cooling may be $30 - 60\%$ efficient. This is about $2\times$ the

convective efficiency values of typical serpentine cooling.

In addition to the improved convective characteristics, film cooling can be used in many points of the airfoil. The *film effectiveness* or *adiabatic effectiveness* is also a dimensionless parameter defined as [12]:

$$\eta_{ad} = \frac{T_g - T_{ad}}{T_g - T_{c,out}} \tag{4}$$

The overall cooling effectiveness, being a function of both the convective and film cooling effectiveness, can be optimized for any cooling arrangement. If the film exit shape is optimized to cover the airfoil as much as practical, one can obtain overall cooling effectiveness up even to 75% with film coverage and convective efficiency in excess of 50% [11]. Simply stated, the peripheral airfoil circuits will pick-up heat by convection in a very effective manner and then eject from film openings with high coverage designs to further reduce the thermal load to the part.

Regarding the different cooling schemes, peripheral cooling and conventional serpentine cooling arrangements may include several internal design features for augmenting internal heat transfer. These internal features may be small posts connected to both sides of the coolant passage, as pedestals, or may project to only about half of the coolant passage, as pin-fins [13, 14]. Fundamentally, both features act in a similar manner, by turbulating coolant flow field and by exposing more surface area to the coolant. These synergistic cooling effects lead to higher internal heat transfer coefficients, which can be regarded as a measure of heat pick-up by the coolant. It should also be noted that there are conduction paths integrated directly with the walls of the airfoil for further cooling. The disadvantage of such augmentation devices is that they increase the coolant flow blockage, which in turn increases the coolant pressure drop. Since the coolant supply pressure may be limited, attention must be given to these blockage effects so as to assure sufficient pressure at the film openings and overcome external gas pressure. The internal-to-external pressure ratio is usually referred to as the *back-flow-margin* with minimum values established for the leading edge and mid-body of the airfoil. On the other hand,

if the internal coolant pressure is much higher than the external pressure at the film exits, then the film jets may actually penetrate through the external boundary layer setting out "blow-off" conditions. Blowing the coolant out nearly normal to the airfoil surface with high velocity is likely to lift the coolant right off the blade and allow the hot mainstream gas to move below the coolant jets making contact with the airfoil surface. This is an adverse film effect that needs to be prevented. To prevent blow-off conditions, the geometrical attributes of film openings need to reduce the ejection velocity by introducing cooling hole shapes, angles, tapering, or diffusion zones while maintaining a high degree of cooling hole filling [15]. Externally in the main flow field, a mismatch between the gas mainstream and the coolant jet velocities will give rise to mixing losses. In this way, film ejection may rip or further energize the external boundary layer; thus, increasing the external heat transfer coefficient or thermal load to the part.

Figures 2 and 3 illustrate typical airfoil cooling schemes. Typically, for the first vane, the coolant is fed into the casing plenum chamber, and from there into the leading edge impingement baffle. From the leading edge baffle, the coolant impinges on the leading edge target surface and is ejected into the external gas-path through several close-spaced rows of holes known generally as showerhead holes. For this component, the

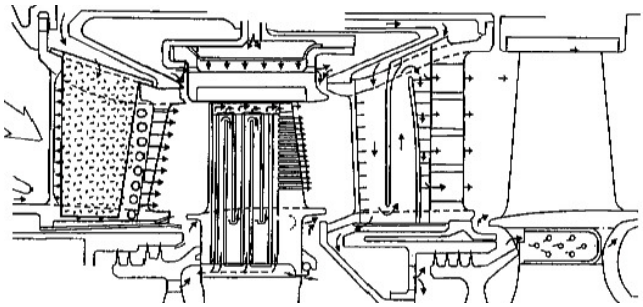

Figure 2: Typical airfoil cooling schemes for a two-stage high pressure turbine (Source [1])

highest temperature occurs at the leading edge where the stagnation point is located [17]. The balance of the coolant flow in this vane will pass through a small gap between the baffle and the internal wall of the airfoil leading to other film holes or slots in the main body or trailing edge. Note that internal cooling is done by convective and impingement cooling. At the trailing edge pedestals may be placed to enhance internal cooling, heat pick-up, and decrease the metal temperature [18]. The first blade shown in Figure 3 is only an example of a wide variety of serpentine cooling configurations. Stators and rotor blades of downstream stages will often have multi-pass cooling of the type shown in Figure 2. The coolant flow is led through a series of serpentine passages and makes several passes along the span before finally ejecting at the trailing edge.

The purpose of turbine cooling is solely justified by the need to have turbine components withstand adverse environments while maintaining life targets. Lifting and durability of airfoils require a synthesis of mission cycle, range of operating conditions and time spent at each condition, including the number of transients between conditions. Overall cooling effectiveness is a function of the design, which is reflected by two other

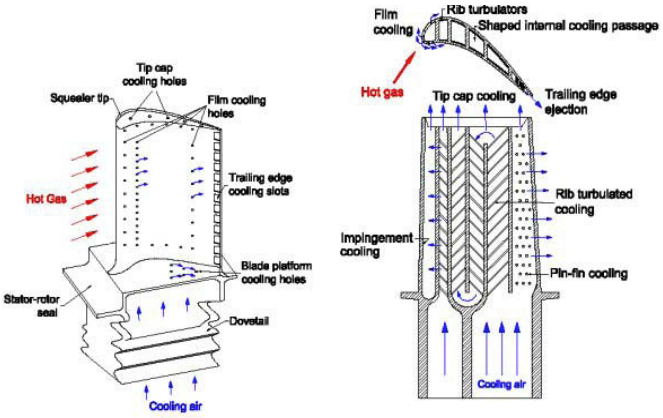

Figure 3: Typical blade cooling schemes (Source [16])

relevant parameters: the convective efficiency and the film effectiveness. The overall cooling effectiveness should balance the external heat load to the part. In turn, all cooling parameters need to be balanced with their effects of aerodynamic and cycle performance. For blades, the mechanical load, due to centrifugal effects, need to be determined in conjunction with the blade bulk metal temperature distributions to evaluate its creep capability.

Research objectives

The obvious requirement for the design process of film-cooled components is a predictive capability for film-cooled surface temperature and adiabatic effectiveness values with high level of confidence. In the framework of CFD, this has to be achieved with manageable computational effort. Fully resolving the film cooling flows, is theoretically possible, but is not feasible in a design environment from an economical standpoint. The development of a method to simulate film cooling flows in 3D-CFD without having to fully resolve the flow inside the cooling holes promises to mitigate this issue.

This work presents a film cooling model able to simulate coolant flows ejected from cylindrical cooling holes in three-dimensional CFD without meshing the cooling hole geometry. The model is exploited to evaluate adiabatic effectiveness. Coolant proprieties inputs are evaluated by external tools, such as correlative approaches, usually employed in preliminary design process. Adding constant source terms to the transport equations for mass, momentum and energy locally in the space occupied by the evolving jet, the model of film-jet is imposed onto 3D-CFD simulation. These source terms are specified in the proximity of the film hole exit inside a predefined injection volume. The influence of hole discretization (in terms of number of elements per diameter exploited during the mesh creation) has been studied. The developed model is intended to be a flexible tool to be used during both the preliminary and detailed analysis phase, combining flexibility (typical of the preliminary design phase) with

accuracy (request during detailed analysis phase). The model has been implemented in a commercial CFD code.

In order to assess the accuracy of the proposed model, a complete validation campaign has been conducted: considered test cases comprehend varying cooling geometry (single and multi row flat plate, vane) at different coolant conditions (in terms of blowing and density ratios). Reference values are retrieved from complete hole discretization 3D-CFD, full CHT 3D-CFD, correlative approach and experimental data. The model proved itself to be a reliable tool, predicting with a high level of accuracy the correspondent complete hole study results.

Finally, the proposed film cooling model has been exploited to study a real heavy-duty gas turbine nozzle. Results are compared against PSP measurements and correlative approach, confirming its capability to estimate adiabatic effectiveness, even in a complex real case, simulating 500 injection holes.

Thesis outline

The present thesis is structured as follows.

Chapter 1 presents the film cooling technique. In the first part, main features of this technique are reported, focusing on influence of coolant conditions on film cooling performance. The last part concentrates on the physics of a jet in cross-flow.

Chapter 2 reports a full numerical analysis of typical film cooling applications at a wide range of working conditions. In particular, it is presented a complete review of unconventional models proposed in literature and a benchmark their predicting capability against each other and standard turbulence models.

Chapter 3 focuses on the description of the proposed Film Cooling Model (*FCM*) developed to simulate coolant flows ejected from cylindrical cooling holes in three-dimensional CFD without meshing the cooling

hole geometry. A review of film cooling models available in literature is presented. Finally, the model implementation inside a commercial CFD code is presented along its main features.

Chapter 4 shows application and validation of the presented *FCM* on film-cooled flat plates under different coolant conditions. Studied test cases comprehend a single row and a multi-rows flat plate. Comparisons against experimental data and complete 3D-CFD predictions are conducted in terms of both adiabatic effectiveness distributions and profiles.

Chapter 5 is composed by two parts. In the first one, an in-house developed correlative approach aimed to predict cooling performances and metal temperatures of gas turbine blades and nozzles is presented. In the second one, the comparison of *FCM*, correlative approach and fully CHT 3D-CFD application to a laboratory test case is presented.

Chapter 6 presents the application of the model to a real case: an actual nozzle of a GE Oil & Gas heavy-duty gas turbine. Results of *FCM* application will be compared against detailed experimental data and *BANKS-3D* predictions in terms of adiabatic effectiveness profiles along the airfoil and endwalls.

Chapter 1

Film cooling technique

> Film Cooling is the introduction of a secondary fluid (coolant or injected fluid) at one or more discrete locations along a surface exposed to a high temperature environment to protect that surface not only in the immediate region of injection but also in the downstream region (Goldstein, 1971).

1.1 Film cooling generalities

Film cooling is a major component of the overall cooling of turbine airfoils. An example of a film cooled turbine vane is shown in Figure 1.1: it is evident that there are holes placed in the body of the airfoil to allow coolant to pass from the internal cavity to the external surface. The ejection of coolant gas through holes in the airfoil body results in a layer or *film* of coolant gas flowing along the external surface of the airfoil. Hence the term *film cooling* is used to describe the cooling technique. Since this coolant gas is at a lower temperature than the mainstream, the heat transfer into the airfoil is reduced. The adiabatic film has a predominant effect in the design of the overall airfoil cooling.

The primary process by which film cooling reduces the heat transfer to the wall is by reducing the gas temperature near the wall, i.e. reducing the driving temperature potential for heat transfer to the wall. As the

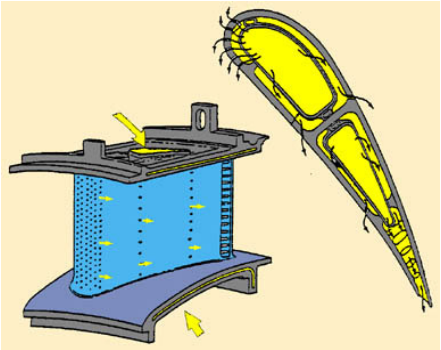

Figure 1.1: Schematic of film cooling configurations on a vane (Source `http://lttwww.epfl.ch/research/htprojects/filmcool.htm`*)*

coolant flows from the coolant holes, it mixes with the mainstream gas resulting in an increase in coolant temperature. A typical example of this is presented in Figure 1.2 which shows measurements of the temperature profile along the centerline of a coolant jet as it flows downstream of the coolant hole. In this figure the temperature contours are presented as normalized Θ contours where Θ is defined as:

$$\Theta = \frac{T_\infty - T}{T_\infty - T_c} \tag{1.1}$$

where T is the local temperature, T_∞ is the mainstream temperature and T_c is the coolant temperature at the exit of the hole. Note that $\Theta = 1$ is the normalized initial coolant temperature and $\Theta = 0$ is the normalized mainstream temperature. Looking at Figure 1.2, the Θ contours show that coolant quickly increases in temperature as it flows downstream. The coolant temperature at the wall is the adiabatic wall temperature (T_{ad}) and this temperature is generally assumed to be the driving temperature potential for heat transfer into the wall.

Generally a normalized form of T_{ad}, referred to as the *adiabatic effectiveness* or *film effectiveness* (Equation 4), is used to characterize the film

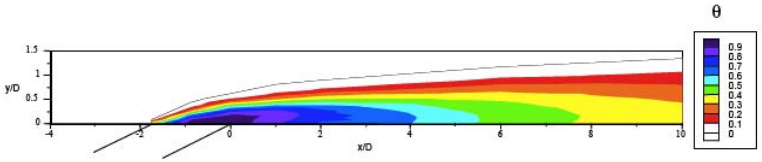

Figure 1.2: Contours of Θ showing the coolant distribution flowing from a film cooling hole (Source [19])

cooling performance (Figure 1.3). For perfect film cooling performance, the adiabatic effectiveness would have a value of 1, i.e. T_{ad} would be equal to the coolant temperature at the exit of the hole. However, a $\eta_{ad} = 0$ would indicate that film cooling has not reduced the gas temperature at the wall. In practice, η_{ad} tends to decrease quickly downstream of the coolant holes due to the strong turbulent dispersion of the coolant jet.

Generally, the adiabatic wall temperature is presumed to be the to be the driving temperature potential for heat transfer into the wall. Consequently, the heat flux into the wall with film cooling ($\dot{q}_f$), is determined using the heat transfer coefficient with film cooling (h_f), defined as:

$$h_f = \frac{\dot{q}_f}{T_{ad} - T_w} \tag{1.2}$$

To evaluate the film cooling performance in reducing the heat flux to the wall, $\dot{q}_f$ should be compared to the local heat flux to the wall that would occur without film cooling ($\dot{q}_0$), determined based on the heat transfer coefficient without film cooling (h_0), as:

$$\dot{q}_0 = h_0 \left(T_\infty - T_w\right) \tag{1.3}$$

It appears that a reduced temperature value for T_{ad} relative to T_∞ will result in a reduced heat flux to the wall. However, these equations also highlight that there is potentially a difference in heat transfer coefficient for the film cooling case and the no-film cooling case. In fact, the disturbance caused by the injection of coolant often causes an increase

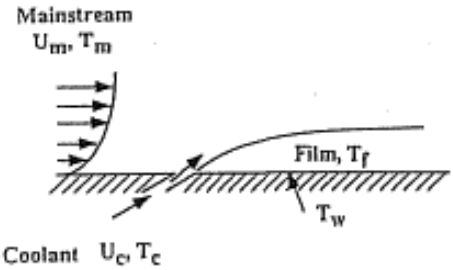

Figure 1.3: Schematic of film cooling concepts and its driving temperatures (Source [20])

in the heat transfer coefficient. This increase in heat transfer coefficient causes an increase in heat transfer to the wall, and hence is detrimental. Consequently the overall performance of the film cooling configuration needs to be evaluated in terms of the a net heat flux reduction (Δq_r) which takes into account decreased gas temperature provided by the coolant film and the increased heat transfer coefficient due to the coolant injection process. The net heat flux reduction is obtained combining Equations 1.2 and 1.3 in:

$$NHFR = 1 - \frac{h_f}{h_0}\left(1 - \frac{\eta_{ad}}{\phi}\right) \tag{1.4}$$

where ϕ is the dimensionless metal temperature for the operational turbine airfoil (Equation 1). Note that ϕ is an unknown quantity that is not generally determined by experiments, and a value for ϕ must be assumed in order to estimate a net heat flux reduction using Equation 1.4. A typical value for operational film cooled turbine airfoils is $\phi = 0.6$, and this value is generally assumed when analysing laboratory data.

1.2 Main geometric and fluid dynamic parameters

The characteristics and performance of film cooling are determined by several of geometric and fluid dynamic parameters.

The main geometric parameters are:

- the length of the holes;
- the pitch of the holes in the same row S_y (span-wise) and between two subsequent rows S_x (stream-wise);
- the hole inclination angle relative to the crossflow direction;
- perforated area (number of rows).

Regarding the inclination of the holes, it must be observed that exploiting inclined holes, instead of normal holes, for same values of airfoil thickness, it is possible to increase the internal surface, and thereby the heat transfer, promoting also the formation of a layer of film along the surface caused by the less jet penetration in the crossflow (and hence enhancing the adiabatic effectiveness).

Film cooling technique also depends on several *fluid dynamic* parameters that influence the main stream and the coolant flow. It is possible to take into account of these parameters defining several dimensionless parameters, like the *Blowing Ratio*, defined as:

$$BR = \frac{(\rho V)_c}{(\rho V)_g}, \tag{1.5}$$

the *Momentum Flux Ratio*:

$$I = \frac{(\rho V)_c^2}{(\rho V)_g^2}, \tag{1.6}$$

the *Density Ratio*:

$$DR = \frac{\rho_c}{\rho_g}, \tag{1.7}$$

and the *Velocity Ratio*:

$$VR = \frac{V_c}{V_g}. \tag{1.8}$$

The effect of these parameters on cooling system performances was, is and will be the object of many investigations. The large number of parameters and their non-linear interactions in affecting the cooling system working conditions, makes film cooling study a quite difficult

matter. Usually, in order to make the subject affordable, each author focuses on a subset of parameters and investigates their influence in a defined variation range. Generally, the most influencing parameter is the *blowing ratio*, representing the jet momentum augmentation compared to the main flow momentum, for constant DR values.

Another parameter that plays an important role, is the *jet Reynolds number*, defined as:

$$Re_j = \frac{\rho_c V_c D}{\mu_c} \tag{1.9}$$

Pressure losses through the holes and heat transfer within the hole depend on Re_j. Usually, an Re_j augmentation involves an increase of the two parameters: it is evident that the first parameter negatively affects the performance of the cooling system, while the second one is a desired effect.

1.2.1 L'Ecuyer and Soechting's classification

L'Ecuyer and Soechting [21] examined the trends from data presented by Pedersen et al. [22]. They defined three regimes to characterize the adiabatic film effectiveness distribution on a flat plate:

- mass addition regime: $\overline{\eta}_{aw}$ increases with BR due to increased thermal capacity of the coolant, but the effectiveness is independent of the density ratio and velocity ratio parameters;
- mixing regime: $\overline{\eta}_{aw}$ distribution depends on BR and DR due to opposing influence of increased thermal capacity and increased coolant/free stream mixing and penetration;
- penetration regime: $\overline{\eta}_{aw}$ distribution is completely dominated by a complex interaction of excessive coolant penetration and augmented turbulent diffusivity and turbulent diffusion of the coolant thermal effect toward the surface.

Based on Pedersen et al. [22] data, for angle of injection $\alpha = 35°$, $P/d = 3$, and for a single row of holes:

- mass addition regime: $VR < 0.25$;

- mixing regime: $0.25 < VR < 0.8$;
- penetration regime: $VR > 0.8$.

1.3 Film cooling performance

The primary measure of film cooling performance is the adiabatic effectiveness, η_{ad} (Equation 4), since it has a dominating effect on the net heat flux reduction. Furthermore, industrial designers typically will focus on the laterally averaged adiabatic effectiveness, $\overline{\eta}_{ad}$, which is the average η_{ad} over a line normal to the flow and extending a distance equal to the pitch between holes.

Besides the simplification in processing adiabatic effectiveness results by using only laterally averaged data, there is a physical rationale for using only the laterally averaged film effectiveness. Remembering that η_{ad} represents the normalized adiabatic wall temperature which corresponds to the gas temperature adjacent to the surface. As the coolant jet flows downstream of the coolant hole there is a large spatial variation of gas temperature near the wall as is evident by the contour plots of η_{ad} shown in Figure 1.4. However the large conductivity of the metal turbine airfoil causes a much more uniform distribution of the *metal temperature*. Consequently the laterally averaged adiabatic effectiveness is a reasonable representation of the effect of the coolant jet [24]. However, it should be recognized that for purposes of understanding the physical processes of coolant dispersion, and for validation and improvement of computational predictions, the spatial distribution of η_{ad} is important information.

Ideally a film of coolant would be introduced to the surface of an airfoil using a slot angled almost tangential to the surface in order to provide a uniform layer of coolant that remain attached to the surface. However, long slots in the airfoil would seriously reduce the structural strength of the airfoil, and hence are not feasible. Consequently coolant is typically introduced to the airfoil surface using rows of holes. The film cooling performance is dependent on the hole geometry and configuration of the layout of the holes. Furthermore, various factors associated with the

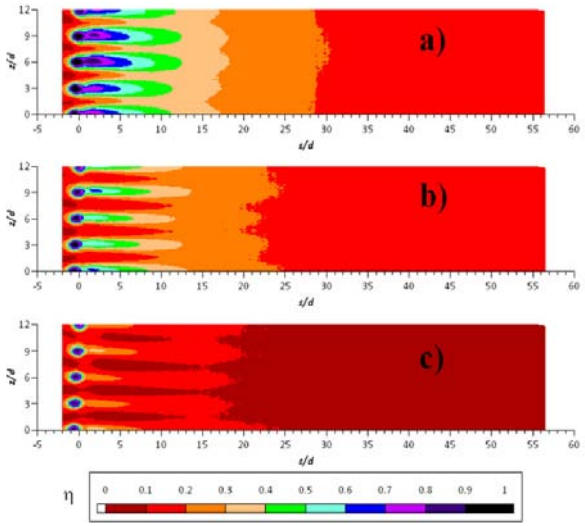

Figure 1.4: Typical airfoil adiabatic effectiveness distribution for various coolant conditions (Source [23])

Table 1.1: Factor affecting film cooling performances (Source [19])

Coolant/Gas conditions	**Hole geometry and configuration**	**Airfioil/Endwall geometry**
Mass flux ratio	Hole shape	Leading edge Main body
Momentum flux ratio	Injection and compound angles of perforation	Blade tip Endwall
Mainstream turbulence	Spacing between holes	Surface curvature
Density ratio	Hole length	Surface roughness
Approach boundary layer	Spacing between rows and number of rows	
Mainstream Mach number		
Unsteady mainstream flow		
Rotation		

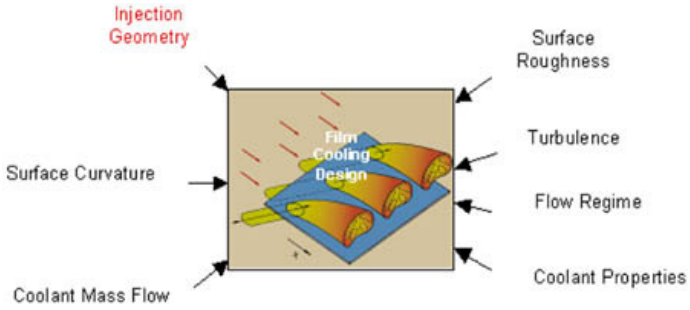

Figure 1.5: Film cooling design and parameters (Source `http://lttwww.epfl.ch/research/htprojects/filmcool.htm`*)*

coolant and mainstream flows, and the airfoil geometry, also significantly affect the cooling performance. A listing of the various factors influencing film cooling performance is presented in Table 1.1: considering the many listed factors, the difficulty in predicting film cooling performance is evident. In Figure 1.5, film cooling design parameters are depicted.

1.3.1 Influence of blowing ratio

A comprehensive study of the adiabatic effectiveness was done by Baldauf et al. [25] using a flat, smooth surface test facility. They made a study on adiabatic film cooling effectiveness at varying blowing ratios (BR) and momentum ratio (I) for a geometry of cylindrical holes with $S_x/d = 3$, inclined 30° to the surface and aligned in the flow direction. Results for blowing ratios from 0.2 to 2.5 are presented in Figure 1.6.

Figure 1.6 shows that the level of $\overline{\eta}$ increases systematically with BR until $BR = 0.6$; then for $BR \geq 0.85$, the peak level of $\overline{\eta}$ begins to decrease, and the position of the peak moves downstream. The initial increase in $\overline{\eta}$ with increasing BR is expected due to the greater mass flow of coolant. The decrease in $\overline{\eta}$ for $BR \geq 0.85$ is due to the coolant jet separating from the surface. This is graphically illustrated in the sequence of thermal profile measurements presented in Figure 1.7 (retrieved from [26]) where is

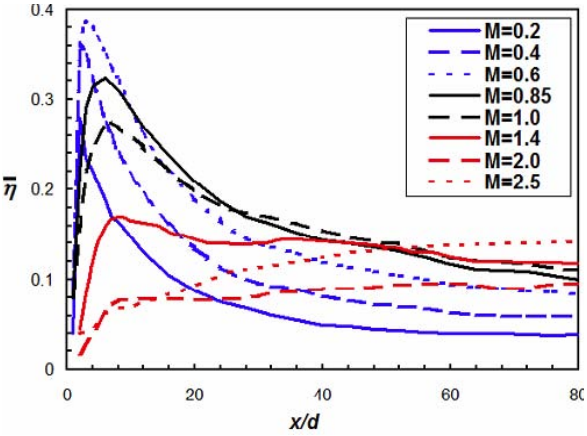

Figure 1.6: Distributions of η_{ad} for varying blowing ratios presented as a function of the streamwise distance x/d (Source [25])

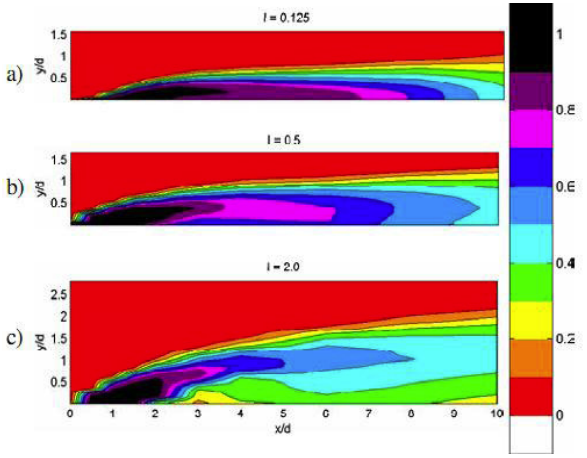

Figure 1.7: Thermal profiles showing three states of coolant jets: attached, detached then reattached, and fully detached (Source [26])

shown the non-dimensional temperature along the centerline of a coolant jet exiting a cylindrical coolant hole inclined 35° to the surface for three different momentum ratio I.

The three profiles presented in Figure 1.7 represent three different states for the coolant jets: (a) fully attached coolant jets, (b) coolant jets that detached and then reattached downstream and (c) coolant jets that were fully detached. Clearly as the coolant jets begin to detach, the coolant temperature at the wall decreases as the core of the coolant jet travels above the surface. The range of momentum flux ratios for each of these flow states was found to be $I < 0.4$ for fully attached jets, $0.4 < I < 0.8$ for detached/reattached jets, and $I > 0.8$ for fully detached jets for flat surface flows. Clearly, whether or not the coolant jets are attached strongly affects the cooling performance.

1.3.2 Influence of density ratio

Typically the coolant to mainstream density ratio for engine conditions is $DR \approx 2$, but often experimental measurements of film cooling performance are conducted with density ratios that are much smaller, even with $DR \approx 1$. Because of this range of density ratios used in testing, it is valuable to understand how the coolant density ratio affects film cooling performance. When testing with lower density ratios, coolant flows at a given mass flux ratio will have higher velocity and momentum flux ratios. Recall that coolant jet separation is primarily a function of momentum flux ratio, so lower density coolant jets will tend to separate before higher density ratio jets. Consequently the maximum film effectiveness for lower density ratio coolant jets is less than for the higher density ratio jets, but the difference in film effectiveness levels is generally small.

For example, Sinha et al. [27], Pedersen et al. [22], and Baldauf et al. [25] found that the maximum laterally averaged film effectiveness was nominally 20% higher for coolant $DR \approx 2$ compared to $DR \approx 1.2$ near the hole ($x/d < 20$) but was essentially the same farther downstream. These tests were for smooth, flat surfaces. Tests for a vane leading edge, pressure side and highly curved suction side showed similar film effectiveness for

low and high density coolant, but the low density ratio coolant has 10% lower adiabatic effectiveness in some cases [28, 29].

1.3.3 Influence of curvature

Surface curvature has been shown by several authors to affect film cooling effectiveness. The results show that, compared to flat plate results, there is decreased film cooing effectiveness on the pressure or concave surface, while on the suction or convex surface there is increased film cooling effectiveness [31]. While the data of Mayle et al. [30], and Ito et al. [32] show similar trends in their results, the implicit corrections to apply for curvature effects are significantly different. The results presented by Mayle et al. [30] have been normalized by their flat plate results, and are shown in Figure 1.8. It was found that a reasonable, but probably over simplified, model to account for curvature effects was to decrease pressure surface effectiveness by 20%, and to increase suction surface effectiveness by 20%. The results in Figure 1.8a show a decrease in the ratio with down stream distance. The downstream distance, x/d is not expected to exceed 150. Close to the cooling hole a 20% reduction in effectiveness exceeds that seen in the data. Further downstream this reduction agrees with the data, especially if the data for a blowing ratio of 0.7 is adjusted downward to give a value of one at $x/d = 0$. For the suction surface the data show

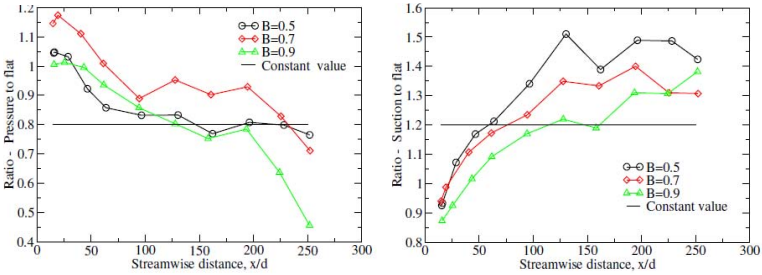

(a) Pressure side *(b) Suction side*

Figure 1.8: Change in η_{ad} due to curvature (Source [30])

a ratio less than one close to the film cooling hole, but a steady rise in the ratio with downstream distance. At far downstream distances the data show an effect of blowing ratio. The higher the blowing ratio (B in Figure 1.8) the lower the slope shown in Figure 1.8b. Because of limited coolant supply total pressures and coolant hole discharge coefficients in the range of 0.6 to 0.8, high blowing ratios are not expected for the first stage turbine vane.

Ito et al. [32] compared the effects of curvature at a constant blowing ratio, but with varying values of the momentum ratio, I. Variations in I at constant BR were achieved by varying the density ratio ρ_c/ρ_g. Figure 1.9 shows results from Ito et al. [32], and the trends in the data differ significantly from those of Mayle et al. [30]. For the pressure surface, the reduction in adiabatic effectiveness is much greater than 20%, except for the first measurement station, close to the hole. For the suction surface momentum ratios of 1/6 and 1/8, corresponding to density ratios of 1.5 and 2.0, show an increase in η_{ad} due to curvature of about 40%. This increase is almost independent of streamwise distance. For the pressure surface there is a large decrease in adiabatic effectiveness, which again is almost independent of streamwise distance. In contrast to the results of Mayle et al. [30], here the 20% adjustment due to curvature is almost always less than is seen in the data.

The data show that, for practical high pressure turbine vanes, the

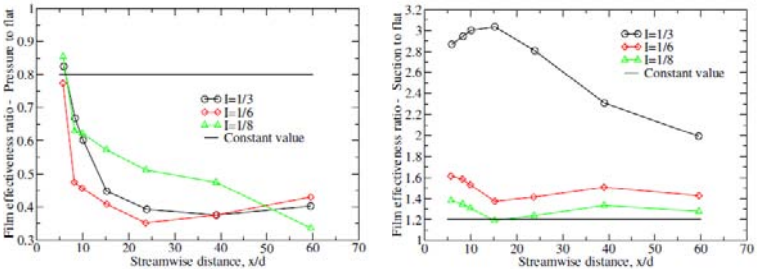

(a) Pressure side *(b) Suction side*

Figure 1.9: Change in η_{ad} due to curvature (Source [32])

blowing and momentum ratios are in regions where suction surface curvature augments η_{ad}, and pressure surface curvature causes η_{ad} to decrease. Further complicating any modelling approach is that the curvature of turbine blades is not constant. To account for curvature effects on a first order basis, Boyle and Ameri [31] suggested to decrease pressure surface effectiveness by 20%, and increase suction surface effectiveness by 20%. On the other hand, at any inlet turbulence intensity the local turbulence intensity at cooling holes on the suction surface is much lower than the turbulence intensity on the pressure surface. Consequently, the effects of inlet turbulence are more strongly felt on the pressure surface. The effects of curvature are to further decrease pressure surface film effectiveness.

1.3.4 Influence of film cooling on heat transfer

In the open literature, studies about the influence of film cooling on heat transfer. Regarding this aspect, the physical basis of the problem was firstly analysed by Goldstein and Taylor [33]. More recently, Baldauf et al. [25] carried out an extensive experimental campaign from which a correlation for the augmentation factor due to the coolant injection was derived. Andreini et al. [34] investigated adiabatic and overall effectiveness of effusion cooling plates at different operating conditions, obtaining indirectly the heat transfer increase for different inclination angles as a function of blowing ratio. A more general review of the flow physics that takes place on the hot side of film cooling plates is provided by Han et al. [20].

Baldauf et al. [35] studied the influence of the main geometrical parameters on fluid dynamics heat transfer coefficient for one row of holes. It should be noted that in Figure 1.10, density ratio is called P and blowing ratio M. As expected, the increase of blowing ratio increases HTC values. Referring to Figure 1.10a, for values of blowing ratio less than 0.85, jet remains essentially stuck to the surface giving little increments of the heat transfer coefficient than those obtained without film (h_0). The maximum heat transfer coefficient is reached in the area between $10 < x/D < 30$, where the film separates from the surface. The maximum increase of h_f

is 25% and is on the mostly tested blowing ratio value ($M = 2.5$).

Results of the same geometrical configuration at a typical low density ratio of 1.2 are shown in Figure 1.10a. In general, the downstream distributions of the heat transfer coefficient have a similar characteristic as for the engine like high density ratio case $DR = 1.8$ (Figure 1.10b). However, the severe augmentation of the heat transfer at higher blowing rates extends further downstream, covering the whole examined test surface. The values range up to a 30% augmentation for the highest blowing rate of 2.5. At short downstream distances, low blowing rates exhibit a reduction of the heat transfer coefficients below the unblown level. The coolant jet impact on the surface seems less intense than in the high density ratio case. Even less convection than from the unblown reference seems possible because of the low coolant velocity.

1.4 Jet in crossflow

The physics of the flow developed in the film cooling is determined by the interaction of the cold jets, coming out from the holes, with the mainstream hot flow. This interaction creates, in the zones immediately downstream of the jets, a flow field characterized by an array of large scale vortical structures. All these structures are inherently unsteady and

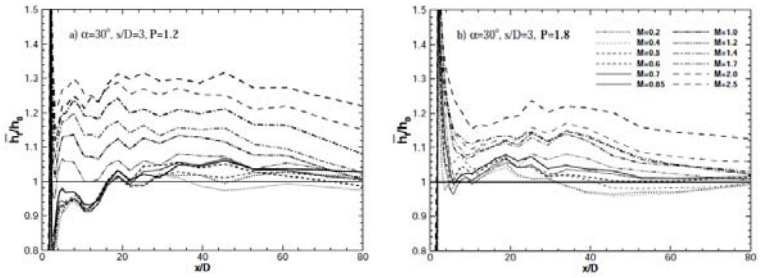

(a) Hole simmetry plane. *(b) Section normal to the hole.*

Figure 1.10: Effect of BR and DR on the heat transfer augmentation (Source [35])

anisotropic [36].

The principal structures of vortices are (Figure 1.11):

- jet shear-layer vortices;
- horse-shoe vortex;
- counter-rotating vortex pair (CRVP);
- wake vortices.

The jet shear-layer vortices dominate the initial portion of the jet and they are the results of the instability in the annular layer close to the plate. This layer is subjected to shear stress and tends to separate at the hole exit, leading to the formation of ring vortices around the jet: these vortices are transported downstream with the jet.

The horseshoe vortices born upstream of the hole leading edge and the jet shear-layer vortices. The formation of these flow structures is similar to the one observed upstream of a solid obstacle, such as a cylinder or an airfoil leading-edge. In fact, when the boundary layer meets an obstacle (of any kind), an adverse pressure gradient is generated, leading to the formation of the horseshoe vortices.

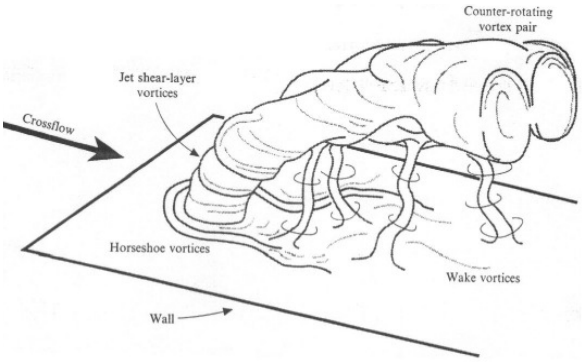

Figure 1.11: Jet in the crossflow structures (Source [36])

The counter-rotating vortex pair (CRVP) develops in the area immediately downstream of the jet and becomes dominant in the regions far from injection. These flow structures have a great influence in the film cooling problem, since they are responsible for the mixing between the jet and the crossflow: this interaction creates a lateral spreading of the jet and hence a better protection of the wall. In fact, the CRVP orientation tends to promote the lifting of the jet, generating a zone where the hot gases can get through (Figure 1.11). Although the presence of CRVP is widely documented in literature, there is not a unique and universally recognized discussion about the causes of its formation. Moreover, each structures of motion, including the CRVP, are strongly affected by the present physical conditions and it is conceivable that different mechanisms may contribute in several ways and different operating conditions to their formation. The most important theories about the formation of CRVP are presented by Andreopulos [37] and by Walters and Leylek [38]. In Figure 1.12, typical flow structures developed inside the hole and at the hole exit are depicted.

The wake vortices are flow structures where the mean component of vorticity is directed normal to the plate. These vortices are characterized

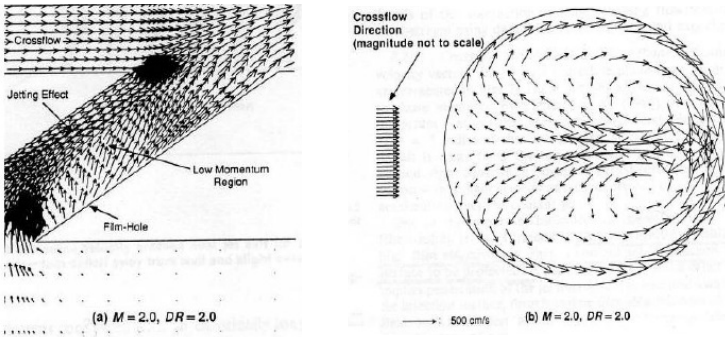

(a) Hole symmetry plane. *(b) Section normal to the hole.*

Figure 1.12: Coolant flow inside the hole (Source [39])

by an evident unsteadiness and by the typical mechanism of vortex shedding. Experimental investigations by Fric and Roshko [40] show that the wake vortex formation is caused by separation events taking place in the boundary layer of the plate immediately behind the jet (Figure 1.13). Their investigations show that the two components of the crossflow, that go around the jet, crash behind it leading to the formation of separation bubbles. These vortices are then lifted by the jet and dragged downstream. The formation of the wake vortex is therefore affected by the main jet lifting.

The jet penetration into the free-stream depends mainly on the injection angle and on the local coolant to free-stream velocity ratio. At large angles and velocity ratios (Figure 1.13b), the jet lifts off. For lower values (Figure 1.13a) the jet bends over quickly and attaches to the wall. After the completion of the jet bending, pressure forces are small and the jet follows the local flow. As soon as the coolant exits the hole, turbulent mixing processes cause the coolant mixing with the free-stream. Neighbouring jets can merge giving a blanket of coolant at some distance downstream; the distance is dependent on the jet spacing. Similarly, coolant from an upstream row of jets can help to form a blanket of coolant, depending on the spacing and the staggering of the jet rows.

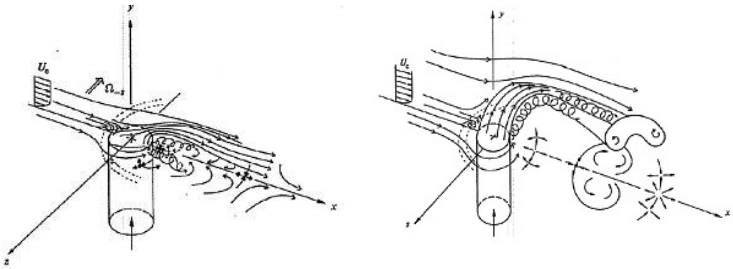

(a) $VR = 0.5$ *(b)* $VR = 2$

Figure 1.13: Coolant jet at low velocity ratio (left) and high velocity ratio (right) (Source [40])

Chapter 2

Numerical study of film cooling

Standard film-cooling geometries as well as modern angled effusion cooling schemes are based on coolant injection in the hot gas stream through circular holes. The injection of a jet in a transverse flow, or crossflow, gives rise to a highly complex turbulent flowfield dominated by many large scale, coherent flow structures which develop as a consequence of the interaction of the two streams [41].

Despite the interest and the efforts devoted to the analysis of the near wall development of the jet in crossflow (JCF) scheme, suitable CFD procedures capable to give satisfactory predictions have not been standardized yet. Even though DNS and LES have recently expanded the knowledge regarding the flow structures developing within the JCF [42, 43, 44], these techniques cannot still be considered, due to their high computational cost and complexity, as a valuable tool for design purposes, or in the simulation of complex cooling systems. Classical steady RANS approach exploiting eddy viscosity turbulence modelling, on the other side, typically shows common weaknesses in over-predicting the jet penetration and systematically underestimating the lateral spreading [45, 46].

In fact, for a jet in crossflow, the hypothesis of isotropic turbulence ceases to be applicable in the mixing zone. The normal to the wall fluctuation is damped by the wall itself while the stream and spanwise

directed fluctuations are influenced by the interaction with the jet. The macroscopic effect is an enlarged lateral diffusion compared to the other two main directions [47]. Despite their theoretical capability to partly model turbulence anisotropy, the Reynolds stress models do not usually significantly improve the overall accuracy of JCF mixing. Another explanation of the mentioned deficiencies is, in fact, the intrinsic unsteadiness of JCF which cannot be modeled through steady RANS [48].

Regardless of the cited numerical issues, the availability of accurate and reliable turbulence models for JCF computation with RANS approach is still a very challenging activity to help engineers in the design and optimization of real cooling systems. In recent years, several works have dealt with this objective. A pioneering approach in this field is the concept of directional eddy viscosity introduced by Bergeles et al. [49] to take into account the anisotropy of turbulent field in JCF. The idea is to use a tensorial definition of eddy viscosity where the terms responsible for jet lateral diffusion are augmented through a correction factor determined by higher order simulations (DNS data). This concept has been developed more recently by Azzi and Lakehal [50] with a detailed methodology to include the directional eddy viscosity in a two-layer $k-\epsilon$ model. This methodology was implemented and applied on literature test cases by Bacci and Facchini [47] and more recently to actual combustor liner cooling geometries by [51, 52, 53, 54]. A first attempt to extend the concept of directional eddy viscosity to other turbulence models was carried out by Cottin et al. [55] where the idea of Bergeles was implemented in a SST $k-\omega$ model with a benchmarking on a typical combustor liner effusion cooling geometry. Further contribution to this family of models comes from Li et al. [56] where a set of general purpose shape functions obtained by higher order computations are used in the tensorial definition of eddy viscosity.

The main drawback of this family of models is the necessity to establish the orientation of coordinate system axis with respect to holes geometry and therefore they can be strictly applied just to flat plate-like geometries. Moreover, such formulations are derived for steady state analysis; hence

they are valid for the mean fields only. The works of Walters [57] and Holloway et al. [48] propose a set of models, both for steady and unsteady RANS analysis, based on a local isotropic modification of eddy viscosity, with a correction factor evaluated through a dedicated transport equation.

The aim of this chapter is to review unconventional models proposed in literature and to benchmark their predicting capability against each other and standard turbulence models over a wide range of working conditions. In particular the models proposed by Azzi and Lakehal [50] and Holloway et al. [48] are considered.

Low and high blowing ratio conditions corresponding respectively to the mass addiction and penetration regime (accordingly to definition by L'Ecuyer and Soechting [21]) are investigated. The former regime is characterized by a coolant jet attached to the downstream wall, as a consequence reported in the following also as non-penetrating regime, and thus by a monotonically decreasing centreline effectiveness while in the latter the momentum of the jet is high enough to resist the bending effect of the crossflow and hence penetrates within the hot gas region, resulting in a lower film protection right downstream the hole. The effect of jet superposition is studied as well considering a 18 row staggered array of holes.

2.1 Numerical methods

In this section, details of numerical methods employed during the study are introduced.

2.1.1 ANSYS® CFX solver

One of the solver employed to perform 3D CFD RANS calculations is the Navier-Stokes solver ANSYS® CFX v.14. Compressibility effects have been taken into account and a High Resolution advection scheme has been used. Energy equation was solved in terms of total energy and viscous heating effects have been accounted for. Turbulence was modelled by means of the $k-\omega$ SST turbulence model, both in its original

formulation made available by the CFD solver and with an algebraic anisotropic correction suited to overcome typical RANS modelling failures for film cooling flows as described in details up ahead. Employed near wall treatment uses an automatic blending between Wall Function and Wall Integration approach on the basis of y^+ value. For all the cases presented, where $max(y^+) < 1$, the Low Reynolds formulation is always recovered.

During the analysis, in order to track the coolant distribution, a transport equation for an additional passive scalar, named *EffCool*, representing coolant concentration, holding the value 1 at the coolant inlet and 0 at the mainstream inlet, was solved. The value of its kinematic diffusivity was specified to guarantee a $Le = 1$ with the aim of fully respecting the mass-energy transfer analogy.

ANSYS® ICEM-CFD has been used to generate hybrid computational grids: details of particular employed meshes will be given accordingly to the studied geometry.

The solution convergence has been assessed by monitoring that RMS residuals fell below a prescribed value of 10^6 and verifying that the averaged value of η_{ad} on the plate reached a steady-state.

2.1.2 OpenFOAM® solver

The other solver (used basically to perform LES computation and turbulence modelling benchmarking) is based on OpenFOAM® [58] open source libraries for continuum mechanic. It is a 3D unstructured finite volume code based on a SIMPLE-like (semi-implicit method for pressure-linked equations) solving algorithm [59]. Steady-state assumption is made and under-relaxation technique is used to guarantee convergence since no fictitious time derivative is employed. In order to solve for both high and low Mach regimes, a pressure based approach including compressibility effects is exploited. The continuity equation is solved in terms of pressure correction to enhance robustness with an additional convective term to account for density variation.

Convective schemes use a second order upwind interpolation scheme

based on the NVA (Normalized Variable Approach) known in literature as self-filtered centred difference [60] blended with a deferred approach with a first order upwind scheme. More details on the adopted solving algorithm can be found in [61]. Such code solves for the Favre-averaged compressible Navier-Stokes equations; thus, assuming steady state, turbulence modelling is definitely a key factor for the success of the computation.

Convergence was reached in case the normalized residuals, defined as in Ref. [61], for each single equation drop below 10^6. Relative tolerance of 0.001 was instead employed in the resolution of single iteration matrices.

Concerning the unsteady computations, a flexible segregated solver, able to switch from URANS to LES just selecting a SGS model instead of a turbulence model, has been used. Pressure-velocity coupling is achieved implementing the PISO (Pressure Implicit Splitting Operator) loop as proposed by standard OpenFOAM® libraries. Dissipation of viscous stresses work into heat has been included into the energy equation to be consistent with the steady state solver. Time advancement was performed maintaining the Courant number less than 1 everywhere in the domain to guarantee stability also in case of purely linear schemes necessary for an accurate LES solution.

2.2 Turbulence modelling

In this section, the investigated unconventional turbulence models are presented in detail, providing the complete set of equations exploited to perform the computations.

2.2.1 Algebraic anisotropic correction

A very known failure of standard RANS numerical computations exploiting eddy viscosity assumption, already pointed out in previous studies [62, 63], is the low lateral spreading predicted for jets in crossflow. Both film and effusion cooling simulations tend in fact to concentrate the cooling effect on the mean line of the holes. This is due to the assumption of turbulence isotropy that fails in the near-wall region because of the

damping of normal to wall fluctuations. To avoid this discrepancy with experimental evidences, Bergeles et al. [49] proposed to algebraically correct the main Reynolds stress, enlarging the product of the stream and span directed fluctuation. The Reynolds Stress tensor is so calculated using a tensorial definition of turbulent viscosity:

$$-\rho\overline{u_i^{'}u_j^{'}} = \mu_{t,ij}\left(\frac{\partial U_i}{\partial x_j}+\frac{\partial U_j}{\partial x_i}-\frac{2}{3}\delta_{ij}\frac{\partial U_k}{\partial x_k}\right), \tag{2.1}$$

where

$$\mu_{t,ij} = \begin{pmatrix} \mu_t & \gamma\mu_t & \mu_t \\ \gamma\mu_t & \mu_t & \mu_t \\ \mu_t & \mu_t & \mu_t \end{pmatrix}, \tag{2.2}$$

and γ is an amplification factor ranging from 4.5 in the free-stream region to 60 in the near wall region [50].

The value for the anisotropic correction γ followed the correlation in Eq.2.3 bounded to the already mentioned upper and lower limits of 60 and 4.5 for $y^\star < 1.5$ and outside the buffer layer respectively.

$$\gamma = \frac{1000y^{\star 0.42}}{2.682y^{\star 2} - 5.463}\,, \tag{2.3}$$

This function was proposed by [64] to match DNS simulations of turbulent flat plate by [65], in which:

$$y^\star = 0.00442Re_y^2 + 0.294Re_y + 0.545\,. \tag{2.4}$$

The anisotropic factor γ profile in the near-wall region is reported in Figure 2.1.

The correction is applied to the domain of the evolving jet only thus isotropic formulation is recovered inside the coolant plenum and the hole.

2.2.1.1 Implementation in Two-Layer model

The above described anisotropic modification was inserted into the two layer $k-\varepsilon$ model [62] by Azzi and Lakehal [50], inside the OpenFOAM® solver. The two layer model consists in patching together a one equation

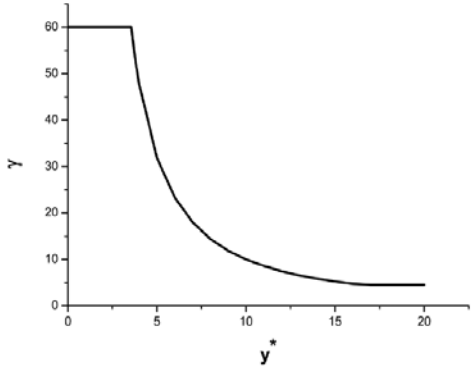

Figure 2.1: Anisotropic factor near wall profile

model in the near-wall layer and a two-equation high Reynolds model in the outer layer by means of an extended wall function for ε. This particular implementation of the two layer model, described and validated in [61], uses Norris and Reynolds closure formulas [66]. The anisotropic correction is introduced by means of additional source terms (conventionally taken on the right hand side of the conservation equations) modelling turbulent flux modification in the momentum, energy and turbulence transport equations as reported in Eq. 2.5.

$$\begin{aligned}
\mathcal{S}_u &= (\gamma - 1)\,\mu_t \frac{1}{2}\left(\frac{\partial u}{\partial y} + \frac{\partial v}{\partial x}\right) \\
\mathcal{S}_v &= (\gamma - 1)\,\mu_t \frac{1}{2}\left(\frac{\partial v}{\partial x} + \frac{\partial u}{\partial y}\right) \\
\mathcal{S}_h &= \frac{\partial\,(\gamma - 1)\,\dfrac{\mu_t}{Pr_t}}{\partial y} + (\gamma - 1)\,R_{xy}\left(\frac{\partial u}{\partial y} + \frac{\partial v}{\partial x}\right) \\
\mathcal{S}_k &= (\gamma - 1)\left[2.0\mu_t\left(\frac{\partial u}{\partial y} + \frac{\partial v}{\partial x}\right)^2 + \mu_t \alpha_k \frac{\partial^2 k}{\partial y^2}\right]
\end{aligned} \tag{2.5}$$

2.2.1.2 Implementation in $k-\omega$ SST model

The same correction was inserted into the $k-\omega$ SST framework by Cottin et al. [55]. It is implemented in OpenFOAM® code and ANSYS® CFX solver using the same source terms reported in Eq. 2.5.

Applications of the proposed model to film and effusion cooling cases can be found both for adiabatic [67, 68, 69] and conjugate heat transfer [52] computations.

2.2.2 *WHLU* model

The unsteady RANS turbulence model proposed by Holloway et al. [48] is here presented. It is based on a steady model previously proposed by the same author [57] which is recovered in case unsteady contribution is posed to zero. The contribution of turbulence on the mean flow, exploiting Bousinnesque hypothesis to model the Reynolds stress tensor, is decomposed into a mean and a fluctuating viscosity contribution as:

$$\mu_t = \bar{\mu}_t + \mu_t' \tag{2.6}$$

where

$$\bar{\mu}_t = X\bar{\beta}\rho f_\mu f_w C_\mu k \tau_{eff} \tag{2.7}$$

and

$$\mu_t' = (1-X)\,\beta'^2 \rho f_\mu f_w C_{\mu,std} \frac{k^2}{\varepsilon} \tag{2.8}$$

The model includes three transport equations for the turbulent kinetic energy (k), the scalar structural dissipation ($\widetilde{\varepsilon}$) and a strain rate parameter (σ^*) as:

$$\frac{D\rho k}{Dt} - \nabla\cdot\left(\left(\mu + \frac{\alpha_T}{Pr_k}\right)\nabla k\right) = P_k - \rho f_k \widetilde{\varepsilon} - g_k \frac{2\mu k}{d^2} \tag{2.9}$$

$$\frac{D\rho\widetilde{\varepsilon}}{Dt} - \nabla\cdot\left(\left(\mu + \frac{\alpha_T}{Pr_\varepsilon}\right)\nabla\widetilde{\varepsilon}\right) = C_{\varepsilon 1} P_k \frac{\widetilde{\varepsilon}}{k} - \rho C_{\varepsilon 2} f_{\varepsilon 2} f_k \frac{\widetilde{\varepsilon}^2}{k} \tag{2.10}$$

$$\frac{D\rho\sigma^*}{Dt} - \nabla\cdot\left(\left(\mu + \frac{\alpha_T}{Pr_\sigma}\right)\nabla\sigma^*\right) = \rho C_\sigma \left(\bar{S} - \frac{\widetilde{\varepsilon}}{k}\sigma^*\right) \tag{2.11}$$

The latter variable is included to better resolve the short-time response of the stress tensor to rapid strain rates. It represents, in fact, the local effective total strain which is a more relevant parameter to evaluate the turbulent viscosity in case of rapid or increasing strain rates than the mean-to-turbulent time scale ratio. This transported quantity modifies the calculation of the mean turbulent viscosity, influencing the terms τ_{eff} and C_μ in Equations 2.7 and 2.8, only in case that it is lower than the ratio between $\bar{S}$ and the turbulent time scale, i.e. ε/k , as follows:

$$\sigma = \min\left(\sigma^*, \frac{\bar{S}k}{\widetilde{\varepsilon}}\right)$$

$$C_\mu = \frac{1}{A_0 A_s \sigma} \tag{2.12}$$

$$\tau_{eff} = \min\left(\frac{k}{\widetilde{\varepsilon}}, \frac{\sigma}{\bar{S}}\right)$$

The other parameters in Equations 2.7 and 2.8 represent: X a measure of the alignment between instantaneous and time-averaged resolved strain rate, β a limiter to damp effective viscosity in non-equilibrium shear layers, f_μ and f_w the viscous and inviscid damping functions characterized by γ which is the ratio of wall distance (y) to large-eddy turbulence length scale $(k^{3/2}/C_L\widetilde{\varepsilon})$. The expressions for both the time-averaged and instantaneous values are:

$$X = \max\left(0, \frac{2\bar{S}_{ij}S_{ij}}{\bar{S}S}\right) \tag{2.13}$$

$$\bar{\beta} = \min\left(1, \frac{3.33\widetilde{\varepsilon}}{\bar{\Omega}k}\right) \text{ if } \frac{\bar{\Omega}y}{\left|\bar{U}\right|} > 1.1,\ \bar{\beta} = 1 \text{ otherwise} \tag{2.14}$$

$$\beta' = \min\left(\frac{3.33\widetilde{\varepsilon}}{Sk}, 1.0\right) \tag{2.15}$$

$$f_\mu = 1 - \exp\left(-\frac{y}{A_\mu L_k}\right) \tag{2.16}$$

$$f_w = \gamma\left(2 - \gamma\right) \tag{2.17}$$

Table 2.1: WHLU model constants

$A_0 = 4.04$	$A_k = 3.5$	$A_s = 2.12$	$A_s = 13.5$
$C_L = 2.495$	$C_{\varepsilon 1} = 1.44$	$C_{\varepsilon 2} = 1.9$	$C_{\mu,std} = 0.09$
$C_\sigma = 4.2$	$Pr_k = 1.0$	$Pr_\varepsilon = 1.17$	$Pr_\sigma = 1.0$

Table 2.2: Summary of investigated turbulence models

TL	Two-Layer model	Isotropic turbulence modelling
TLA	Anisotropic TL	Bergeles's anisotropic correction in TL
SST	Shear-Stress Transport model	Isotropic turbulence modelling
SSTA	Anisotropic SST	Bergeles's anisotropic correction in SST
WHLU	Unsteady model by [48]	Isotropic turbulence modelling based on local effective strain
WHL	Steady state version of WHLU	No fluctuating turbulent viscosity

$$\gamma = \min\left(\frac{C_L y\widetilde{\varepsilon}}{k^{\frac{3}{2}}}\right) \tag{2.18}$$

In order to close the resolved transport equations, additional relations, such as Equation 2.19, are needed as well as the constants reported in Table 2.1.

$$f_k = 1 - \exp\left(-\frac{y}{A_k L_k}\right)$$

$$g_k = \exp\left(-0.2445\frac{y}{L_k}\right) \tag{2.19}$$

$$f_{\varepsilon 2} = 1 - \frac{2}{9}\exp\left(-\frac{Re_T^2}{36}\right)$$

A brief summary of the investigated models, their main features and nomenclature adopted in the discussion of the results is presented in Table 2.2.

2.3 Single row plate

2.3.1 Test case description

The first faced test case is the one studied by Sinha et al. [27]: they performed measurements of film-cooling effectiveness using a row of inclined holes that injected cryogenically cooled air across a flat, adiabatic test plate. They studied the effect of BR and DR on η_{aw}. The geometry consists of a flat plate with a single row ($S_y = 38.2\ mm$) of large ($D = 12.7\ mm$) cylindrical holes at 35° of inclination angle, fed with coolant from a plenum at constant pressure (see Figure 2.2). The text matrix covers a wide range of coolant conditions, varying independently DR and BR: they observed a strong influence of momentum flux ratio (I) on jet behaviour coming out from the hole, leading to jet attachment to the surface, detachment and reattachment or fully detachment.

For the purposes of this analysis, only flow conditions representative of a non-penetrating regime are investigated ($BR = 0.5$, $DR = 2$): in this way, this test case becomes representative of a mass addiction regime, and so a jet completely attached to the surface (following definition by L'Ecuyer and Soechting [21]). A summary of the applied boundary conditions is reported in Table 2.3.

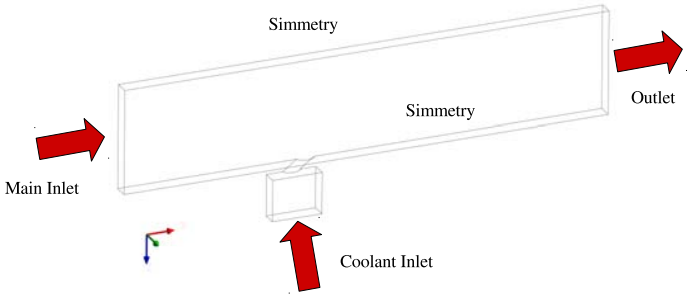

Figure 2.2: Sketch of the adopted computational domain (single row test case)

Table 2.3: Flow conditions (single row test case)

Crossflow temperature [K]	300
Coolant temperature [K]	153
Pressure [Pa]	10^5
BR [-]	0.5
DR [-]	2
Turbulence level (Tu) [%]	≤ 0.2
Crossflow velocity [$m\ s^{-1}$]	20

2.3.2 Numerical details

The symmetry of geometry and boundary conditions was exploited to simplify the computational domain to a half of the hole only in case of steady-state turbulence modelling (Figure 2.2). This technique, which allows higher convergence rates under steady-state assumption, was avoided for the unsteady model in order not to damp the shedding of the wake downstream the hole. Periodic boundary conditions on the sides of the domain were implemented instead. The domain extends more than $18 \cdot D$ upstream and $30 \cdot D$ downstream the hole, the upper confinement is modelled as a symmetry plane to avoid mesh clustering and is posed $10 \cdot D$ above the plate. So, only one hole has been studied, neglecting interactions between two adjacent holes since the high S_y value.

Multi-block structured meshing strategy was employed. Since the implementation of low-Reynolds near-wall treatment, a consistent mesh refinement with $y^+ < 1$ for the first cell layer and with at least 20 cells in the boundary layer was realized. The final mesh size was $177 \cdot 10^3$ cells for the half hole model.

Since this case is the less computationally expensive among the one proposed in this work, it was decided to complete the analysis with a large eddy simulation refining the mesh in the stream and span direction and using the same topology totally achieving $1.4 \cdot 10^6$ cells: eight times higher than the number of cells with respect to the steady state and four times with respect to the WHLU setup. This corresponds approximately

to 90 elements in the span direction, 110 elements downstream the hole, and 40 in the normal to the wall direction for the downstream flat-plate. The interior part of the perforation is discretized using around 40 cells in the radial and more than 100 in the tangential direction.

Even though the mesh is getting too coarse moving away from the hole injection to resolve correctly, in the turbulent flow field, inside the wake of the jet issuing from the hole, the resolved turbulent kinetic energy is more than 90% of the total kinetic energy. The aim of this simulation was not to evaluate the enhanced capability of LES in modelling the thermal boundary layer development (for this purpose in fact near-wall resolution is certainly not sufficient to resolve correctly the energy spectrum since x^+ and z^+ grows above acceptable limits already at $X/D > 3$), but to use this solution as a comparison for the flow structures developing around the jet in cross-flow.

RANS type boundary conditions were imposed at the inlets, thus main flow turbulence is certainly underestimated. For the outflow, a wave transmissive condition, which imposes an advective condition $D\Phi/Dt$ for the extrapolated variables and a linear relaxation technique for static pressure, is employed.

The unsteady calculations were run for more than 80 ms (160 ms for the LES due to a much larger transient evolution of the solution) and the averages were extended for nearly 40 ms. The time steps, chosen to guarantee a maximum Courant number close to 1, were respectively $2 \cdot 10^{-6}$ s and $1 \cdot 10^{-6}$ for the WHLU model and the LES simulation resulting in a total of around 40 (serial mode) and 500 (in parallel mode) hours on a 4 cores Intel-i7® 930 at 2.80 GHz.

In order to complete the analysis, the two-layer and SST models were run in the unsteady solver while the WHL was investigated in the steady mode. The isotropic RANS models did not show relevant unsteadiness due to high turbulent viscosity that damp any possible fluctuation; thus the results for their unsteady run basically coincide with the steady one and were not included.

2.3.3 Results

As expected, the turbulence modelling has a strong impact on the adiabatic effectiveness distribution both from a qualitative and a quantitative point of view, as can be appreciated in Figure 2.3. The first thing

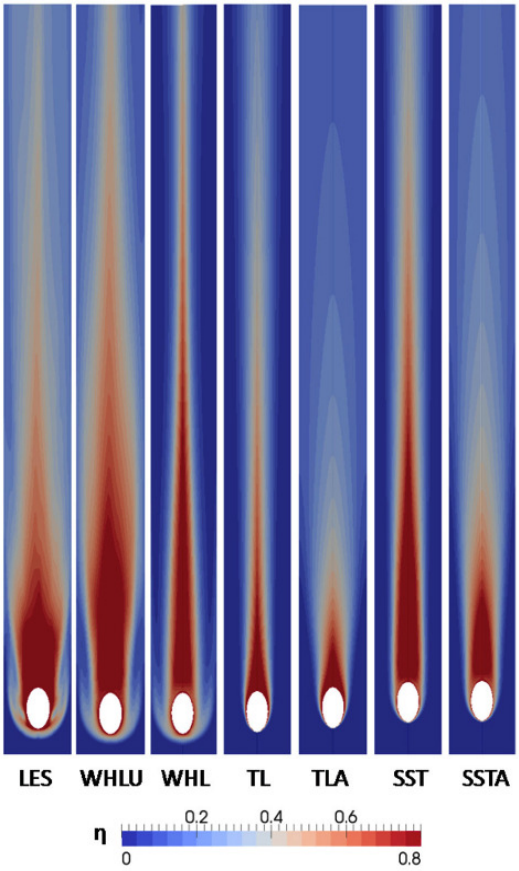

Figure 2.3: Distribution of adiabatic effectiveness on the wall: all maps but LES and WHLU are mirrored against hole symmetry line (single row test case)

to note is related to the effects of the horse-shoe-like structure developing at the upstream lip of the hole. The WHL and the LES simulations in fact report a trace of relatively high effectiveness upstream the hole itself due to a vortical structure recirculating the coolant as reported in Figure 2.4a. This little vortex is part of the more complex horse-shoe like vortex structure reported in Figure 2.4b where the Q criterion is used to deduce coherent structures. The capacity of the WHL model to predict this structures was already reported by the authors who proposed the model for a jet injection at 90° [48] showing a good qualitatively agreement with available experiments [70].

Secondly, the three isotropic steady models (TL, SST and WHL steady) show a much less uniform effectiveness at the end of the plate due to a reduced jet spreading in the span direction as well documented in literature

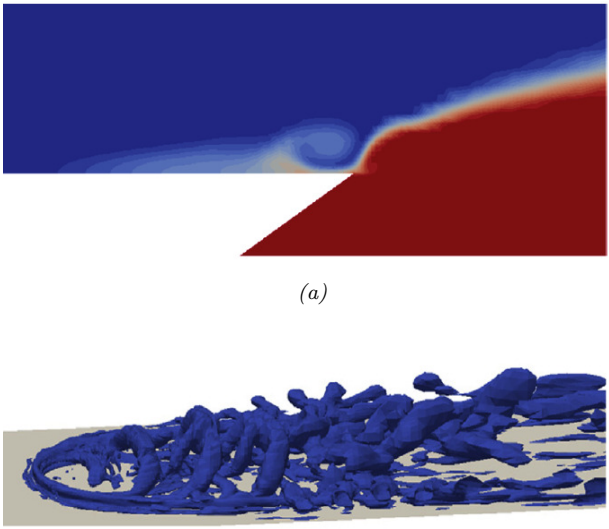

(a)

(b)

Figure 2.4: Near hole flow and thermal field details (single row test case)

[51]. Vice versa, both the unsteady computations, and even more the algebraically corrected models, are able to overcome this deficiency. This can also be seen in Figure 2.5, where the span-wise profiles of the adiabatic effectiveness are reported at three stations ($X/D = 1, 10, 15$) downstream the hole.

Except for $X/D = 1$ where the effect of the horse-shoe vortex dominates the lateral effectiveness values as LES, WHLU and WHL report an increase in the span profile, the three corrected models (TLA, SSTA, WHLU) and the LES computations show a lateral slope of the effectiveness profile in fairly good agreement with experiments and realistic levels of temperature at the lateral symmetry plane. Moreover, the steady models

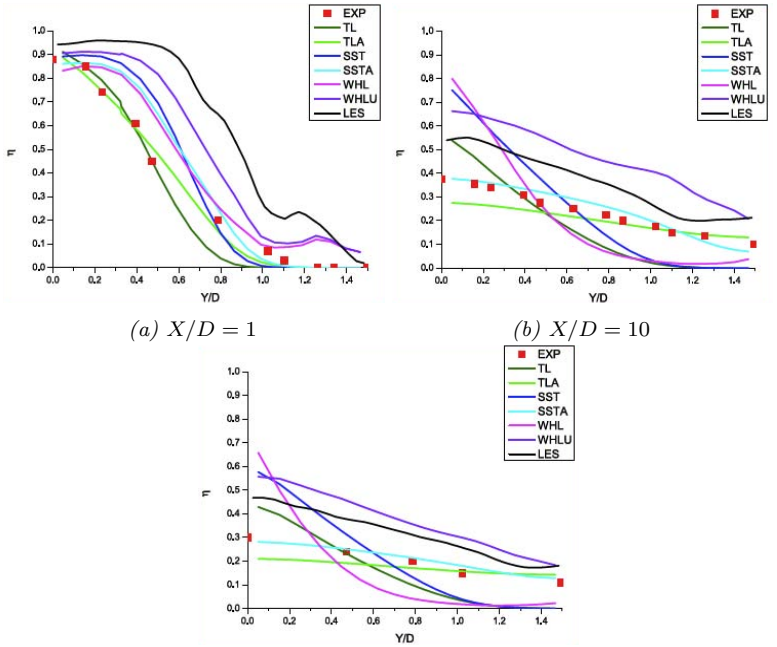

(a) $X/D = 1$

(b) $X/D = 10$

(c) $X/D = 15$

Figure 2.5: Span-wise profiles of adiabatic effectiveness at various X/D sections (single row test case)

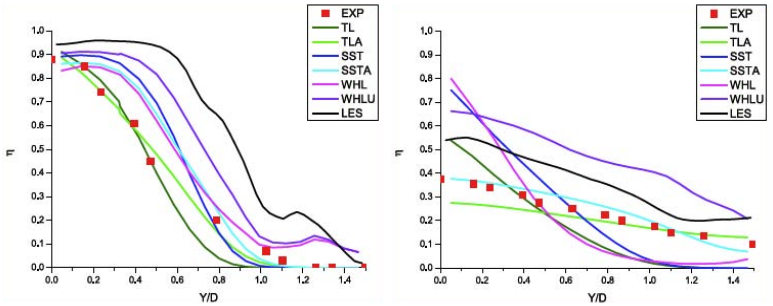

Figure 2.6: Centreline (a) and span-wise averaged (b) adiabatic effectiveness profiles (single row test case)

exploiting Bergeles et al. [49] correction are also capable of predicting the centreline experimental values fairly well while the unsteady computation (WHLU and LES) results in a too high centreline coverage like the conventional turbulence models employed.

In order to appreciate the stream-wise evolution of the film, the profiles of both centreline and span-wise averaged adiabatic effectiveness are reported in Fig. 6. In terms of centreline values, all models but the Two Layer models show a starting value for adiabatic effectiveness below 1, due to the detachment of the jet right downstream the injection, and a retarded peak between $X/D = 2$ (LES) and $X/D = 5$ (SST) caused by the progressive coverage. SST and LES show the same decreasing profile of the experiments up to $X/D \approxeq 5$ where LES stops the reduction while SSTA continues to follow experimental curve up to $X/D > 20$. The TLA model predicts lower values approaching the expected values only in the limit of very high X/D. The WHLU vice versa strongly over-predicts the experimental profiles as much as the SST and its steady counter-part.

Concerning the span-wise averaged profiles, the unsteady simulations show much higher values than the other models due to the larger imprint of the jet on the wall as already noticed in Figure 2.3.

2.3.4 Remarks

This benchmark showed that compared with standard multi-purpose turbulence models, unconventional ones improve the level of accuracy of the computations at low blowing rate. Moreover, it is not possible to indicate a single model able to predict the complex thermal field correctly. WHLU, which is the only unsteady model investigated, seems to be more physically based, but results tend to be highly costly and quantitative predictions are poor at low blowing rate. SSTA well behaves at the studied conditions, while the TLA even though in more quantitative agreement for the averaged values with the experiments is not able to capture some qualitative phenomena.

It is important to highlight that, from an industrial point of view, unsteady models are not affordable in terms of computational time: as said above LES computation on a single hole costed about 500 hours of calculation, and considering a complete nozzle cooling scheme of 500 perforations, it easy to say that steady models are preferable. Furthermore, OpenFOAM® is not still acknowledged as a reliable tool by the whole industrial community, hence for the next test case, the employed solver will be ANSYS® CFX. For this reason, only the SST model (available in the code) and its anistropic modification (implemented inside the code) will be studied.

2.4 Multi row plate

This test case introduces the superposition effect since more than one row of holes is considered. Furthermore it investigate higher blowing ratio values.

2.4.1 Test case description

This numerical analysis is based on equivalent geometries and flow conditions as those employed in a parallel experimental investigation performing Pressure Sensitive Paint measurements to evaluate purely

adiabatic effectiveness [71]: in Section 2.4.2 further details about this measurement technique will be provided. Among the different arrays considered in the experimental campaign, only two plates, characterized by a different hole perforation angle α, are considered in this work; most relevant geometric features are summarized in Table 2.4.

The numerical set up aims at reproducing the main characteristics of the experimental rig (depicted in Fig. 2.7) such as the feeding duct shape of the hot and coolant gas and a turbulence generator grid able to provide two different levels of turbulence intensity, low ($Tu = 1.6\%$) and high ($Tu = 17\%$). Furthermore, each plate has been tested with several blowing ratios (BR) conditions (1.0, 2.0, 3.0). In order to generate oxygen partial pressure gradient necessary for the PSP based technique, the coolant is fed with nitrogen while the mainstream consisted of air. The test is conducted at almost isothermal condition thus the effective density ratio is virtually 1.

Table 2.4: Test plate geometry (multi row test case)

Name	D [mm]	*Rows*	L/D	α	s_x/D	s_z/D
G2	1.50	18	6.25	30	9.15	7.37
G7	1.50	18	3.13	90	9.15	7.37

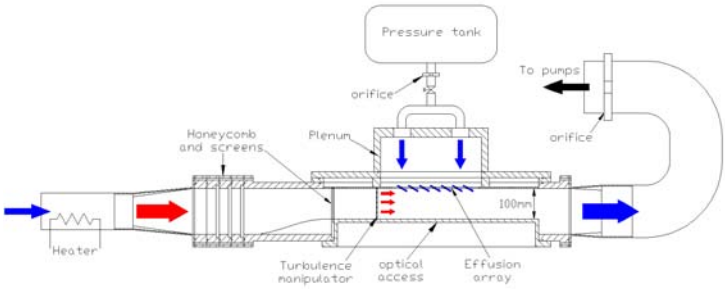

Figure 2.7: Sketch of the experimental test rig (multi row test case)

Table 2.5: Test matrix of performed simulations (multi row test case)

Name	α [*deg*]	DR [−]	Tu [%]	BR [−]		
G2	30	1	1.6	1	2	3
			17.7	1	2	3
		1.7	17.7	1	2	3
G7	90	1	17.7	1	2	3
		1.7	17.7	1	2	3

The numerical analysis aims at widening the investigated range of conditions exploring hot stream conditions to generate a density ratio of 1.7 which is representative of typical isothermal experiments conducted with CO_2.

The full test matrix of the simulations performed in the present work is summarised in Table 2.5.

The experimental data set was also exploited to perform a computational model sensitivity which was conducted on G2 at $BR = 2$ chosen as the reference case.

2.4.2 Adiabatic effectiveness measurements

Pressure sensitive paint (PSP) is an organic substance, composed by oxygen sensitive molecules embedded in the paint solution using a polymer binder permeable to oxygen. Through the exploitation of the luminescence behaviour of these molecules, PSP can be used to measure the oxygen concentration of the atmosphere surrounding the paints, which in turn can be linked to the partial pressure of air. This property makes the paint suitable for gas concentration technique based on the heat and mass transfer analogy [72], e.g. for adiabatic effectiveness measurements.

Despite the fact that the applicability of heat and mass transfer analogy has limitations, especially in case of flowfields where viscous effects are dominating, it represents a good approximation for test cases as encountered in the present work [73]. Assuming valid the analogy, if a tracer gas without free oxygen (e.g. N_2 or CO_2) is used as coolant in

the vane cooling system it is straightforward to replace the temperature definition of film cooling effectiveness by mass fractions of oxygen [72], and hence in terms of O_2 partial pressure measured with PSP [74]:

$$\eta_{aw} = \frac{T_{main} - T_{aw}}{T_{main} - T_{cool}} \equiv \frac{C_{main} - C_w}{C_{main}} = \\ = 1 - \frac{1}{\left(1 + \left(\frac{P_{O_2;air}/P_{O_2;ref}}{P_{O_2;fg}/P_{O_2;ref}} - 1\right)\frac{M_{fg}}{M_{air}}\right)} \tag{2.20}$$

where C_{main} and C_w are oxygen concentration respectively in the main free stream and in proximity of the wall.

The uncertainty estimate on adiabatic effectiveness measurements was based on the method proposed by Kline and McClintock [75] and on a confidence level of 95%. It was estimated to be 10% for $\eta_{ad} = 0.2$ and 3% for $\eta_{ad} > 0.8$, taking into account the uncertainties in calibration and image capture. The adiabatic effectiveness tests were repeated several times in order to confirm the repeatability of the results.

2.4.3 Numerical details

3D CFD RANS calculations have been performed exploiting Navier-Stokes solver ANSYS® CFX v.14. For further information about numerical setup, see Section 2.1.1.

The mainstream boundary conditions have been assigned in terms of total pressure, total temperature and turbulence quantities at the main inlet, mass flow rate and total temperature are specified at the coolant inlet and mass flow rate was fixed at the outlet (Figure 2.8).

Injections of both air and nitrogen were modelled with identical gas properties assuming ideal gas behaviour. From a dimensional analysis the thermal field in totally driven by convection, so the effect of buoyancy was neglected both for $DR = 1$ and $DR = 1.7$.

In order to reduce the computational cost, it has been decided to take advantage of the symmetry condition offered by the geometry (see Figure 2.8). In this way, only half hole has been modelled for each row.

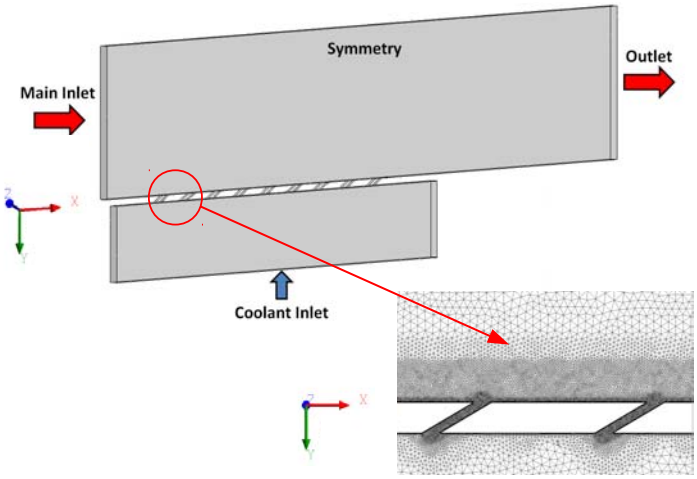

Figure 2.8: Sketch of the numerical domain and particular of the mesh (multi row test case)

2.4.4 Mesh sensitivity analysis

Generally speaking, in turbomachinery applications structured multi-block hexahedral meshes are most often used for flow-path simulations: a structured grid requires less memory, provides superior accuracy and allows a better boundary-layer resolution than an unstructured grid. On the other hand, unstructured meshes are used for more complex and odd geometries where a structured mesh is difficult to create, such as: blade tip regions, areas involving leakage flows and secondary air systems, film cooling holes etc. Moreover, it is well known that mesh refinement plays a central role in film cooling simulations. So, giving the complexity of the studied geometry, it has been chosen to employ a hybrid unstructured mesh (tetra with prism at wall surfaces) and a comprehensive mesh sensitivity analysis has been performed on the reference case in order to find a cost-effective grid resolution able to correctly capture local

concentration gradients at an affordable computational cost.

Four grids have been tested in this analysis: the first mesh (Mesh A) counts 2.5 million of elements, the second one (Mesh B) has been generated reducing of 40% the global scale factor and hence increasing the number of elements up to 5.0 millions of elements. Last two grids (Mesh C and D) included further refinements in the mixing region and within the holes, resulting in 7.2 and 22.4 millions of elements respectively.

The results have been reported in Fig. 2.9, which highlights the effect of mesh refinement on span-wise averaged adiabatic effectiveness against experimental results from Andreini et al. [71]. All simulations result in a strong underestimation in the first rows of holes, most likely caused, as demonstrated in the following section, by the assumption of turbulence isotropy on which standard $k-\omega$ SST model is based. Most important in this context is however to highlight the effects of the mesh refinement. Successive mesh refinements lower the span-wise averaged effectiveness at the end of the plate, which is opposite to the experimental evidence, but

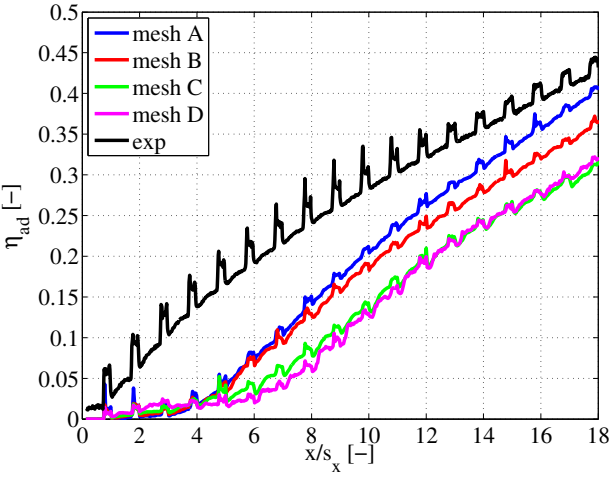

Figure 2.9: Multi row test case: sensitivity to mesh refinement (G2, BR=2)

improve the capability to reproduce the trend of growth matching the slope of experimental curve. Last refinement from Mesh C to D, resulting in a three times higher number of elements, does not show a significant variation on the obtained wall concentrations, hence Mesh C has been used for the following investigations.

2.4.5 Turbulence model sensitivity analysis

Following the considerations coming from single row plate analysis (Section 2.3) about turbulence modelling, the algebraic anisotropic correction was hence implemented and tested against standard isotropic $k-\omega$ SST turbulence model.

The main effect of the above proposed anisotropic correction is a larger diffusivity in the near wall region which results in a lower coherence of the cooling jets whose shape, especially in the first rows of holes, is largely influenced by the turbulence modelling. Figure 2.10 reports a contour plot of coolant concentration on a plane normal to the stream-wise direction positioned $1D$ downstream the 9^{th} hole. It is possible to note how the

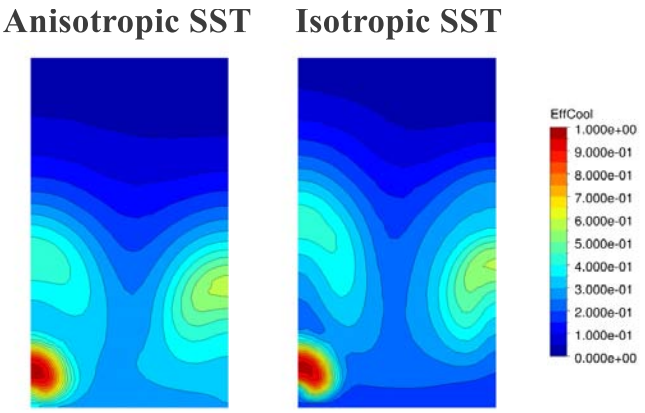

Figure 2.10: Multi row test case: contour plot of coolant concentration at $X/D = 1$ for 9^{th} hole (G2, BR=2)

anisotropic model predictions result in a lower jet penetration and in a less pronounced kidney-vortex which is responsible for the ingestion of hot gas below the jet itself. In such a way the entire region within the two symmetry planes shows a higher film protection due to a more complete merging of consecutive jets.

This effect is responsible for increased levels of cooling effectiveness especially where superposition does not play a fundamental role thus resulting in a rapid increase of averaged value able to reproduce the experimental growth rate already from the first rows of holes. Figure 2.11a shows that, despite a slight overestimation, the agreement with the experimental curve is very good for the anisotropic SST model both in terms of concentration value and superposition effect. Compared to the isotropic model, the anisotropic model permits to reduce the discrepancy with experimental data on average by an order of magnitude as better highlighted in Figure 2.11b, where the relative error between spanwise averaged adiabatic effectiveness values obtained by numerical predictions and experiments is reported as a function of streamwise position. As already hinted the anisotropic correction is highly beneficial for the first rows of holes but is also capable of reducing the asymptotic error below

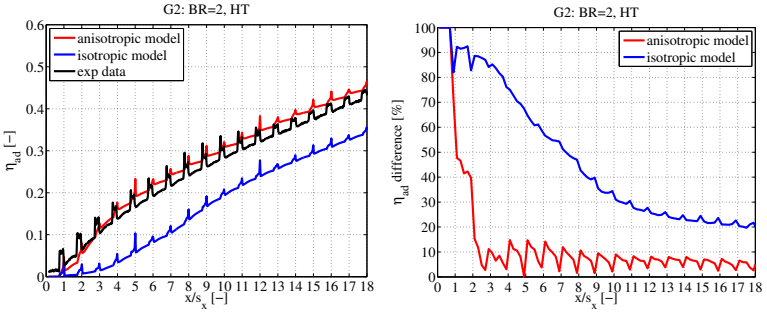

(a) Span-wise averaged η_{ad} *(b) Span-wise averaged η_{ad} absolute error*

Figure 2.11: Multi row test case: turbulence model effects on adiabatic effectiveness for G2 geometry

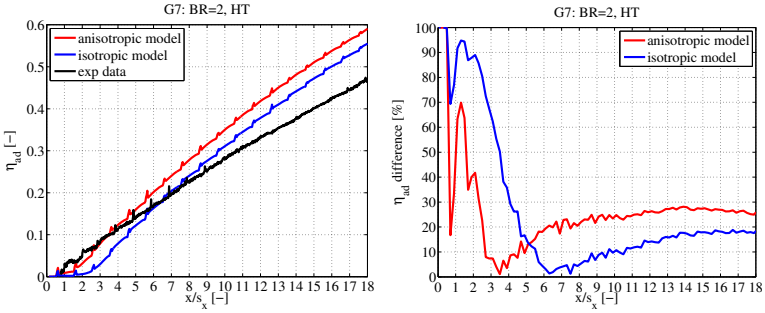

(a) Span-wise averaged η_{ad}

(b) Span-wise averaged η_{ad} absolute error

Figure 2.12: Multi row test case: turbulence model effects on adiabatic effectiveness for G7 geometry

8% while standard isotropic formulation is assessed around 20%.

The same analysis was conducted on G7, as pointed out by Figures 2.12a and 2.12b. The two models predict equivalent levels of effectiveness with an almost constant shift of about 0.03 which makes G7 more insensitive to turbulence modelling. The anisotropic model shows the same increase of accuracy for the first 5-6 rows of holes but, since the trend of growth is over-predicted by both models, the isotropic predictions result to be closer to experimental data approaching the end of the plate. Computation of the relative error does not offer a clear estimate of which model is globally preferable thus to make the analysis more homogeneous the following simulations will be performed with the corrected turbulence model.

2.4.6 Blowing ratio effects

In Figure 2.13, comparisons between experimental and numerical data for G2 at three different BR values are reported. As can be seen, numerical model well predicts span-wise averaged adiabatic effectiveness for both trend and values, especially at higher BR values. CFD leads to a general overestimation of the experimental data, revealing higher peaks

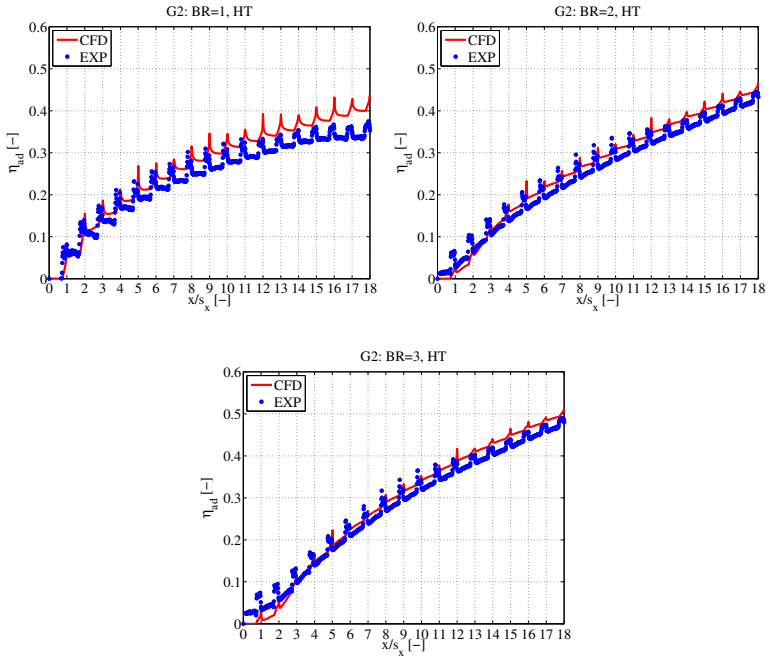

Figure 2.13: Multi row test case: BR effects on adiabatic effectiveness (G2 geometry)

just downstream coolant injection as highlighted by BR=1 results.

Increasing the BR, the jets detach from the wall and the cooling effectiveness due to film protection strongly reduces, as can be seen for first rows of holes. This phenomenon takes place for $1 < BR < 2$ as first rows effectiveness is pretty much the same for BR=2 and 3. However, due to the higher coolant mass flow injected, the superposition effect is larger and the plate effectiveness is enhanced downstream. Although an asymptotic condition could not be verified at any of the tested blowing ratios even for $x/s_x = 18$, the trend of growth results to be proportional to BR.

This is true even more for 90° holes, whose spanwise averaged η_{ad} is

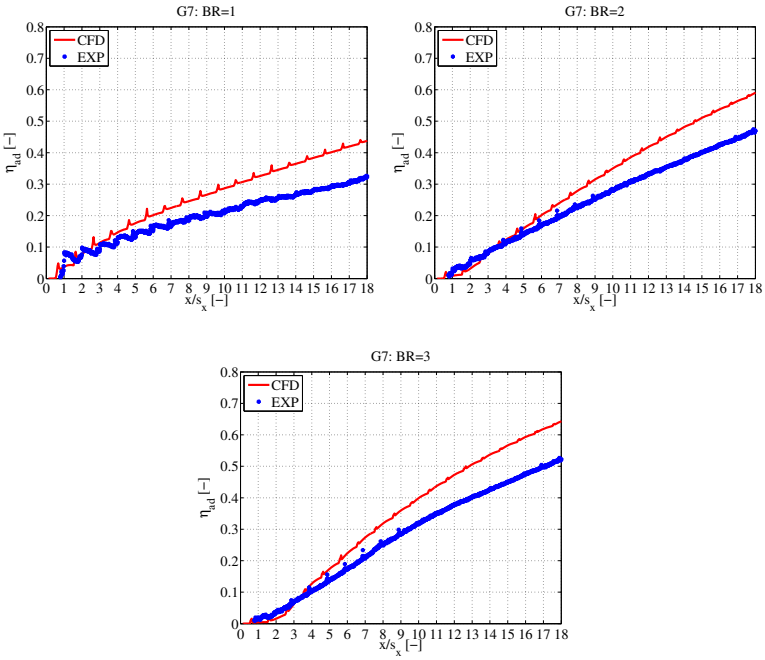

Figure 2.14: Multi row test case: BR effects on adiabatic effectiveness (G7 geometry)

plotted in Figure 2.14, where the trends among the three investigated blowing ratios are similar also for BR=1 because jet is always in penetration regime. For this flow configuration where near wall effects are less dominant, CFD predictions with the anisotropic turbulence model show a systematic overestimation of the locally averaged effectiveness and the trend of streamwise growth resulting in a shift of η_{ad} downstream the last row of approximately 0.12 independently on the BR; this corresponds to roughly 30% for BR =1 and to 20% a BR = 3. To the author knowledge, this is the first attempt to use such anisotropic turbulence model with orthogonal perforations, further work in the tuning of such correction is believed to provide better estimate also for normal injection flow.

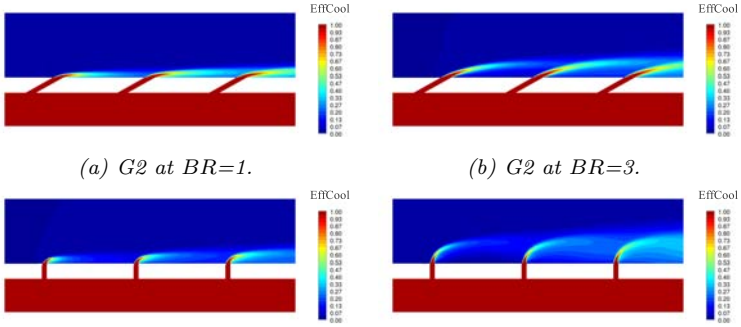

(a) G2 at BR=1. (b) G2 at BR=3.

(c) G7 at BR=1. (d) G7 at BR=3.

Figure 2.15: Multi row test case: contour plot of coolant concentration on symmetry plane for both geometries (for 1^{st}, 3^{rd} and 5^{th} rows)

In order to better understand the flow characteristics in the investigated conditions, concentration contour plot on the symmetry plane are presented in Figure 2.15, focusing on the first 3 odd rows of holes. Flow conditions are largely sensitive to both BR and injection angle. As already hinted mass addiction regime is reported only for G2 at $BR = 1$ where jets are actually confined in a thin layer along the wall. for the 90° injection instead the normal to the wall momentum is already high enough to guarantee jet penetration at least from the 3^{rd} row.

At the higher blowing ratio the penetration regime is achieved also by G2. Jet shape is however quite different between G2 and G7, as G7 shows a thicker wall layer affected by coolant injection and a higher streamwise diffusion of the jet, furthermore jet bending towards the wall is promoted as evidenced by the 5^{th} hole.

2.4.7 Inlet turbulence effects

Figure 2.16 shows spanwise averaged adiabatic effectiveness for two levels of inlet turbulence intensity (HT and LT) with varying BR for G2.

Comparing high turbulence and low turbulence intensity cases, it is possible to highlight that as turbulence intensity increases also adiabatic

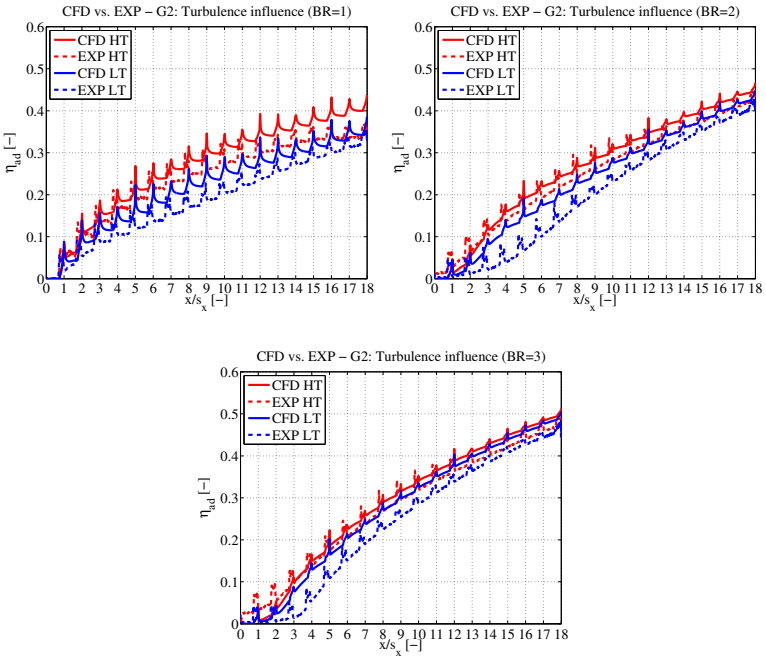

Figure 2.16: Multi row test case: inlet turbulence effects on adiabatic effectiveness (G2 geometry)

effectiveness increases. The enhanced level of mixing between the two flows results beneficial both in mass addiction and penetration regime because of the promoted lateral diffusion of the jet on the wall in the former case and the lower jet penetration in the latter.

Likening experiments and numerical data, it is clear that CFD is less influenced by inlet turbulence intensity especially for the high blowing ratios. Both at BR=2 and 3 conditions in fact, numerical results do not show the initial low levels of adiabatic effectiveness associated with LT and the two curves results to be almost coincident. This is due to the fact that numerical diffusivity is mostly driven by turbulence generated within the cooling duct which is insensitive to the inlet free turbulence intensity.

For BR=1 the two turbulence levels show the same effectiveness increase on the first rows but a different growth rate due to superposition resulting in a shift which remains quite constant along the plate, vice-versa the experiments show similar values at the end of the plate.

2.4.8 Density ratio effects

As regards the influence of Density Ratio on adiabatic effectiveness, in Figures 2.17 and 2.19 comparisons between simulations conducted with DR=1 and 1.7 values are presented, since no experimental data are available for this DR value. Comparing Figures 2.17a and 2.17b, it is possible to see that at low BR, DR has a high influence on η_{ad}, while at higher BR no difference is evidenced. In order to understand possible explanations of this effect, Figure 2.18 presents *EffCool* contour plot 3D downstream the 9^{th} hole. At equivalent BR the configuration with enhanced DR have a lower velocity ratio which affect the interaction between the coolant and the main stream resulting in more deflected jets in case of DR >1 as the imprints on the cutting plane are closer to the wall. However, concerning wall adiabatic effectiveness, this does not have an effect when the jet is detached from the wall, as at BR=2, while in the

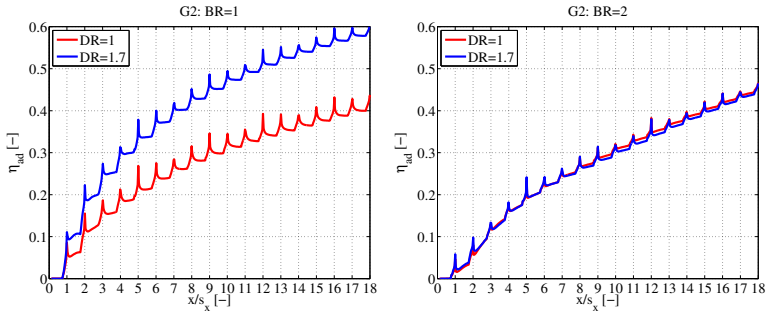

(a) BR=1. *(b) BR=2.*

Figure 2.17: Multi row test case: DR effects on adiabatic effectiveness (G2 geometry)

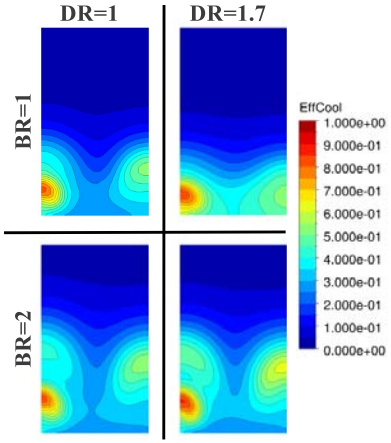

Figure 2.18: Multi row test case: coolant concentration contour plot on planes placed 3D downstream the 9^{th} row (G2 geometry)

mass addiction regime it results in more flattened jets close to the wall. The effect at BR=1 is highlighted at higher distance from the injection, as the jet issued from the previous hole (on the right) has an imprint adjacent to the metal surface for DR=1.7, while the jet remains detached from the surface for DR=1. For greater BR value (BR=2), adiabatic effectiveness is immune to DR influence (Figure 2.17b): in this case DR effects are compensated by VR decrease effect, resulting in a jet placed nearly at the same position of the correspondent case at DR=1 (2.18).

The very same considerations remain still valid for G7 configuration: even in this case, DR most affects coolant effectiveness at low BR (Figure 2.19a) than at high BR (Figure 2.19b), even if it has less influence than for G2 configuration. Coolant concentration contour plots on a plane orthogonal to the streamwise direction placed 1D downstream the 9^{th} hole are depicted in Figure 2.20 to explain this behaviour. The effects of DR on the coolant concentration field are equivalent to those highlighted for G2, but in this case the higher lateral spreading of the jet occurs at higher wall distance, thus the effect on wall effectiveness is already lowered at $BR = 1$ and substantially disappears at $BR = 2$.

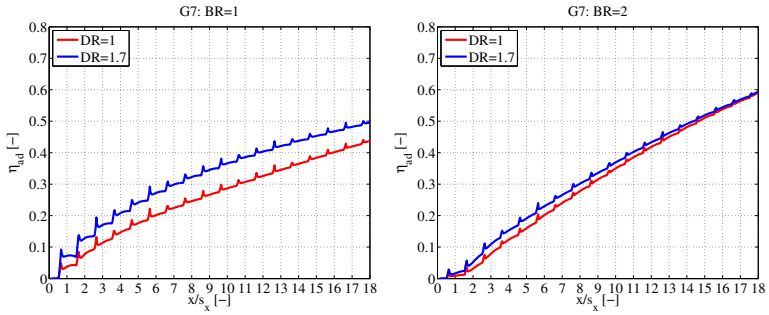

(a) BR=1. *(b) BR=2.*

Figure 2.19: Multi row test case: DR effects on adiabatic effectiveness (G7 geometry)

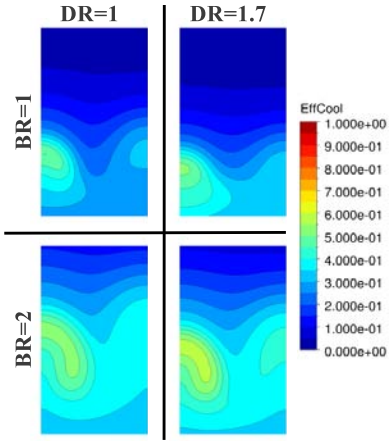

Figure 2.20: Multi row test case: coolant concentration contour plot on planes placed 3D downstream the 9^{th} row (G7 geometry)

2.5 Final remarks

A systematic analysis of the performance of unconventional RANS turbulence models specifically developed for film and effusion cooling applications has been performed exploiting an open-source CFD code and

a commercial one. Investigated conditions embrace both the penetration and non-penetration regime with BR ranging between 0.5 to 3.0 and include single hole and multi-row flat plate film cooling. This benchmark showed that compared with standard multi-purpose turbulence models, unconventional models usage improves the level of accuracy of the computations. Moreover, it is not possible to indicate a single model able to predict the complex thermal field correctly at all conditions, even if the algebraic anisotropic correction to SST model results to be the most reliable in case of multi perforated plate. On the other hand, the necessity of such turbulence formulation of a clear definition of development coolant streamlines to correct the lateral jest spreading, results in a difficult application to film-cooled blades and nozzles study, where the coolant pattern is not known a priori.

Finally, some advises about meshing characteristics can be provided. Referring to Section 2.4.4, the tetrahedral mesh counting about 7.2 million elements (Mesh C in Figure 2.9) is the results of a grid independence study. Hence, in order to achieve a reliable single-hole discretization, about 1 million elements for each hole are necessary.

Chapter 3

Film cooling model: *FCM*

In this chapter, the developed film cooling model, called FCM, is presented. After a literature review about the state of the art of film cooling modelling, details about FCM and its implementation are provided in order to better understand its features and peculiarities.

3.1 Literature review

The need to increase gas turbine efficiency, component life, and engine output results in a more ample use of film cooling in the design of gas turbine vanes and blades. As the use of film cooling itself counteracts the positive effect on engine efficiency due to cooling air bypassing the combustion process, it is necessary to use film cooling flows as efficiently and sparingly as possible. The obvious requirement for the design process of film-cooled components is a predictive capability for film-cooled surface temperature and adiabatic effectiveness values with high level of confidence. In the framework of CFD, this has to be achieved with manageable computational effort. Fully resolving the film cooling flows, is theoretically possible as has been shown by Goormans-Francke et al. [76] but is not feasible in a design environment from an economical standpoint. The development of a method to simulate film cooling flows in 3D-CFD without having to fully resolve the flow inside the cooling holes premises to mitigate

this issue.

One of the first attempts to model film cooling avoiding the complete discretization of film cooling holes can be attributed to Crawford et al. [77] and Miller and Crawford [78]: they implemented a model for the coolant injection in a 2D boundary layer code. More recently, approaches in 3D-CFD have been presented.

Heidmann and Hunter [79] investigated the possibility to account for film cooling through the use of source terms. They identified problems related to introducing source terms only at the wall similar to an inlet boundary condition. A model was proposed using uniformly distributed source terms at some finite distance from wall to overcome the problems

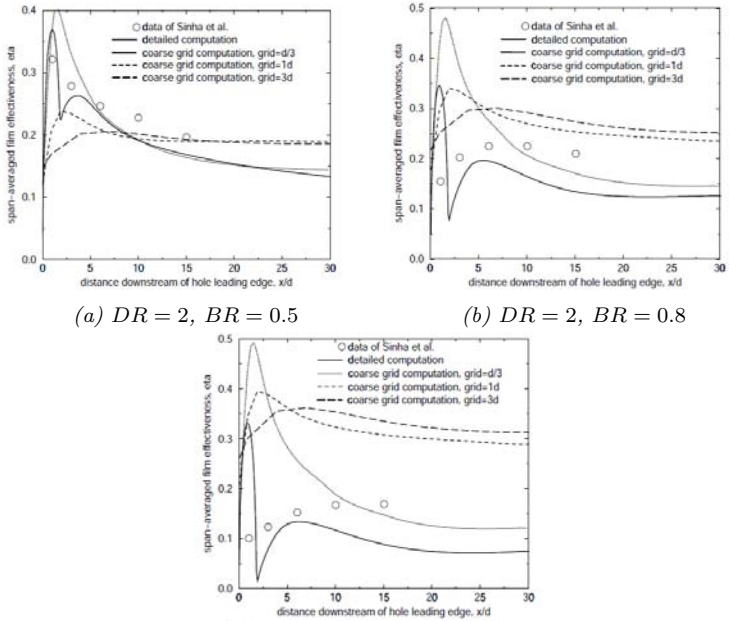

(a) $DR = 2,\ BR = 0.5$ *(b)* $DR = 2,\ BR = 0.8$

(c) $DR = 2,\ BR = 1.0$

Figure 3.1: Heidmann's model: comparison of span-averaged effectiveness for thick source term model (Source [79])

related to the use of wall-adjacent sources. They found an inability of their model to capture the jet detachment that causes the lower effectiveness values in the data and detailed calculation. This might be remedied through a more realistic distribution of source terms, instead of the uniform distribution of the present model (Figure 3.1).

The model by Burdet et al. [80] uses an injection model in which the coolant flow is injected into the domain through a plane of injection, quite similarly to an inlet boundary condition. The plane of injection extends into the main flow boundary layer and it is oriented almost orthogonal to the main flow direction. Upstream of this plane of injection, the main flow blockage effect of the injected film is accounted for using an immersed free-slip adiabatic wall boundary condition: this BC forms a hood-shape as an obstacle to the main flow boundary layer (Figure 3.2). Downstream of this hood lies the plane of injection. Even if their model gives an accurate representation of the jet aero-thermal flow field at the plane of injection, its downstream evolution and diffusion is subject to complex flow phenomena, resulting in a worst agreement with experimental results (Figure 3.3).

More recently, two modelling approaches have been proposed by Tartinville and Hirsch [81]. The first one uses a stub of a film cooling hole, which is attached to the main flow computational domain using a non-matching grid interface. At the inlet of the stub, appropriate boundary

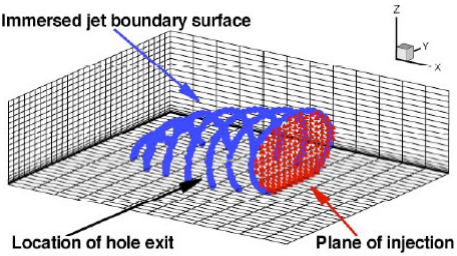

Figure 3.2: Burdet's model: example of a coolant jet boundary surface immersed in a mesh (Source [80]).

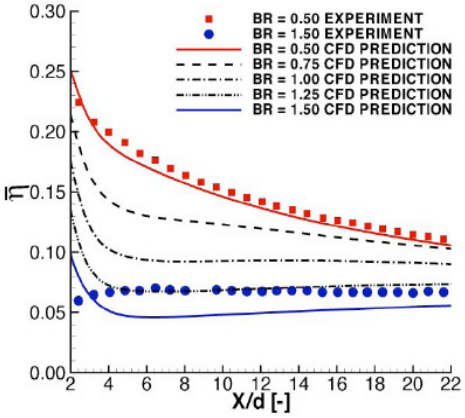

Figure 3.3: Burdet's model: predicted and measured laterally averaged wall adiabatic effectiveness (Source [80])

conditions are applied, injecting the flow into the fluid domain. Alternatively, an approach adding source terms as fluxes to cell faces above the cooling hole exit has been investigated. Results of their model applied to a film-cooled flat plate test case (Figure 3.4) show that, whatever approach is used, the lateral spreading of the plume is underestimated just downstream of the injector. However such an under-estimation appears to be more sensitive on a convex wall (for example a blade pressure side) than on concave wall (blade suction side). The local source term treatment is also able to capture the kidney vortices that appear for a jet in a cross-flow. Furthermore, when refining the mesh, the local source term approach converges towards the full meshing solution.

auf dem Kampe and Völker [82] proposed a model to simulate flows ejected from cylindrical film cooling holes in 3D-CFD, describing the film-jet in terms of its shape and the distribution of temperature and velocity components within the film-jet body, using a correlation-based prediction of the complete three-dimensional flow field in the proximity of a film hole exit based on characteristic film cooling parameters presented in [83]. They found a very good agreement between detailed CFD calculation and

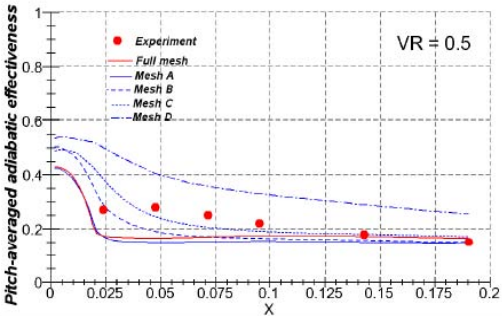

(a) $VR = 0.5$

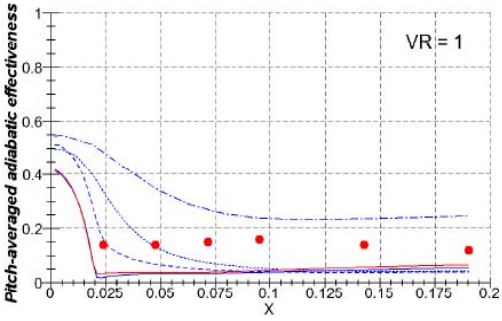

(b) $VR = 1$

Figure 3.4: Tartinville's model: measured and computed stream-wise distribution of pitch averaged adiabatic effectiveness (Source [81])

film cooling model results, in terms of temperature distribution (Figures 3.5 and 3.6), for both high and low BR values. In both cases, the quality of their film cooling model prediction within the first 20 hole diameters downstream of the ejection location is good. Further downstream, some offset is noticeable: the cooling effect in the low blowing ratio case is slightly underpredicted in the far-field, while, in the high blowing ratio case, the cooling effect due to film-jet re-attachment in the far-field is overpredicted. However, their model results show its ability to apparently correctly capture the jet lift-off behaviour characteristic of the high blowing ratio case with no lateral inclination. Finally, they found how the film

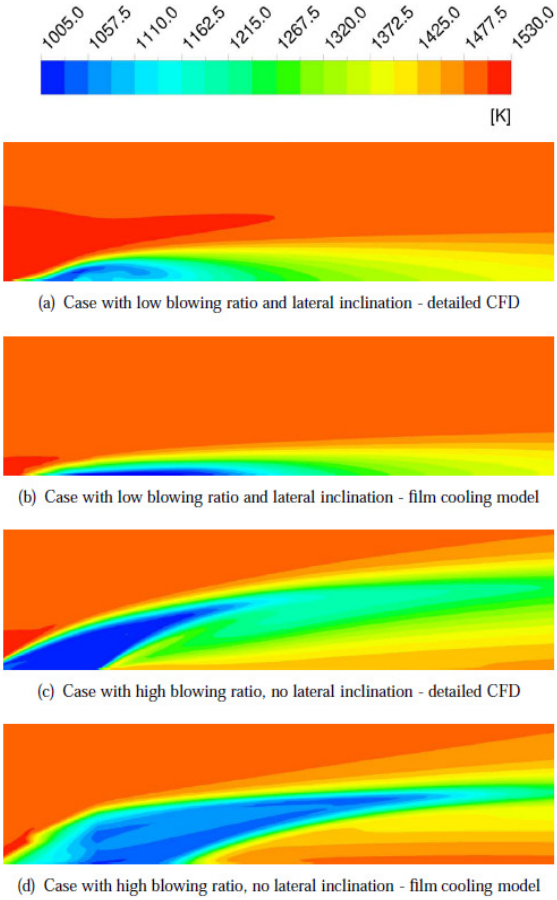

Figure 3.5: Auf dem Kampe's model: temperature distributions in a meridional cut-plane (Source [82])

cooling jet penetration into the main flow boundary layer is correctly captured using the film cooling model (Figure 3.5).

Finally, Andreini et al. [84] presented a method to study effusion cooling, consisting of an array of closely spaced discrete film-cooling holes. Their model, named *SAFE* (*Source bAsed eFfusion modEl*), replaces

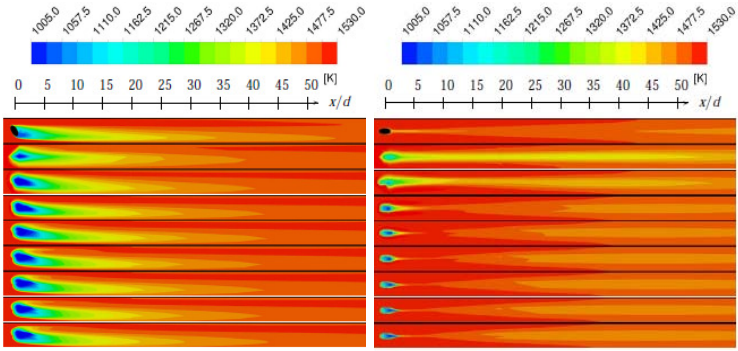

(a) Low blowing ratio case *(b) High blowing ratio case*

Figure 3.6: Auf dem Kampe's model: surface temperature prediction of detailed CFD (top) and film cooling model with meshes using 1, 2, 3, 5, 7, 10, 20 nodes per diameter and the detailed reference mesh, at the bottom (Source [82])

the effusion hole with a mass sink on the cold side of the plate, a mass source on the hot side and a heat sink (considering the convective effect within the perforation) inside the liner's solid. They also implemented an automatic calculation of the mass flow through each hole, obtained by a run time estimation of isentropic mass flow with probe points, while the discharge coefficients are calculated at run time through an in-house developed correlation. From the comparison between discrete hole and source point application results (Figure 3.7) it is possible to notice that the resulting injection angle is quite different, and consequently the coolant protection on the plate. Authors ascribed this effect to the application of the source point within the prism layer, close to the wall, which seems to make the injection angle almost orthogonal. In Figure 3.8, the comparison between experimental data and the Andreini et al.'s source-based methodology is reported: it is possible to notice how the local pressure drop based formulation gives very similar results with respect to the case with prescribed values, having the advantage of a limited number of inputs required. On the other hand, authors pointed out how the latter

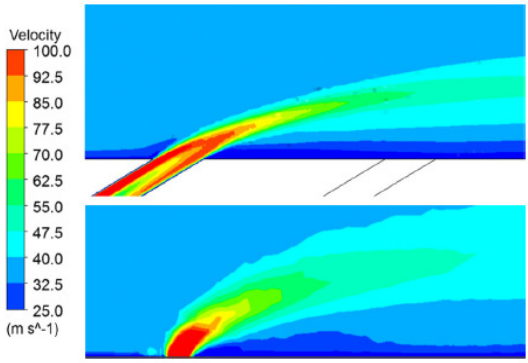

Figure 3.7: SAFE model: comparison of the flowfield in presence of discrete holes (top) and source points (bottom) (Source [84])

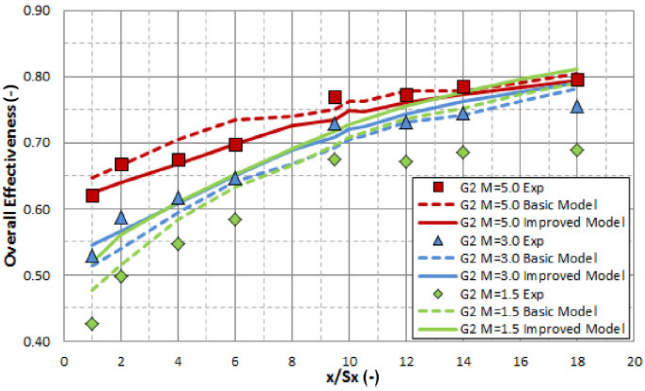

Figure 3.8: SAFE model: comparison between experimental data and source model: effect of blowing ratio (Source [84])

approach implies a strong dependence on the accuracy of the way the inputs (necessary to the application of their model) are estimated.

The model presented in this work places itself as a middle approach between the last two presented, including the volume injection approach with the coolant mass and proprieties calculated by an external correlative

approach. The proposed film cooling model allows a more simplified approach than the one by auf dem Kampe and Völker [82], not introducing a spatial distribution of the coolant proprieties inside the injection volume. Such an improvement would be at the expense of the simplicity of the present model, since it would require knowledge of the distribution of the source terms for various blowing ratios and geometry configurations. Compared to the model by Andreini et al. [84], the application of source terms inside a volume of elements than inside a single element containing the point of injection (source point) leads to a more complex and complete discretization.

3.2 Model Formulation

A mass source term $\mathcal{S}_{MS}$ is used in order to introduce the coolant flow into the domain. Source terms of mass are defined in a confined volume around the film hole location, consisting of a multiple finite volumes (elements of the mesh) depending on mesh resolution. Three-dimensional velocity and temperature fields (as well as turbulent kinetic energy and eddy frequency) are modelled within this source volume by imposing velocity and temperature values to the mass source terms. The continuity equation with the source term is given by:

$$\frac{\partial \rho}{\partial t} + \frac{\partial \left(\rho u_i\right)}{\partial x_i} = \mathcal{S}_{MS} \tag{3.1}$$

The contribution of the mass source term $\mathcal{S}_{MS}$ to the momentum and total energy equations is accounted for as shown below:

$$\frac{\partial \left(\rho u_i\right)}{\partial t} + \frac{\partial \left(\rho u_i u_j\right)}{\partial x_j} = -\frac{\partial p}{\partial x_i} + \frac{\partial \tau_{ji}}{\partial x_j} + \mathcal{S}_{MS} u_{MS,i} \tag{3.2}$$

$$\frac{\partial E}{\partial t} + \frac{\partial \left(u_i E\right)}{\partial x_i} = \frac{\partial u_i \tau_{ji}}{\partial x_j} - \frac{\dot{q}_i}{\partial x_i} - \frac{\left(p u_i\right)}{\partial x_i} + \mathcal{S}_{MS} \frac{E_{MS}}{\rho_{MS}} \tag{3.3}$$

where $u_{MS,i}$ denotes the velocity vector and E_{MS}/ρ_{MS} the ratio of total energy to density that is associated with the mass source. The total

energy E is calculated as:

$$E = \rho \left(e + \frac{1}{2} u_i u_i \right) \tag{3.4}$$

where e is the specific internal energy defined as

$$e = (c_p - R)\, T \tag{3.5}$$

with c_p the specific heat capacity at constant pressure, R the specific gas constant and T the temperature.

In this application of the model, $\mathcal{S}_{MS}$, $u_{MS,i}$ and T_{MS} are estimated through external approaches and so they are inputs of the model. As mentioned before, source terms are assigned within a source volume. In this formulation, it is possible to chose among three different shapes: source point discretization (a replica of the method presented by Andreini et al. [84]), cylindrical and delimited cylinder shapes.

The resulting high mass flow density in the source volumes displaces the main flow in approximatively the same way as the real jet-film would. Clearly, at the source volume boundaries, momentum and energy exchange is permitted, allowing the immediate development of shear layers between film-jet and cross-flow boundary layer.

For the present model formulation, the mass source term, as well as velocity, temperature and turbulence proprieties terms, is uniformly distributed across any given source volume.

The current implementation of the film cooling model uses SST turbulence by Menter [85], in its formulation provided in ANSYS® CFX v. 14.0. A more sophisticated approach for the turbulent quantities is left for future model improvement.

3.3 User subroutines in ANSYS® CFX

In ANSYS® CFX, it is possible to apply a native approach to source terms application, The code, in fact, allows the application of source points within the domain: the specified source is distributed among the

vertices of the element in which the point is located, hence the effect of the source will therefore become more pronounced as the mesh is refined. This is the approach adopted by Andreini et al. [84]. However, as already said, the limit of this methodology is both its excessive discretization (only one element per hole) and its high memory requirements needed by the expressions and variables created by the code when such methodology is applied.

To overcome these limits, the present film cooling model has been implemented in the code using user subroutines, written in Fortran: effectively, CFX allows to add additional features and physical model, calling these routines through a source code interface.

In CFX, two different kind of user routines are available [86]:

- user defined CEL (CFX Expression Language) functions;
- junction box routines.

3.3.1 User defined CEL funcions

Basically, user CEL functions allow to create customized functions in addition to the predefined CEL functions inside CFX. A user CEL function passes an argument list to a subroutine written by the user, and then uses the returned values from the subroutine to set values for the quantity of interest. In Figure 3.9, a streamlined representation of user function implementation in CFX is depicted. All variables that are available for use in standard CEL expressions are also available for use in user CEL expressions.

User CEL functions have fixed argument list that contains the following data fields [86]:

- NLOC: number of location in space over which the calculations have to be performed;
- NARG: number of arguments passed to the function;
- ARGS(1:NLOC,1:NARG): arguments passed to the function (at each point in space);

- NRET: number of return variable (always 1);
- RET(1:NLOC,1:NRET): return variables (at each point in space);
- character, double precision, integer, logical and real stacks.

The length (NLOC) of the arguments (ARGS) and the return value (RET) of user CEL functions is determined by the *locale* for which the routine is called: for example, for an internal element group, NLOC is the number of vertices in the current *locale*. In general, a user CEL function is called several times during each iteration and the value value of NLOC could be different for each call: this is because the CFX-Solver splits the specified region (for example, an internal region) into a number of 'smaller' parts (called *locale)* and calls user functions for each part.

Regarding the units of ARGS and RET, on entry into a user CEL

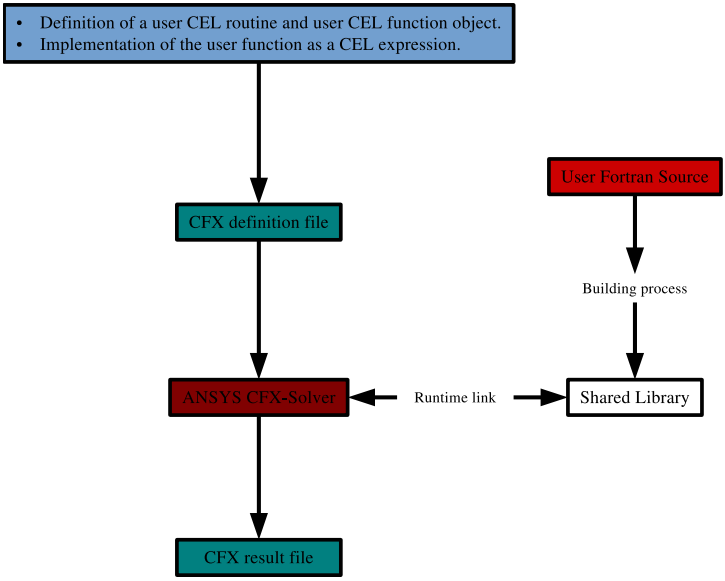

Figure 3.9: User function definition and implementation in CFX

function routine, the arguments are automatically converted into the units specified by the user in the User Function Editor (in CFX-Pre). On exit, the results are automatically converted from the results units into the solution units (specified by the user in CFX-Pre) used by the CFX-Solver.

3.3.2 User junction box routines

In addition to defining user CEL functions (called at each iteration), it is possible to call user subroutines at several points during execution of the CFX-Solver: this subroutines are called junction boxes. Junction boxes can be used to accomplish several tasks, for example to control input/output of user data, allocate memory for user defined variables (accessing internal data structures of CFX-Solver) and so on. It is important to remember that junction box routines have no access to CEL variables.

3.4 Implementation of the model

In order to use the film cooling model with ANSYS® CFX, several steps have to be taken during the run definition in CFX-Pre:

- Creation of *user routines objects* to link the film cooling model User Fortran code to the CFX case definition.
- Creation of *user function objects* that in turn refer to the previously specified user routines objects. In this step, it is necessary to specify arguments and result units.
- Definition of *additional variables* fields for $\mathcal{S}_{MS}$, $u_{MS,i}$, T_{MS}, $cool_{MS}$, ω_{MS} and k_{MS} (see section 3.4.1).
- Definition of a *subdomain* object, that covers the entire fluid domain (see section 3.4.1).
- Specification of a *continuity source* for the subdomain. In the input fields for mass source, temperature, velocity components, turbulence and passive scalar, the respective additional variables have to be referenced.

Table 3.1: FCM: necessary inputs for each hole

Input	**Unit**
injection point coordinates	$[m]$
perforation radius	$[m]$
injection angle	$[^\circ]$
compound angle	$[^\circ]$
CD	$[-]$
mass-flow	$[m\ s^{-1}]$
exit pressure	$[Pa]$
exit temperature	$[K]$
injection volume	$[-]$
turbulence level	$[\%]$

In order to simplify the implementation, all the above steps have been automated in the form of a CFX Command Language (CEL) script.

Boundary conditions required by the film cooling model are specified outside of the CFD environment in a text file, read by the junction box at the beginning of the solver run. The informations contained inside the text file are stored in memory stacks within CFX-Solver itself, making them available to all the user subroutines and, in case of a parallel run, to all the partitions.

In case of a run coupled with an external network solver (from which film cooling data are recovered), the required boundary conditions (reported in Table 3.1) are: the geometrical coordinates of the exit point of each hole, the perforation radius, two geometrical perforation angles (injection and compound angle), discharge coefficient, $\dot{m}$, pressure, temperature and the injection volume shape.

In effect, these changes cause the CFX-Solver to make calls to the defined User Functions when running. For each *locale*, a call is made to the particular user subroutine and the nodal coordinates (of the vertices inside the *locale*) are passed as input to these functions. During the first iteration of the run, the code identifies whether or not each element resides inside the injection volume of each hole, and consequently stores

the informations of the positive element vertices: at these vertices, the user defined source terms will be assigned. These informations are stored inside the memory stacks, so for the next iterations all the subroutines will search vertices associated to source terms inside the proper stack. It is important to highlight that current implementation is not solution-dependent: all proprieties and volume shapes are provided by the user. It is however possible to introduce dependencies on the current state of the flow solution, requiring a runtime update of the source terms. This functionality will be implemented in future releases of the code.

3.4.1 Additional variables and user subroutines

As explained above, there are many additional functions as many user subroutines implemented in CFX. During the run, some informations are stored inside memory stacks: in fact, some subroutines need output coming from other subroutines as input to calculate the proper additional variables.

Every subroutine is composed by a similar structure. There is a first part in which the argument list and variables allocation are present, followed by BC informations recovering from the proper stack. Then, there is the execution of the volume individuation process (only in case of *Mass-flow* usersub) or recovering of elements information, storing internally elements vertices informations.

In total, there are 8 subroutines: in Table 3.2, the necessary inputs and outputs of each subroutine are reported. A summary of user-subs characteristics follows.

Mass-flow This is the main subroutine: since mass equation is the first equation solved by CFX-Solver, this is the first called usersub. Hence, during its execution on the first call, the informations about the element vertices interested by general source application (i.e. inside the injection volume discretization) are stored in memory stacks, from which the other subroutines recover information, avoiding useless and time-consuming calculations. Obviously, this sub provides the assignment of mass-flow

Table 3.2: FCM: user subroutine inputs and outputs

Usersubroutine	**Inputs**	**Outputs**
Mass-flow	Hole inputs	$\dot{m}$ element vertices V
Velocity components	Hole inputs V	V_x V_y V_z
Temperature	Hole inputs	T
Turbulent kinetic energy	Hole inputs V	k
Eddy frequency	Hole inputs k	ω
Coolant	Hole inputs	*Coolant*

values for each vertex associated to a hole. Finally, this sub evaluates the velocity magnitude, used as input by other subroutines, as:

$$V = \frac{\dot{m}}{\rho_{out}\frac{\pi}{4}D_h^2} = \frac{\dot{m}}{\frac{o}{RT_{out}}\frac{\pi}{4}D_h^2} \tag{3.6}$$

where all the coolant proprieties are retrieved from input file.

Velocity components There are three user subroutines each one associated to a velocity component. Components values are computed from velocity module (Equation 3.6) and perforation angles (input text file, Table 3.1).

Temperature This sub recovers temperature value from input text file, associating it to the positive elements vertices.

Required turbulence quantities There are as many turbulence quantities as many needed by the particular chosen turbulence model. In case of $k-\omega$ SST model, to author's knowledge, no correlations are available

in open literature to estimate turbulence quantities at hole discharge. Therefore this quantities (turbulence kinetic energy k and turbulence eddy frequency ω) are evaluated as (referring to ANSYS® CFX manual [86]):

$$k = \frac{3}{2} V^2 T u^2 \tag{3.7}$$

and

$$\omega = \frac{\varepsilon}{k} \tag{3.8}$$

where

$$\varepsilon = \frac{k^{3/2}}{0.3 D_h} \tag{3.9}$$

Coolant In order to track the coolant distribution, a transport equation for an additional passive scalar *Coolant* representing coolant concentration was solved. This user subroutine assigns the value 1 at the elements vertices inside the injection volumes of each hole. The value of its kinematic diffusivity was specified to guarantee a Lewis number (Le) equals to 1 with the aim of fully respecting the mass-energy transfer analogy.

3.4.2 Injection volumes

As will be explained in the validation chapter, two different injection volume shapes are available in the film cooling model: a cylinder shape (Figure 3.10a) and a delimited cylinder shape (Figure 3.10b). The first

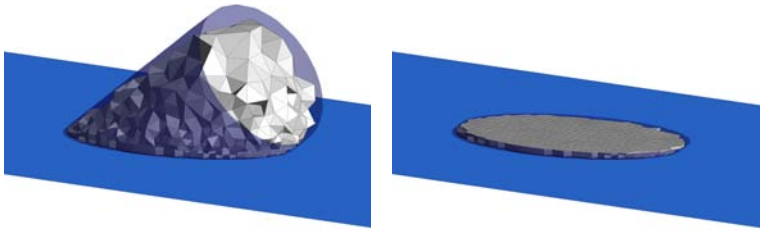

(a) Cylinder volume. *(b) Delimited cylinder volume.*

Figure 3.10: Different injection volumes available in FCM

shape is a cylinder oriented along the same axis of the perforation and extended until the edge of the hole. The second shape is the same of the previous, but delimited from the surface of injection by a fixed distance of 5% of the hole diameter, resulting from a preliminary sensitivity analysis.

This two shapes were originally intended to represent the mass addiction regime (*delimited cylinder*) and the penetration regime (*cylinder*). However, as will be demonstrated, the first one has proven a very good ability to reproduce full hole discretization results then the second one for different geometries and boundary conditions.

3.5 Final remarks

The developed film cooling model has been presented: it allows to estimate adiabatic effectiveness through the introduction of a volume injection approach, avoiding the meshing process of perforations. Coolant mass and proprieties calculated by external tools. The proposed film cooling model allows a simplified approach, not introducing a spatial distribution of the coolant proprieties inside the injection volume. The model has been implemented inside the commercial code ANSYS® CFX.

Chapter 4

FCM validation: flat plate test cases

In this chapter, the presented film cooling model will be tested and validated against the experimental data and the complete CFD analyses presented in Chapter 2, in terms of adiabatic effectiveness profiles and distributions: only SST turbulence model results are recovered, since *FCM* implementation in ANSYS® CFX relies on this turbulence model. Furthermore, the influence of both elm/D values and injection volume shape is studied.

4.1 Single row plate

The first test case is the same case reported in Section 2.3: it consists of a flat plate cooled by a row of inclined holes.

4.1.1 Film cooling model setup

Concerning the film cooling model setup, in Figure 4.1, the exploited numerical domain is reported: in this case in order to better represent the coolant jet the half hole symmetry condition has not been applied.

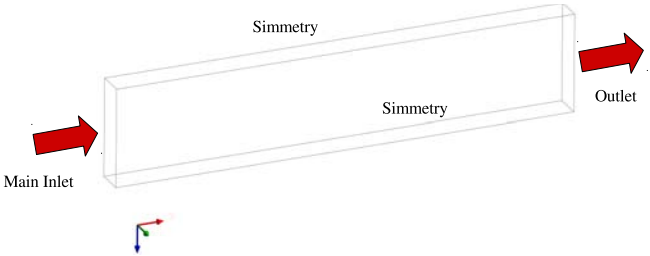

Figure 4.1: FCM computational domain (single row test case)

Following the setup presented for the complete hole study, the mainstream boundary conditions have been assigned in terms of mass flow rate, total temperature and turbulence quantities at the main inlet and static pressure at the outlet (Figure 4.1).

Regarding coolant proprieties and conditions applied as boundary conditions to the model, values are recovered from the complete hole analysis.

Three different mesh refinements have been tested, looking for indications about the minimum element per diameter (elm/D) value to be applied in order to discretized the coolant volume of injection. In this particular case, since its geometrical simplicity, the mesh refinement has been applied to the whole wall interested by the coolant injection, keeping unchanged the other parameters associated to the mesh. Furthermore, the influence of volume injection shape (cylinder or delimited cylinder) has been investigated. Informations about exploited numerical grids are reported in Table 4.1.

Table 4.1: Mesh dimension for film cooling model (single row test case)

elm/D	**mesh dimension**
5	$92 \cdot 10^3$ nodes
10	$353 \cdot 10^3$ nodes
20	$1393 \cdot 10^3$ nodes

4.1.2 Results

First of all, it is important to highlight some particular features of the studied perforation.

As presented in Section 2.3, the studied perforation is very short: it presents a l/D value of 3.5. In this way, the coolant has no capability to develop inside the hole. At the exit of the hole, indeed, strong non-uniformities are present: on the left side Figure 4.2, the dimensionless velocity values on a plane parallel to the wall are represented, highlighting inhomogeneities in terms of velocity distribution. On the right side of Figure 4.2, the flowfield inside the hole is represented: it displays the main peculiar features of jet, as above explained in Chapter 1. For this reason, film cooling modelling application without taking into account the injection non-uniformity depicted in Figure 4.2, is expected to have a strong impact on predictability of film cooling coverage. In addition, as can be seen in the picture, the effect of the real angle of injection is to be considered: in the application of film cooling model, inside the injection volume the velocity components are imposed to have the geometric angle. However, the real angle with which coolant penetrates inside the mainstream, is different from the geometric one (Figure 4.2), and generally it can be considered function of various parameters, such as BR and DR.

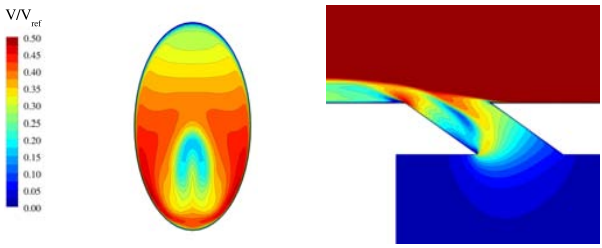

Figure 4.2: Complete hole discretization: velocity distribution on hole exit (left) and symmetry plane (right) (single row test case)

As can be seen in Figure 4.3 and 4.4, where the η_{aw} distribution on hole meridional plane and on the wall is reported for all the studied model application, there are strong influences of both injection volume shapes and mesh discretization. The complete hole results are the SST case ones

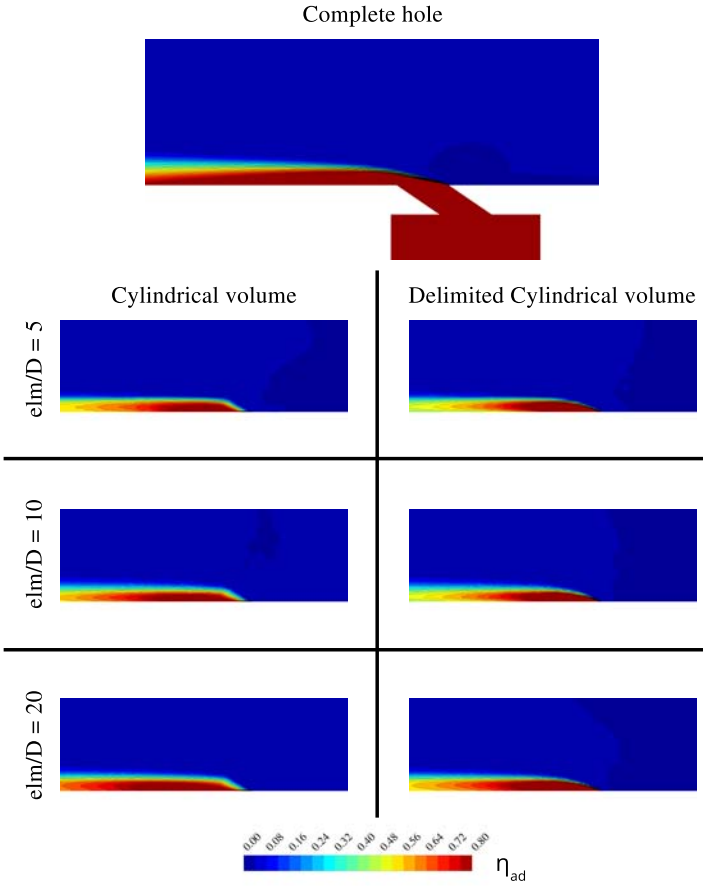

Figure 4.3: Adiabatic effectiveness distribution on hole mid-plane (single row test case test case)

of Section 2.3.

Regarding the volume shape, it is possible to highlight how cylindrical volume results to be too wide to discretize a jet at low BR (as in this case): this is a regime of mass addition, jet is bended towards the wall and hence this kind of shape reveals to be not-physic. However, the delimited cylinder shape does not guarantee a good prediction due to the strong jet non-uniformity coming out the hole.

As to be expected, the number of elements per diameter length used to represent the hole (elm/D parameter) and hence the mesh refinement,

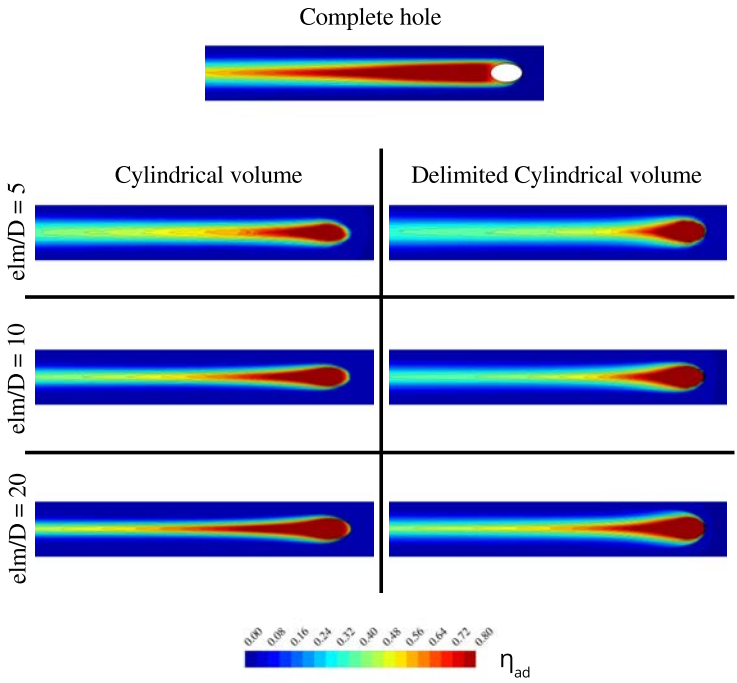

Figure 4.4: Adiabatic effectiveness distribution on wall (single row test case test case)

heavily affects coolant distribution and penetration for the same injection volume: for more coarse mesh, results show how the numerical diffusivity generated by the mesh leads to a more bended jet.

From a quantitative point of view, looking at Figure 4.5, the span-averaged adiabatic effectiveness profiles are presented for all cases: in addition to experimental, film cooling model and SST complete hole discretization, the algebraically corrected SST turbulence model (SSTA) results are reported (see Section 2.2.1). For all the cases, the jet imprint on the wall does not extend as the complete hole SST case (as depicted also in Figure 4.4, leading also an overestimation of experimental values. However, even if some differences arise especially near the hole (due to the critical stressed above), film cooling model application results are aligned to data retrieved from simulation exploiting film cooling modelling similar to the presented one (Figure 3.1).

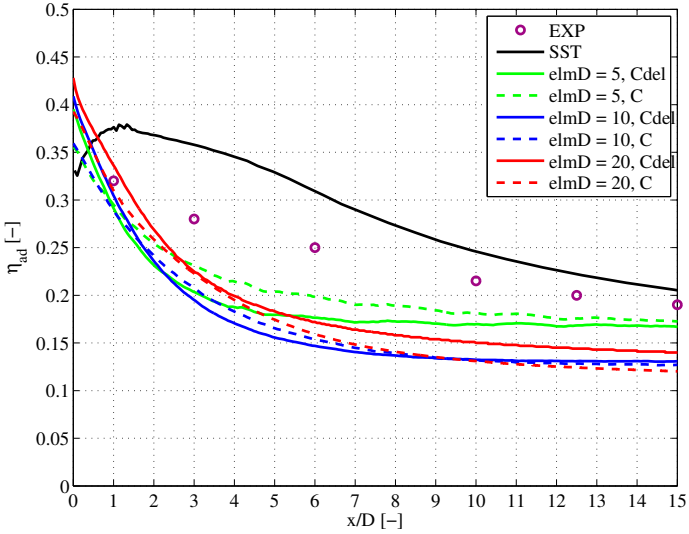

Figure 4.5: Span-wise averaged adiabatic effectiveness (single row test case)

4.2 Multi row plate

The next step is to extend the validation of the film cooling model to a more complex geometry. Hence, it is been decided to test the model predicting capability applying it to a multi-perforated plate described in Section 2.4, introducing the superposition effect since more than one row of holes is considered. Furthermore, it will be investigated blowing ratio values ranging between 0.5 and 2.

4.2.1 Film cooling model setup

In this analysis, only the highest tested turbulence intensity ($Tu = 17\%$) has been taken into account. Furthermore, plate has been tested with several blowing ratios (BR) conditions (0.5, 1.0, 2.0). The full test matrix of the simulations performed in the present work is summarized in Table 4.2.

The main-stream boundary conditions have been assigned in terms of total pressure, total temperature and turbulence quantities at the main inlet, mass flow rate and total temperature are specified at the coolant inlet and mass flow rate was fixed at the outlet.

Regarding film cooling model setup, three elm/D values have been studied (5, 10 and 20 elm/D ratios) in order to analyse the influence of hole discretization on adiabatic effectiveness prediction. Also, a sensitivity analysis has been conducted in order to verify the importance of injection volume shape. The mesh strategy is the same of the complete hole

Table 4.2: FCM: test matrix of performed simulations (multi row test case)

BR [−]	DR [−]
0.5	1
1	1
	1.5
2	1

Table 4.3: Mesh dimension for film cooling model (multi row test case)

elm/D	**mesh dimension**
5	$1.2 \cdot 10^6$ elements
10	$3.5 \cdot 10^6$ elements
20	$12.1 \cdot 10^6$ elements

run: the only difference is the application of mesh refinements located in correspondence of the holes on the surface, resulting in grids ranging from 1.2 million elements ($elm/D = 5$) to 12.1 million elements ($elm/D = 20$). In Table 4.3, the exploited mesh characteristics are reported. In this application, coolant boundary conditions are retrieved from complete hole analysis. It is important to remember that for the computations with the full meshing of the cooling hole (Section 2.4) a 7.2 million elements mesh (half-hole study) has been exploited.

4.2.2 Results

In this section, the results of film cooling model application are reported, posing particular attention to the model discretization at various BR values. Adiabatic effectiveness profiles and distributions are the yardstick of model reliability against complete hole study.

4.2.2.1 $BR = 0.5$ case

In Figure 4.6, the coolant distributions on the meridional plane of odd holes (1^{st}, 3^{rd} and so on) are reported for all studied cases (various elm/D ratios and injection volume shapes) compared to the complete hole study. In case of cylinder injection volume, it is possible to observe that the coolant jet does not lift off from the wall, and so it remains attached to the surface: this is mainly related to the uniform distribution of the source terms inside the volume. On the contrary, the delimited cylinder injection, not superimposing a distribution in the domain of the evolving jet, but only in a small portion near the wall, allows the coolant

to detach from the surface in the final part of the plate (due to effect of the previous jets) but also in the first part. This is particularly true increasing the elm/D ratio: a better discretization of the perforations

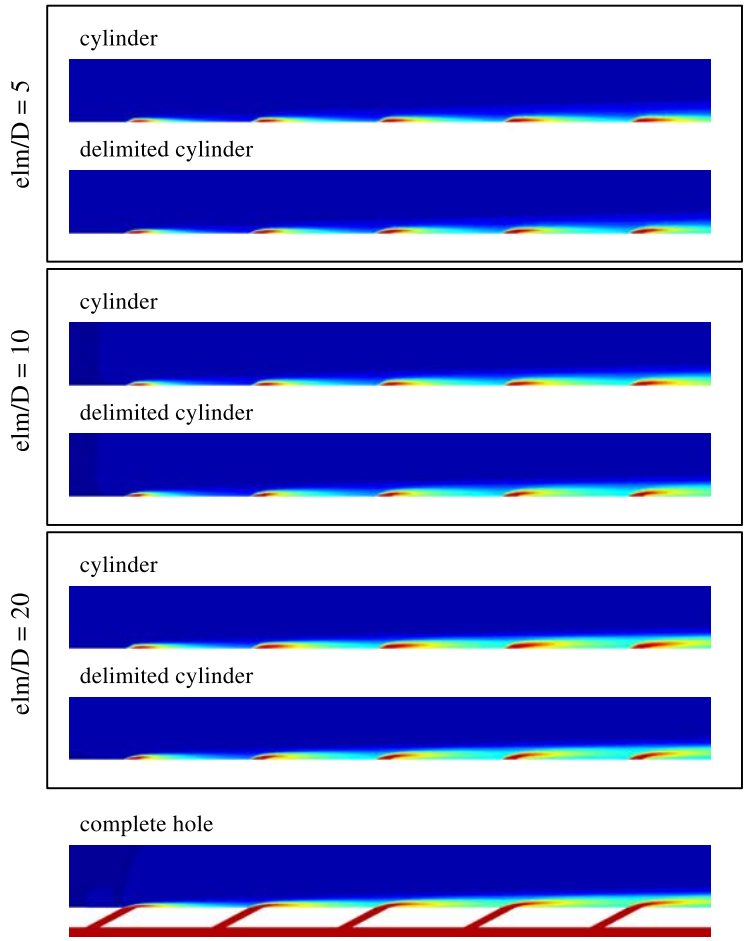

Figure 4.6: Multi row test case: contour plot of coolant concentration on the meridional plane of odd holes ($BR = 0.5$, $DR = 1$)

leads to a jet shape more similar to complete hole one.

The clear underestimation of jet penetration can be seen also in the coolant traces on the wall (Figure 4.7): remaining attached to the surface, coolant jets overestimate the distribution prediction of the complete hole discretization, especially at lower elm/D values and for cylinder volume, leading to evident higher η_{ad} values at the end of the effusion plate.

The case that shows the better agreement is the one at $elm/D = 20$ with delimited cylinder injection volume: it is possible to observe how from a qualitative (jet shape in Figure 4.6, extension and development in Figure 4.7) and a qualitative (profile in Figure 4.8) point of view it

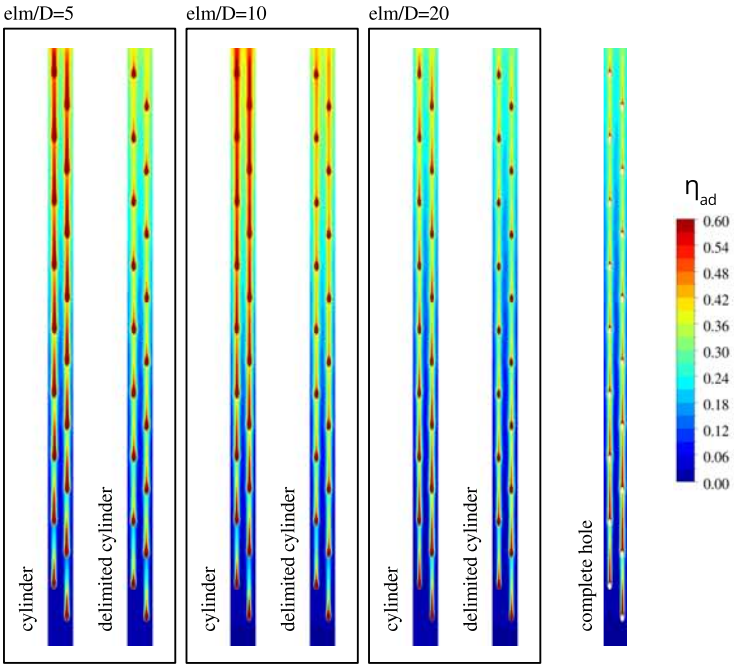

Figure 4.7: Multi row test case: adiabatic effectiveness distribution on the wall ($BR = 0.5$, $DR = 1$)

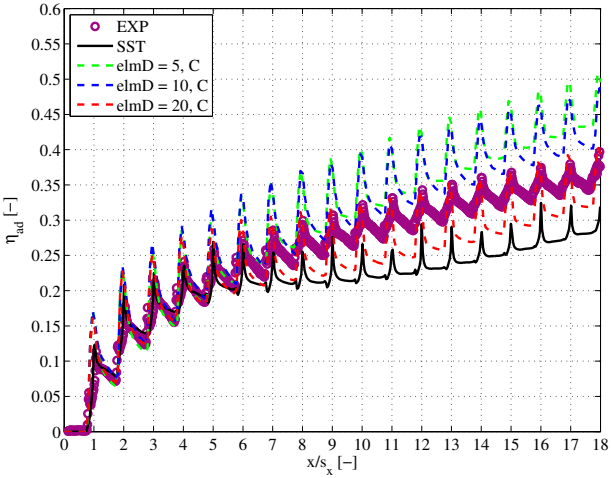

(a) Cylinder

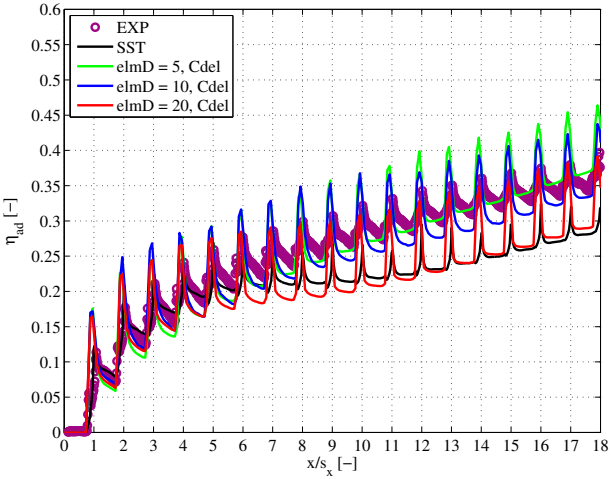

(b) Delimited cylinder

Figure 4.8: Multi row test case: span-wise averaged adiabatic effectiveness on the wall ($BR = 0.5,\ DR = 1$)

properly reproduces adiabatic effectiveness predictions coming from the complete hole discretization. In Figure 4.8 in fact, span-wise averaged η_{ad} profiles are reported for all the studied configurations, comparing them to experimental data: as can be seen, complete hole discretization (SST profile) reports a clear underestimation of experiment values, especially at the end of the effusion plate. This can be explained with the well-known underestimation of jet spreading and over-prediction of the penetration related to classical SST model, leading to injection of hot gases below the jet itself [68].

Film cooling model application, in terms of hole discretization (number of elements per diameter), well reproduces complete hole discretization results: the increase of elements leads to a less influencing numerical diffusion, translating in a better agreement with complete hole results. Regarding the injection hole shape, delimited cylinder one returns slightly over-estimation of complete hole SST profile until 11^{th} hole, successively the two profiles realign.

4.2.2.2 $BR = 1$ cases

Concerning $BR = 1$ case, looking at Figure 4.9 and 4.10, where η_{aw} distribution on side plane and wall respectively, for all studied cases is depicted, it is possible to observe the same behaviour described for $BR = 0.5$ case. The cylinder injection volume is not able to well reproduce the jet shape, leading to a underestimation of the lift off from the wall (especially at lower elm/D value) and hence to a overestimation of coolant effectiveness at the final part of the plate in respect to complete hole discretization. On the contrary, the delimited cylinder shape allowing the jet to detach from the surface, provides a good estimation of adiabatic effectiveness comparing to complete hole predictions, both in jet shape and coolant coverage on the wall, increasing the number of elements describing the perforation.

Furthermore, for this BR condition, the influence of DR has been verified. In Figures 4.11 4.12, the span-wise averaged profiles of η_{ad} are reported for $DR = 1$ and $DR = 1.7$ case, respectively, comparing

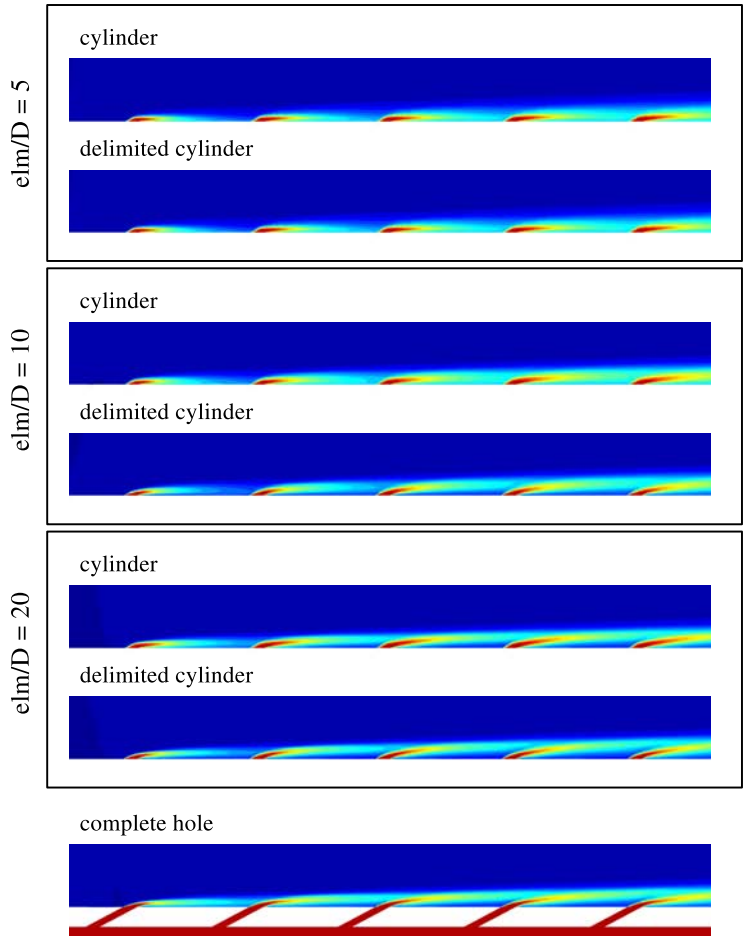

Figure 4.9: Multi row test case: contour plot of coolant concentration on the meridional plane of odd holes ($BR = 1$, $DR = 1$)

injection volume shapes and elm/D influence. Even in this case, the delimited cylinder case with the highest value of elm/D ratio results to be a very good approximation of the complete hole in terms of adiabatic

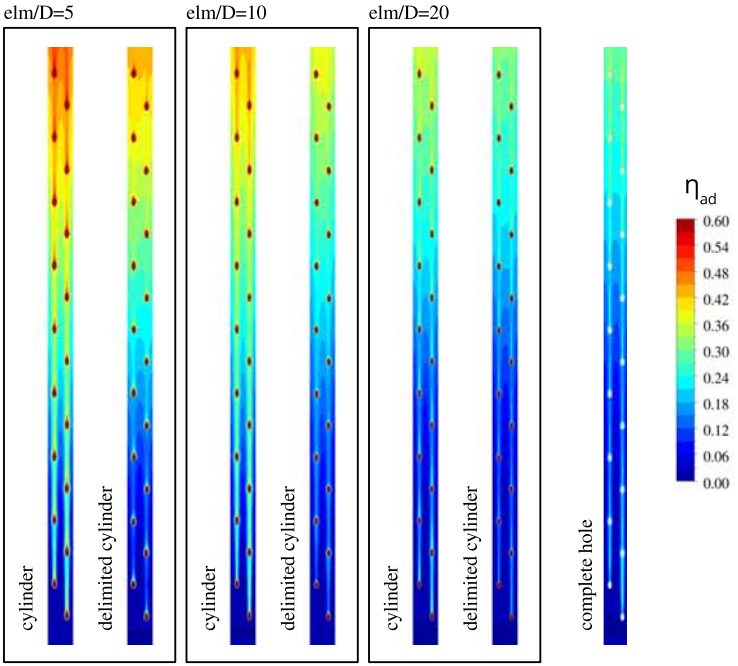

Figure 4.10: Multi row test case: adiabatic effectiveness distribution on the wall ($BR = 1$, $DR = 1$)

effectiveness averaged values and distribution.

4.2.2.3 $BR = 2$ case

At $BR = 2$, the regime is of complete jet penetration: increasing the BR value, in fact, jets detach completely from the wall and cooling effectiveness due to film protection strongly reduces, as can be seen for first rows of holes (Figure 4.13), since hot gas is attracted below the jet by the influence of kidney vortices. However, due to the higher coolant mass flow injected, the superposition effect is larger and the plate effectiveness is enhanced at the end of the plate (Figure 4.14).

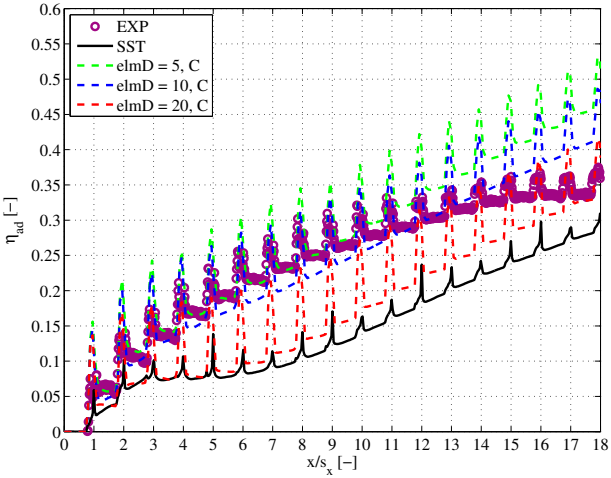

(a) Cylinder

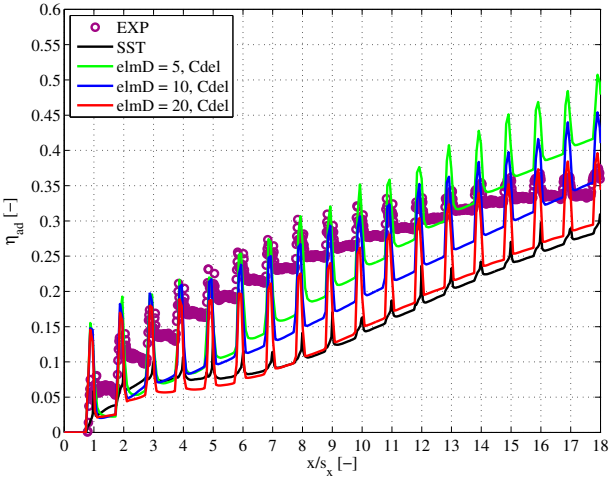

(b) Delimited cylinder

Figure 4.11: Multi row test case: span-wise averaged adiabatic effectiveness on the wall ($BR = 1$, $DR = 1$)

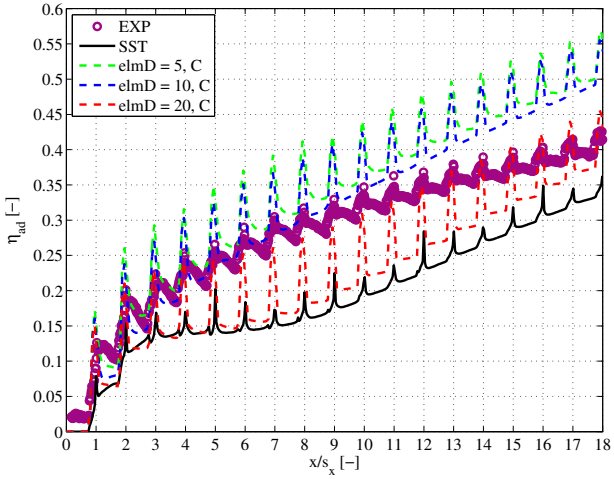

(a) Cylinder

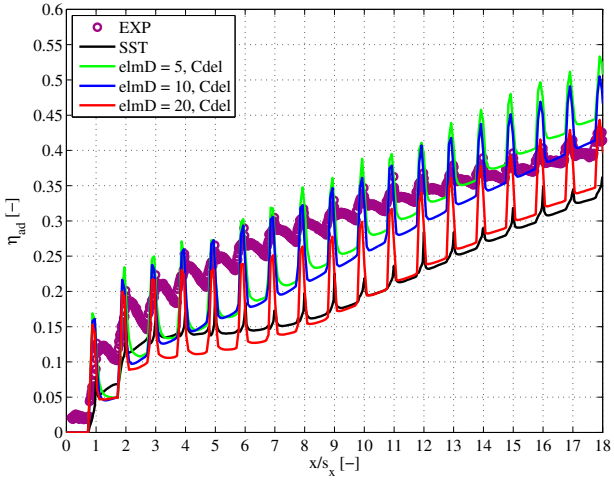

(b) Delimited cylinder

Figure 4.12: Multi row test case: span-wise averaged adiabatic effectiveness on the wall ($BR = 1$, $DR = 1.5$)

Even in this case, cylinder injection shape at lower elm/D value results to overestimate the η_{ad} value at the end of the plate, due to worst discretization of holes, translating in greater numerical diffusion.

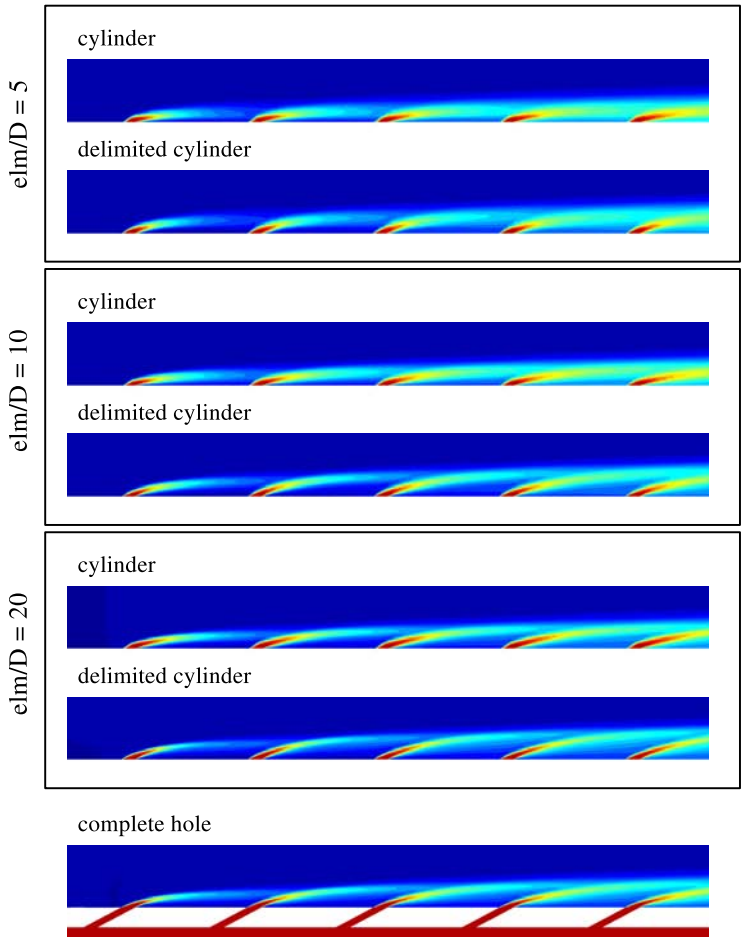

Figure 4.13: Multi row test case: contour plot of coolant concentration on the meridional plane of odd holes ($BR = 2$, $DR = 1$)

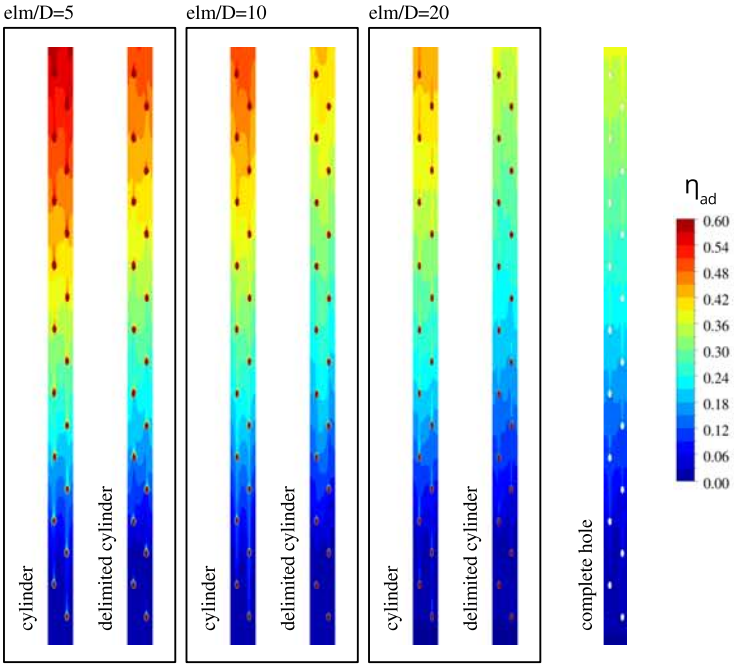

Figure 4.14: Multi row test case: adiabatic effectiveness distribution on the wall ($BR = 2$, $DR = 1$)

Delimited cylinder appears to be the better predictor of complete hole case.

At $BR = 2$, the regime is of complete jet penetration: increasing the BR value, in fact, jets detach completely from the wall and cooling effectiveness due to film protection strongly reduces, as can be seen for first rows of holes (Figure 4.13), since hot gas is attracted below the jet by the influence of kidney vortices. However, due to the higher coolant mass flow injected, the superposition effect is larger and the plate effectiveness is enhanced at the end of the plate (Figure 4.14). Even in this case, cylinder injection shape at lower elm/D value results to overestimate the

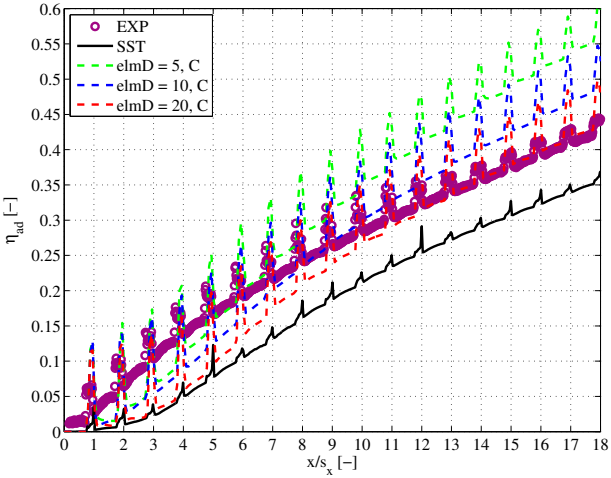

(a) Cylinder

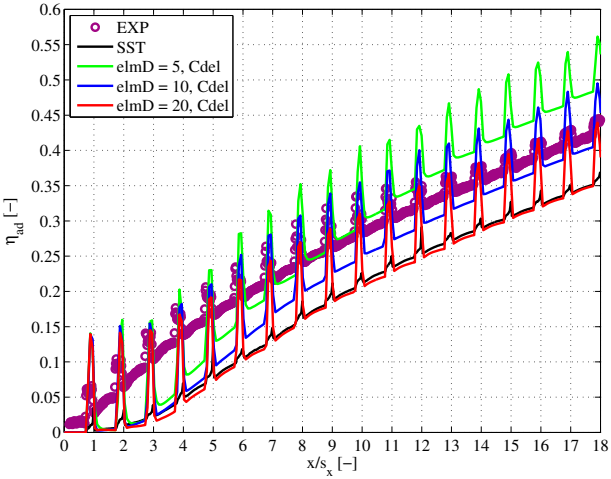

(b) Delimited cylinder

Figure 4.15: Multi row test case: span-wise averaged adiabatic effectiveness on the wall ($BR = 2$, $DR = 1$)

η_{ad} value at the end of the plate, due to worst discretization of holes, translating in greater numerical diffusion. Delimited cylinder appears to be the better predictor of complete hole discretization results.

Looking at Figure 4.15, where adiabatic effectiveness profile comparison is reported, it is possible to see how $elm/D = 20$ delimited cylinder shape case profile is very well reproducing the complete hole case one, even in the first part of the plate, since the higher BR value leading to penetration regime.

It is important to stress that the object of this study is not to reproduce experimental results, but complete hole discretization ones: film cooling model tool must be able to simplify design process.

4.3 Final remarks

A comprehensive validation analysis of the performance of the proposed film cooling model has been performed. Investigated conditions embrace both the penetration and non-penetration regime with BR ranging between 0.5 to 2.0 and include single hole and multi-row flat plate film cooling. The present film cooling model shows itself as a feasible and reliable tool: the scope of this methodology is in fact to reproduce in the most coherent and representative way the predictions of complete hole CFD analysis, avoiding the time-consuming mesh process and with a smaller (in terms of element number) numerical domain. The comparison is achieved trough analysis of adiabatic effectiveness profiles and distributions. Concerning the injection volume shape, the cylinder shape overestimates the effective portion of the domain occupied by the cooling jet, leading to greater values of adiabatic effectiveness in respect to *full computation* analysis, using isotropic turbulence model. Hence, delimited cylinder shape is more reliable at medium and high BR values. Furthermore, when refining the mesh near the hole exit, the local source term approach converges towards the full meshing solution.

Regarding the study of single row flat plate, the limit of the uniform source application emerges leading to the necessity of spatial distribution

of source terms at low BR and when studying holes with low l/D ratio. However, such an improvement would be at the expense of the simplicity of the present model, since it would require knowledge of the distribution of the source terms for various blowing ratios.

Chapter 5

FCM application to a laboratory case: film-cooled turbine vane

This chapter is composed by two parts. The first part is dedicated to the description of an in-house developed decoupled procedure (*BANKS-3D*) aimed to predict cooling performances and metal temperatures of gas turbine blades and nozzles. In the second part, *FCM* and *BANKS-3D* are applied to a laboratory test case: NASA C3X-1988 film-cooled turbine vane.

5.1 Blade And Nozzle Network Solver (*BANKS-3D*)

An iterative procedure developed to solve a conjugate heat transfer problem in a decoupled way, recently presented by Andreini et al. [87, 88] is here described. In this procedure, the internal cooling system is modelled by an in-house one-dimensional thermo-fluid network solver, external heat loads and pressure distributions are evaluated through 3D CFD and heat conduction through the solid is computed through a 3D FEM solution. The proposed methodology is placed in the middle between fully 3D CFD tools, that require a complete meshing of the cooling system, and classical fluid network-based tools coupled with simplified conductive models. It allows, in fact, to contain computational costs, mainly related to CFD

discretization of cooling features, obtaining nevertheless results with an adequate overall accuracy. This characteristic is the main innovative nature of the new procedure, assuring its feasibility in both preliminary and detailed design phases.

The present procedure is able to supply a fully 3D characterization of the temperature field since it is obtained from the study of the three-dimensional thermal gradient. Compared to CFD CHT calculations, this decoupled procedure can execute temperature distribution estimation with a reduced computational cost, since utilizing a one dimensional correlative approach to evaluate thermal load and pressure on the coolant side, requires less computational resources than a CFD calculation applied to the entire domain. One-dimensional study of internal fluid network has the great advantage to easily permit sensitivity analysis, due to relatively short calculation time, besides being a robust design instrument, especially for preliminary considerations or optimization methods. Also the assessment of the film cooling effect (as it is described more in detail above) is not performed through the discretization of the solid domain as CFD CHT methods do. The use of correlations for the adiabatic effectiveness estimation and the application of the *Heat Sink Model* for the estimation of the heat removal through holes, makes faster and less expensive, from a computational point of view, to execute the analysis, since the decoupled procedure sets free from the bound of meshing. Solid is not simulated with cooling channels neither with ejection of fluid from them, and the geometry, which the FEM solver analyses, is not perforated. This allows to reduce the calculation time and the dependence of the solution from the mesh clustering, bound in particular to the coarseness of the mesh around the film holes. For their small dimensions, holes are difficult to discretize and therefore require a very high number of small elements, with the consequence of increasing considerably the computational cost. On the contrary the FEM grid produced by the procedure, for the same level of accuracy, is much more slight since the solution dependence on mesh coarseness is much less marked for the FEM analysis (see section 5.1.4).

5.1.1 Procedure description

A simplified scheme of the method discussed in this work is shown in Figure 5.1. It summarizes the flow chart of the iterative scheme and the main codes and tools involved in the procedure.

As it is evident from the diagram, the characterization of the three-dimensional temperature distribution of the blade, is obtained by interfacing the internal and external fluid solver with a 3D FEM thermal

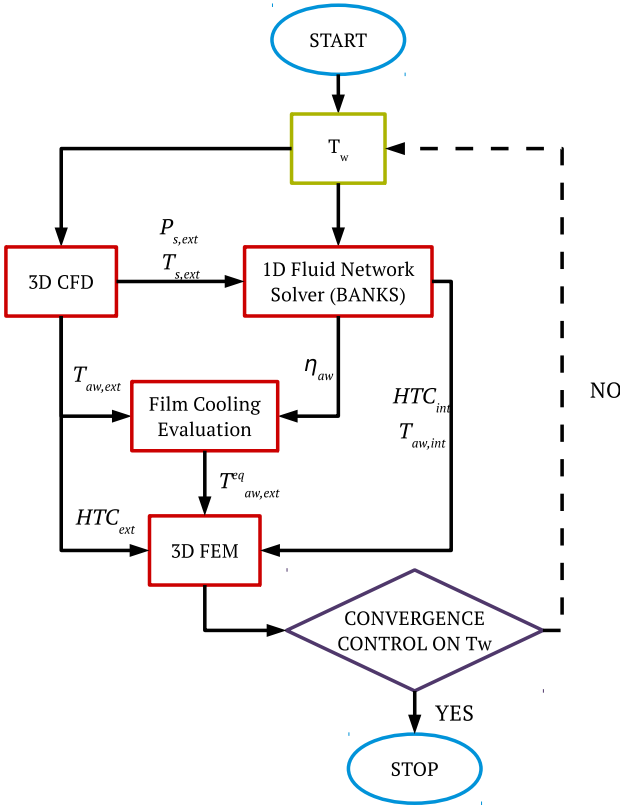

Figure 5.1: BANKS-3D: flow chart of the iterative scheme

conduction model. Each component solves a specific part of the heat transfer analysis.

To determine the blade temperature, it is necessary to evaluate:

- the external heat exchange, studied through a fully 3D CFD analysis;
- the internal heat exchange, studied by the 1-D fluid network solver *BANKS*;
- the conductivity through the blade studied, through a 3D FEM analysis.

Using these three codes, the blade temperature can be determined. FEM needs of boundary conditions which are required both on hot gas and coolant side. These boundary conditions are heat transfer coefficients and adiabatic wall temperatures. However the external aerothermodynamics, the heat conduction in cooled airfoil and the heat removed by the internal coolant fluid network, are strongly coupled: if on one hand blade temperatures depend on the fluid dynamic behaviour of hot gases and coolant, on the other hand, fluid dynamics depends on blade temperatures too, thus an iterative scheme to match external heat loads, metal conduction and internal cooling effects is necessary. It has to be verified that a heat balance is realized such that the the temperature everywhere in the model does not change between the last two temperature patterns by more than a value set by designer.

The calculation (Figure 5.1) starts with a first trial blade temperature distribution, which is utilized to initialize the codes used for the convection calculations (internal and external side). Internal heat transfer coefficient HTC_{int} and adiabatic wall temperature $T_{aw,int}$ are determined with *BANKS* and applied to the internal boundary elements. To estimate the aero-thermodynamics on the external blade surface exposed to the flow path, a CFD analysis is performed. It supplies to *BANKS* local external conditions required as input by the correlations such as gas velocity, V_g, temperature, $T_{s,ext}$, and pressure, $P_{s,ext}$. These information are used to obtain the right pressure drop through the film cooling

holes, which determine the mass flow rate through the film ducts, and there fore the coolant behaviour and efficiency. To *BANKS* also the adiabatic wall temperature, $T_{aw,ext}$, is provided by CFD calculations for the eventually correction of $T_{aw,ext}$ if film cooling is present. Finally, CFD provides heat transfer coefficient, HTC_{ext}, to the FEM solver, which is added to HTC_{int} and $T_{aw,int}$ coming from *BANKS* analysis. With these boundary conditions, the FEM solver calculates the temperature distribution through the blade, resulting in a new blade temperature pattern. In the next iteration, the new blade temperature distribution is applied as a new boundary condition again to the CFD code and to the fluid network solver, which perform again the fluid dynamic analyses allowing the cycle to be restarted until it converges.

In the following sections the various tools are analysed more in detail.

5.1.2 CFD analysis

In the CHT3D procedure, dedicated 3D CFD computations, are performed to determine the thermal loads and the pressure distribution which are necessary to characterize the external flow field. Such CFD simulations do not take into account the presence of film cooling holes on the blade, since the effect of the coolant film is computed by the 1D fluid network solver which through specific correlations provides to modified $T_{aw,ext}$ supplying the correct value, and simulating the decay of film cooling effectiveness along the airfol, as it will explain more in detail in section 5.1.3.1. Only the cooling due to purge flows coming from endwalls and cavities are completely simulated by the CFD tool, since they can not be modelled through *BANKS*.

However the role played by CFD analysis inside the decoupled procedure is limited to provide the external gas conditions, and HTC and adiabatic wall temperature, to express external loads on the blade surface. In order to obtain these information, which will be passed to the FEM solver for conduction solution and to *BANKS* as input to obtain the right β for each film cooling hole, two typologies of CFD calculation are required:

- an adiabatic simulation to provide $T_{aw,ext}$, $P_{s,ext}$ and the other parameters characterizing the main flow;
- a fixed wall temperature simulation for each overall iteration to provide HTC_{ext} values.

In the adiabatic simulation heat flux is zero everywhere on the airfoil. This allow to determine the temperature acquired by the external surface on which the thermal insulation is imposed. This distribution is then used in the fixed wall temperature simulation for each overall iteration which is performed until convergence occurs.

At the first iteration in which no approximation of T_w is known yet, the first trial blade temperature distribution is obtained scaling the $T_{aw,ext}$ distribution with a constant and consistent value chosen by the user to initialize the calculation.

Applying such a kind of initializing distribution, is more efficient than the imposition of a constant temperature equal everywhere on the blade, since although the right distribution is not obviously guesses, however a whatever distribution is set and this is more representative of what happens on the different parts of the blade, than the imposition of a constant value on every region of the airfoil, a condition which would be evidently not realistic. This causes a faster convergence to the solution since every time the computation starts from a solution closer to the correct one.

At each subsequent iteration of the overall procedure the fixed wall temperature simulation is re-performed, imposing the most updated wall metal temperature distribution.

In order to keep the definition of HTC always consistent, despite the local values of adiabatic wall temperature, which is eventually affected by the mixing with purge flows if they are present, the expression used for the definition of HTC is therefore:

$$HTC_{ext} = \frac{\dot{q}}{(T_{aw} - T_w)} \tag{5.1}$$

where $\dot{q}$ is the wall heat flux (obtained from the fixed wall temperature

simulation), T_{aw} (the adiabatic wall temperature obtained from the adiabatic simulation) is the reference temperature value and T_w is the wall temperature. Such definition of HTC_{ext} is chosen with the purpose of avoiding an equation denominator value equal to 0.

5.1.3 1D Fluid Network Solver (*BANKS*)

In the presented procedure, the internal cooling system is modelled using an in-house developed 1D fluid network solver, BANKS, which allows a modular approach of the internal cooling systems and solves the fluid network through a one-dimensional steady state analysis using a large cooling model library. In BANKS several elementary models of the main important and common cooling techniques and patterns (smoothed and ribbed radial tubes, curves impingement, film cooling, mixed axial and radial models and so on) are implemented. It can explore the common geometries used in innovative blade system and simulate the main external and internal cooling techniques (convection with and without turbolators, impingement, film cooling). It has been devised to be a quick tool for design problems involved in cooling systems for gas turbines, and its characteristics are studied to reduce as much as possible run time, keeping in the meantime results accuracy and permitting designer to easily perform sensitivity analysis. With the various implemented components patterns, combined in a fluid network, the user is able to describe the most complex blade cooling solutions.

After assigning the inlet boundary conditions, defined in terms of total pressure and total temperature, and the outlet boundary conditions in terms of static pressure profile, BANKS provides for each single model the thermo-fluid dynamic output parameters. User can also specify boundary conditions for fluid network in terms of inlet and outlet pressures or mass flow rate, depending on design specifications. Component flow function is generally wall temperature-dependent and not linear, thus flow function for each component is linearized and network is numerically solved, with an iterative procedure, returning coolant output conditions (pressures, mass flow rate distribution and so on) and the distributions of the heat transfer

coefficient and adiabatic wall temperature (Table. 5.1). Convergence is achieved when differences on pressures and mass flow remain unchanged or below the allowed error limit set by user.

Coolant is considered to be a perfect gas subjected to wall friction, heat transfer, area change, centrifugal effects and mass addiction (or removal). Flow field is solved in subsonic regime, Mach number up to unity, as is usually the case of actual cooling systems.

Commonly used best-practice correlations, collected in literature during years, for various cooling systems, are used to determine the coolant heat transfer coefficients and total pressure losses, while the one-dimensional momentum and enthalpy equations are solved for the coolant temperatures. The heat transfer coefficients and coolant temperatures are assumed to vary in the coolant flow direction.

Geometric specifications of single components, as holes diameters, channel heights, ribs angles and so on, together with results coming from the previous CFD simulations (Section 5.1.2) represent the input data for *BANKS*. In particular the 1-D network solver uses at each iteration, HTC_{ext}, $T_{aw,ext}$ and $p_{s,ext}$ from CFD , while the conditions on the internal surface, in terms of HTC_{int}, $T_{aw,int}$ and $p_{s,int}$, used to initialize the calculation and accelerate the convergence, are those carried out from the previous iteration. As already mentioned, if the first iteration is performed, as regards $T_{aw,int}$, this is derived from the first trial blade temperature distribution got from the CFD analysis.

BANKS discretizes the blade through sections orthogonal to the blade axis and therefore and refers to a dimensional curvilinear abscissa

Table 5.1: Main inputs and outputs in BANKS

Inputs	**Outputs**
Geometry	Internal HTC
Coolant BC's conditions	Internal T_{aw}
Internal wall temperature	Coolant exit conditions
	η_{aw} estimation

obtained with a specific algorithm. Sections number depends on the geometry system complexity.

With specific macros files containing the x, y, z coordinates and corresponding non-dimensional abscissas of nodes on airfoil, and inner cavities, individuated from the intersection between the mesh and the 2D planes, are created. These files will be used within the single iteration every time there is a passage of informations between *BANKS* and ANSYS® Workbench v.14 environment used, the latter, to place the thermal load on the blade surfaces and to solve the conduction.

Similarly macros are used to generate from CFD results, gas parameters distributions referred to the blade airfoil sections expressed in term of dimensional curvilinear abscissa, since gas properties (T, P, V, Cp, R, μ , λ) obtained by CFD, are initially expressed in function of Cartesian coordinates, being referred to the mesh nodes of the 3D CFD analysis.

When BANKS has obtained of the all required informations, it analyses the cooling system at each section with its correspond thermal loads. The coolant heat transfer coefficient HTC_{int} and the bulk coolant temperature T_c are allowed to vary radially and along the adimensional abscissa (case of film cooling). In the case of radial channels, it provides the temperature distribution along the cooling ducts and cavities through the interpolation along the radial axis, of the temperatures calculated with the one-dimensional approach for each control volume, in which the channel is discretized. The number of control volumes is set by the user according to the complexity of the cooling scheme. Similarly $HTCs$ values are calculated from correlations for every control volume, and are interpolated along the radial direction. Also the coolant conditions in term of Ma, Re and so on are calculated giving a one-dimensional distributions along the ducts. Based on this one-dimensional method, likewise the other models of cooling techniques are solved, including film cooling.

Then the output provided by BANKS, containing fluid network solution, are passed to the FEM solver as internal boundary conditions for the following conduction analysis.

5.1.3.1 Film cooling and holes heat sink effect

One of the most interesting aspect of the procedure is the modelling of film cooling through the use of a correlative approach which does not require a discretization of the solid domain.

The film cooling effect is evaluated from the fluid network solver by computing, along prearranged radial sections of the blade, the adiabatic effectiveness using implemented correlations (Appendix A.1). Local external conditions required as input by the correlations (pressure, gas velocity and temperature), are obtained from the adiabatic CFD simulation. The resulting distribution of adiabatic film effectiveness is then interpolated on the 3D surface of the airfoil and local values of adiabatic wall temperature (T_{aw}), predicted by the CFD simulation, are corrected according to the definition of adiabatic effectiveness:

$$T^{eq}_{aw,ext} = T_{aw} - \eta_{aw}(T_{aw} - T_c) \tag{5.2}$$

where η_{aw} is the local value of adiabatic effectiveness after the interpolation from the correlation data and T_c the coolant temperature exiting from each hole (computed by the fluid network solver).

The heat removal due to convection through the film cooling holes has been taken into account considering the convection correlations (see Appendix Heat transfer coefficient estimation correlations). This approach allows to avoid film cooling holes meshing, strongly reducing the computational costs.

5.1.3.2 Adiabatic effectiveness estimation

Concerning the adiabatic effectiveness estimation, various correlations collected in literature are implemented in the fluid network solver to evaluate the adiabatic effectiveness according to the different typology of device adopted. In Appendix Adiabatic effectiveness estimation correlations, details and range of validity of these correlations are reported.

5.1.4 FEM 3D Thermal conduction model

Finally, once external and internal thermal loads are evaluated, conduction through the metal of the blade can be solved. The procedure uses the FEM module of ANSYS® v.14. External load values (HTC_{ext} and $T^{eq}_{aw,ext}$), obtained by CFD and film cooling steps, are interpolated on external blade surfaces of FEM mesh (airfoil, endwalls). In the same way internal loads coming from the fluid network solver, in terms of HTC and T_{aw}, are interpolated on the internal cavities of the blade. The entire set of interpolation steps is completely managed by automated tools coupled with the ANSYS® Workbench environment. FEM grid is clustered enough to limit discretization errors due to interpolation process on non-conformal grids.

5.1.5 Convergence criteria

As outlined in the description of the various steps of the procedure, the convergence is verified by checking the local values of the wall metal temperature. The procedure is considered converged when the relative error between the last two iterations is below 0.1%. Very few iterations (below 10) are usually required to obtain convergence.

5.2 Film-cooled turbine vane test case

The last of tested campaigns for validating the presented procedure will be now described. After validation of the presented film cooling model on single hole and flat plate, now it is tested on a representing real cooling scheme of a vane. The present cooling configuration is the one applied to 1988 NASA C3X test case, herein referred to as *1988 C3X*, originally presented by Hylton et al. [89]. The test case is representative of a highly loaded, low solidity, internally and externally cooled airfoil, simulated at engine conditions with an internal cooling device, composed of ten radial smooth channels, to which a open loop cooling system is added in the form of film cooling and showerhead. The vane presents a thermal barrier

separating the leading edge and the tail region. The last one is the only taken into account in heat transfer and temperature measurement.

After a brief overview of results available in literature about 1988 C3X test case, blade geometry and Hylton's experimental activity are introduced. Afterwards, the results obtained in the present work are presented. The results will be compared with experimental data provided by Hylton et al. [89], *BANKS-3D* results and a fully 3D CHT analysis.

5.2.1 Literature review

Similarly to 1983 C3X test case, many authors referred to the Hylton et al. [89] report for their verification purposes, since it provides a database covering a wide range of operating conditions and geometries, allowing to investigate a more complex configuration, comprehensive of film cooling. Measurements from this experiment provide data for downstream film cooled turbine vanes and extend the database generated in the previous studies [90, 91]. Therefore, because of the possibility to test tools prediction capabilities in presence of both internal and film cooling, 1988 C3X vane has been the subject of several investigations too.

Garg and Gaugler [92] conducted RANS simulations of the film and internally cooled C3X vane by prescribing the experimental temperature distribution along the blade surface and velocity/temperature profiles at the hole exits. They noticed that the exit velocity and temperature profiles could result in differences up to 60% in HTC when comparing to experimental data. Also, different effects were observed on the pressure and suction surface upon the hole shape, conical or cylindrical. The study highlighted the importance of specification of proper conditions at the hole exit in film-cooling applications. In [93], authors varied the span-wise pitch of shower-head holes (maintaining the other details of the vane geometry fixed) from the original $7.5\,D$ to $3.0\,D$, in order to study its effect on the heat transfer coefficient and effectiveness over the vane surface finding highly three-dimensional behaviour for adiabatic effectiveness and heat transfer coefficient.

Laskowski et al. [94] performed a turbulence model assessment and mesh sensitivity using ANSYS® CFX with unstructured meshes. Good metal temperature agreement was found with experimental data, showing that the wall integration approach allows a better agreement than wall function. The wall integration metal temperature falls within the experimental uncertainty aside from a small region downstream of the thermal barrier on the pressure side. In [95], the same authors conducted 3D simulations of the plena, film and hot gas path with prescribed wall temperatures, and compared heat transfer coefficients to the experimentally derived. In general the agreement was satisfactory.

Mangani et al. [96] analysed the same geometry and experimental test point tested by Laskowski et al. [94] for validating a procedure aimed to transform OpenFOAM ® code in a complete CFD suite for the steady and unsteady analyses of heat transfer. A certain number of turbulence models have been tested, finding good agreement with experimental measurements in terms of wall temperature for the Spalart-Allmaras V2F and TL SST turbulence models, while the one equation SA turbulence model showed disagreements with respect to experiments. For wall heat transfer coefficient predictions all the turbulence models gave an acceptable agreement with experimental data in terms of HTC profile shape except for the TL model that has a lack in the prediction near the thermal barrier for both airfoil surfaces.

Hall et al. [97] conducted 2D simulations of the internal/film cooled 1988 C3X vane leading edge film cooling data of Hylton et al. [89]. The simulations included the film cooling holes and plena and made use of span-wise periodic boundary conditions to minimize the problem size. The experimental temperature was prescribed along the vane surface and comparisons were made between the derived heat transfer coefficient and the computed value. The computed value was 50% - 150% higher than the experimental value near the leading edge, with the agreement improving only between 50% - 100% of the surface distance from the leading-edge and further towards the trailing edge.

Sarkar et al. [98] used experimental data from 1988-C3X vane to validate a Navier-Stokes flow solver in the finite volume form using the Baldwin-Lomax algebraic model. The main thrust of the paper was to examine the effects of variable wall temperature, which occurred as a result of internal convective cooling, on prediction of blade surface heat transfer. Results obtained showed good agreement with the experimental data. Sarkar et al. [99] also conducted 2D simulation on the same geometry with suction side and pressure side film cooling for different pressures and temperature ratios. The experimentally derived heat transfer coefficient was prescribed along the vane external surface in order to compute a metal temperature.

5.2.2 Test case description

In this section, the experimental program, concerning the procedure employed by [89] to obtain the experimental results, and the description of the test case, are briefly presented.

5.2.2.1 Geometry and film cooling scheme

The vane profile used for 1988 C3X is the same as the one used in the non-film cooled experiments reported in [90].

The test vane located in the centre was replaced with a new C3X vane which had suction side, leading edge, and pressure side film cooling arrays. The test vane was initially fabricated as a single piece. After all the film cooling holes and plena and the ten radial cooling holes were machined, the vane was cut into a nose and a tail piece to form a thermal barrier between the film cooled nose piece and the rest of the vane (Figure 5.2). The two pieces of the vane were held together by two pinned tabs mounted on each end of the vane.

The test vane was internally cooled by an array of ten radial cooling holes. The radial cooling holes of each of the outer two slave vanes were supplied from a common plenum, whereas each hole in the test vane was supplied from a separate, metered line.

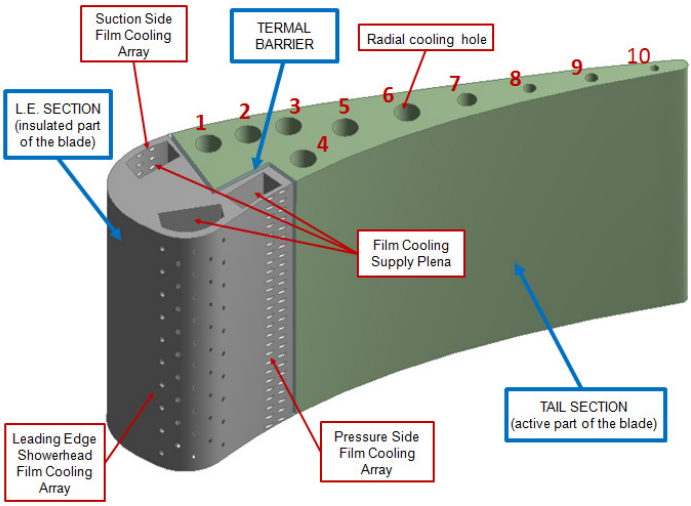

Figure 5.2: Cooling scheme of 1988 NASA C3X

Concerning the film cooling geometry, in addition to the details available in Figure 5.2, one row of showerhead holes was located at the geometric leading edge, with one row on the suction side and three on the pressure side. Previous film cooling data [91] indicated that the ideal locations for the suction and pressure surface film cooling arrays would be just upstream of the suction and pressure surface recovery region respectively. These locations were determined to be 25.2% of the surface distance (as measured from the geometric stagnation point) on the suction side and 22.5% of the surface distance on the pressure side. Two cooling hole rows were centred at these points. The length to diameter ratio of the holes were kept the same as the showerhead hole length to diameter ratio.

The three film cooling arrays were fed by three supply plena, each with a separate, metered line. This system was designed to provide the capability of individually controlling the blowing parameters of each array. The film coolant supply was piped through an electric heating system

that provided the capability to vary the coolant supply temperature.

5.2.3 Experimental test overview

In the experiment conducted by [89], in order to obtain heat transfer measurements, the internal and external boundary conditions of the test piece were evaluated at thermal equilibrium and then, the internal temperature field was estimate by solving the 2-D steady-state heat conduction equation within metal.

5.2.3.1 Instrumentation

The external boundary conditions were measured using thermocouples installed in grooves on the exterior surface of the test vane. Each airfoil surface was instrumented with approximately eighty thermocouples located in the fully 2-D region of the airfoil in a plane near midspan. Additional surface thermocouples were located off midspan on each test vane to check the 2-D assumption. Each test vane was instrumented with surface static pressure taps in addition to the heat transfer instrumentation. Approximately 30 taps were located around each airfoil outer surface in a plane near midspan.

The flow to each cooling tube and plena of the test vane was measured using a calibrated orifice meter. Each cooling tube was also instrumented with a static pressure tap and thermocouple at the vane inlet and exit in order to measure static pressure and total temperatures at the inlet and exit of the vane for each duct.

5.2.3.2 Data reduction

Cascade inlet total pressure and temperature were based on readings at the upstream core flow rakes. The average inlet/exit static pressure value were taken as the average of readings of a certain number of endwall static taps at the cascade inlet/exit plane.

The average wall temperature was defined as the average of the midspan vane surface temperatures. The operating conditions of Re

(based on the true chord) and T_w/T_g were calculated from these averaged measured quantities. The average coolant temperature for each tube at the vane surface temperature measurement plane was calculated, assuming a linear temperature rise through the vane cooling hole.

The Re for each cooling tube was determined from the measured flow rate, cooling hole diameter, and viscosity based on the average coolant temperature. The Prandtl number for the coolant flow was calculated from the average coolant temperature. Average heat transfer coefficients and coolant temperatures for the ten radial cooling holes, provided the internal boundary conditions for the finite element calculation. The Nusselt number was then calculated from the following relationship for turbulent flow in a smooth pipe:

$$Nu = Cr(0.022Pr^{0.5}Re_D^{0.8}) \tag{5.3}$$

Cr is a function of Pr, Re_D, and x/D, which corrects the Nu expression for a fully developed thermal boundary layer to account for thermal entrance region effects. The constant Cr found in [100] ranged from approximately 1.03 to 1.12 for the Pr, Re_D, and x/D values encountered in the experiment. The average heat transfer coefficient for each cooling hole was then calculated from the Nusselt number, hole diameter, and thermal conductivity.

5.2.3.3 Tabulated experimental data

Measured results provided by Hylton et al. [90] are pressure and temperature distributions, whereas heat transfer coefficient is a derivative quantity. All distribution are located at midspan of the blade and values have been normalized to reference ones.

5.2.4 Numerical setup

5.2.4.1 BANKS setup

Procedure-supporting CFD simulations Steady-state CFD RANS calculations have been performed with the commercial 3D Navier-Stokes

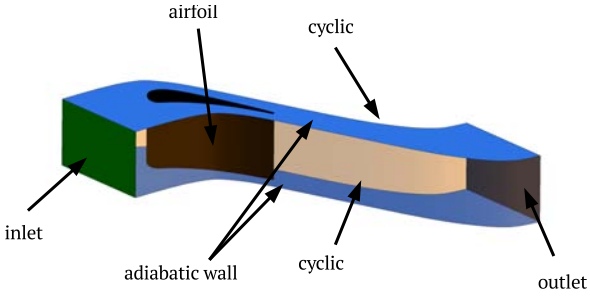

Figure 5.3: Film-cooled vane test case: CFD domain of procedure-supporting simulations

solver ANSYS® CFX v.14. In Figure 5.3, the numerical domain is reported. Solid surfaces are treated as smooth, no-slip walls, upper and lower walls are considered adiabatic. Only one vane is simulated, delimiting external fluid domain by periodic boundaries. The flow path boundary conditions have been recovered from Hylton et al. [89], in terms of total pressure, total temperature, turbulence intensity and length scale values at the inlet, but the outlet static pressure was not specify. Furthermore, no transitional turbulence model has been applied due to the presence of film cooling holes on the airfoil modifying the external flowpath.

Hylton et al. [89] reported an average Mach number at a pressure rake, located just aft of the vane trailing edge plane at the midspan, and that Mach number has been converted to an average static pressure, using the isentropic flow relation:

$$\frac{p_{0g}}{p_g} = \left(1 + \frac{\gamma - 1}{2} Ma_{is}^2\right)^{\frac{\gamma}{\gamma-1}} \tag{5.4}$$

The average static pressure value has been adjusted in the simulations, taking into account pressure losses, by matching the value of the provided Mach number, at the outlet of the computational domain.

Compressibility effects have been taken into account and the High

Resolution advection scheme has been used. The fluid has been modelled as ideal gas with molecular weight 28.96 $kg\ kmol^{-1}$ and the properties of specific heat capacity c_p, thermal conductivity λ and viscosity ν, were expressed as function of temperature by correlations fitting the data reported by Rohsenow et al. [101].

Energy equation has been solved in terms of total energy and viscous heating effects have been accounted for. The $k-\omega$ SST turbulence model, in its formulation made available by the CFD solver, has been used in conjunction with an automatic near-wall treatment approach.

Fluid network setup In the fluid network solver, film cooling and showerhead devices are modelled through a pattern which treats at the same time the flux through the radially cavity (of generic shape), and the ejection of coolant through the rows of film cooling and showerhead, connected to the cavity. All geometrical data required by the fluid network solver for defining the model, have been retrieved from Hylton et al. [89].

Concerning the internal cooling system, the ten radial channels were fed by a metered line with a calibrated orifice meter for each tube, in order to control inlet pressure and temperature separately for each duct. The one-dimensional fluid dynamics is resolved using correlations from a traditional set (see Appendix Heat transfer coefficient estimation correlations), for fully developed flows.

Geometry and internal flow conditions, at the tasted operating points, always allow to obtain Reynolds numbers clearly above 10^4, and so, to achieve fully turbulent conditions. As regards the inlet region, flow was assumed to be fully developed at the hole inlets at the hub of the vane, as in the experiment of [89], there were long tubes feeding the channels [102]: flow developed in piping leading coolant through the metered line to the test-bed blade, before entering the tubes. On the base of these considerations, flow inside the channels has been treated as a fully developed one, without considering the entry region, assuming its development occurred in the metered line before reaching the vane.

The model implemented for the resolution of the flow through the

internal radial ducts, carries out a 1D calculation of the stationary flow, considering friction effects and heat transfer; the duct is modelled as a radial channel having a generic section eventually variable with the radius (with a roughness/smoothness which is imposed by user). For 1983 C3X test case, a smooth surface and a cylindrical section have been imposed. All geometric parameters required to correctly characterize the model, have been retrieved from [89], such as diameters, height of the blade and so on. Each tube needs to be characterized by an own specific value for both inlet total temperature and pressure. These are the inputs required, as usual, by the fluid network solver, together with the discharge static pressure.

However, whereas 1983 C3X vane case provided documentation of the radial coolant channel flow [90], 1988 C3X vane case did not. Coolant supply conditions were not documented in the original report [89], and literature too is poor about these informations. The study carried out by Laskowski et al. [103] had resulted as the most exhaustive among those consulted concerning information about boundary conditions. In their work the authors present an inverse procedure for finding the mass flow rate and the total inlet temperature for each channel. From geometry, external wall heat transfer coefficient and metal temperature distributions retrieved in [90], cooling flows has been calculated in order to match the experimental metal temperature distribution at midspan. However they provided boundary conditions only for case run 44344 (Table 5.2) and for this reason it has been chosen for the present analysis.

Informations about plena feeding film cooling rows, have been retrieved in [89]. Table 5.3 shows the actual secondary flow conditions represented by the coolant to gas absolute temperature ratio, T_{0c}/T_{0g}, the average coolant to free stream total pressure ratio, P_{0c}/P_{0g}, and film coolant mass flow rate for each of the three plena supplying the suction surface, the leading edge, and the pressure surface film cooling arrays. The coolant to gas absolute temperature ratio has some variation from plenum to plenum due to each cavity requiring a different coolant mass flow rate to achieve the prescribed coolant to gas total pressure ratio. Each plenum

Table 5.2: Film-cooled vane test case: radial cooling channels boundary conditions (Source [103])

	Final values	
Channel	$\dot{m}[kg\ s^{-1}]$	$T_{0c,in}[K]$
1	0.00784	425.25
2	0.00793	367.06
3	0.00794	350.79
4	0.00826	402.94
5	0.00748	325.1
6	0.00691	326.76
7	0.00752	360.59
8	0.00770	422.46
9	0.00473	379.99
10	0.00357	421.32

Table 5.3: Film-cooled vane test case: boundary conditions for coolant feeding plena

	$P_{0c}/P_{0g}[-]$	$T_{0c}/T_{0g}[-]$	$\dot{m}[kg\ s^{-1}]$
Suction Side	0.85	0.0134	0.0296
Leading Edge	0.86	0.00638	0.0141
Pressure Side	0.83	0.00752	0.0166

is fed separately and all inputs required by the fluid network solver are available. The discharge pressure will be imposed by the external flow field determined by the procedure-supporting CFD simulations, since no tip discharge is provided.

In order to evaluate the heat transfer coefficients on radial cavities and film tubes surfaces, it is possible to choose from the same set of correlations available for the radial channels.

FEM setup As for the previous case, the conduction through the metal of the blade is solved by the *Steady-State Thermal Module* of ANSYS® v.14. The boundary conditions are both the internal and external thermal

loads derived from the CFD and from the fluid network solver interpolated on the blade surfaces. The value of thermal conductivity was specified to vary linearly with the temperature as reported by Facchini et al. [104]:

$$k\left(T\right) = 6.811 + 0.020176 \cdot T \tag{5.5}$$

For this simulations, the numerical grid consists of about $9.8 \cdot 10^5$ tetrahedral elements (with ten nodes).

5.2.4.2 Full 3D CHT analysis

In Figure 5.4, the numerical domain employed in the fully 3D coupled conjugate analysis is depicted. Following the experimental test rig configuration, the solid blade has been discretized with three different solid domains: the blade LE (where the film cooling feeding plena are placed), the blade tail (where the internal cooling tubes are located) and the insulating thermal barrier between the two solids. The fluid domain comprehend both the hot gas path flow and the three film cooling plena: in this way no interface connections between fluid domains are needed.

Moreover, in order to track the coolant distribution, four transport

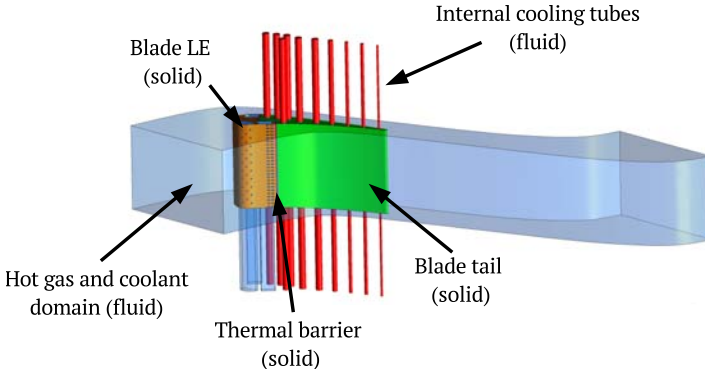

Figure 5.4: Film-cooled vane test case: full 3D CHT analysis numerical domain

equations for as much additional passive scalars representing coolant concentration were solved, settings their value accordingly to the particular plenum, holding the value 1 at the particular plenum inlet and 0 at the other inlets: one passive scalar for the coolant coming from each plenum and one passive scalar (*coolant*) representing the film cooling effect of all the coolant.

Blade LE and blade tail solids employ temperature dependent proprieties (following [104]). Concerning the thermal barrier solid, a low constant thermal conductivity value ($0.03\ W\ m^{-1}\ K^{-1}$) is applied.

It is important to note that following the guidelines provided in Section 2.5, where for the study of a single hole the use of mesh of about 1 million elements is advised, in this case the hot gas and coolant mesh would have count about 152 million elements (since 152 film cooling holes are realized), not counting solid and internal cooling tubes. This mesh would result not affordable from a computational point of view, so a lighter mesh process has been adopted leading to a more time-affordable numerical grid: this is a hybrid (tetra and prism layers at the solid walls) unstructured mesh (summary is reported in Table 5.4).

As for the the procedure-supporting CFD simulations, the flowpath boundary conditions are recovered from [89], as for the plena boundary conditions. As explained above, the coolant supply conditions for the ten channels were not documented in the original report [89] and they are recovered from [103].

Table 5.4: Film-cooled vane test case: mesh characteristics of the full CHT computation

domain	**mesh dimension**
hot gas and coolant	$25.3 \cdot 10^6$ elements
solid	$8.1 \cdot 10^6$ elements
internal cooling tubes	$6.0 \cdot 10^6$ elements

5.2.4.3 Film cooling model implementation

In this case, as applied also in [92], the computational span of the domain is 1/20 of the real span: the spanwise pitch domain is $7.5D$, where D is the diameter of the holes. In other words, the influence of the upper and lower endwalls has not been taken into account, limiting the study of film cooling just at the central part of the real span. This shrewdness is due to reduce the domain and so the computational time, reducing the number of film cooling holes actually studied. So, a symmetry condition on the lower and upper side has been applied, in order to obtain a less computing expensive numerical grid. Coming from the results of the other test cases, $elm/D = 5$ and $elm/D = 20$ hole discretizations are applied: as could be expected, it has been proved how $elm/D = 10$ discretization returns results standing between the other two, and so it has been decided to not continue to study this case.

Following previous considerations about injection volumes and BR (from the first part of the validation process, Section 4.3), only the delimited cylinder injection volume shape has been retrieved in this application: in Table 5.5, BR results retrieved from BANKS analysis have been reported. It is possible to observe how BR values are similar in case of PS and SS rows, while there are strong discrepancy in SH rows. In particular, the middle SH row presents a very high BR value: in correspondence of this row the fluid stagnation point is located, so external gas velocity is near to 0, leading to a high penetration of cooling jets.

The standard numerical setup has been applied. Details of the two exploited meshes are reported in Table 5.6.

Even in this case, in order to evaluate the coolant development and its effectiveness, a passive scalar has been injected into the domain in correspondence of the injection volumes.

Table 5.5: Film-cooled vane test case: mean BR values for film cooling holes

row	BR
SS2	0.82
SS1	0.82
SH1	1.77
SH2	3.35
SH3	13.9
SH4	2.56
SH5	2.18
PS2	1.72
PS1	1.66

Table 5.6: FCM: mesh dimension for film cooling model (film-cooled vane test case)

elm/D	**mesh dimension**
5	$0.84 \cdot 10^6$ elements
20	$1.85 \cdot 10^6$ elements

5.2.5 Discussion of results

First of all, in order to assess the accuracy of the *BANKS-3D* procedure, comparisons with experimental metal temperature values on the midspan of the blade (as reported in [89]) will be now discussed. Furthermore, comparisons between the three numerical approaches (correlative, full CHT and *FCM*) in terms of adiabatic effectiveness are reported. Also, about *BANKS* procedure, the influence of superposition model is highlighted. Temperature values are normalized with the very same reference values reported in [89]. Moreover, concerning T_w/T_{ref}, experimental error bars of $\pm 2\%$ (as reported in [89]) are applied.

Concerning correlative approach, in terms of *HTC* evaluation, two simulations were carried out: one employs Dittus Boelter correlation (*case*

1) and the other employs Gnielinski one (*case 2*). A comparison with the full 3D CHT run and experimental values [89] is reported in Figure 5.5 (metal temperature values on the leading edge region are not reported by Hylton et al. [89]): small differences between simulations with different convection correlations can be found. Comparison with experimental data shows a very good agreement except for small differences on the pressure side near -40% of the blade.

In Figure 5.6, η_{ad} averaged values are reported for suction and pressure side: they are averaged on the portion of the domain employed in *FCM* analysis, in order to avoid spurious effects of endwalls on the flowfield, in the fully CHT case. The spikes on the full 3D CHT and film cooling model application data are relative to the injection holes, where the coolant concentrations are equal to 1. Superposition models by L'Ecuyer and Soechting [21] and Baldauf et al. [25] are applied. Due to very similar η_{ad} values, only *case 1* data are reported.

In the region interested in film cooling coverage effect, strong 3D phenomena due to the interaction between jets coming out from the plena and the main flow are present. Besides, as reported above, SS and PS holes are placed just upstream the suction and pressure recovery region respectively, introducing another solid 3D effect. These phenomena could explain the difference in terms of metal temperature and adiabatic effectiveness between correlative and full 3D CHT results.

Looking at the LE region ($-0.22 \leq X/Ax_{Ch} \leq 0$ in Figure 5.6a and $0 \leq X/Ax_{Ch} \leq 0.25$ in Figure 5.6b), a good agreement between the three approaches can be seen, in terms of both values and trends. In this particular region, film cooling holes have a strong component of compound angle ($45°$): it is important to highlight that no correlation for adiabatic effectiveness evaluation available in open literature from the author knowledge, considers compound angle in their formulation. For this reason, correlative approach tends to underestimate CFD-based approaches results. *FCM* implementation does not show to be influenced by mesh refinement in this region, while slightly overestimating full 3D CHT approach results, especially on the suction side of the LE region. In

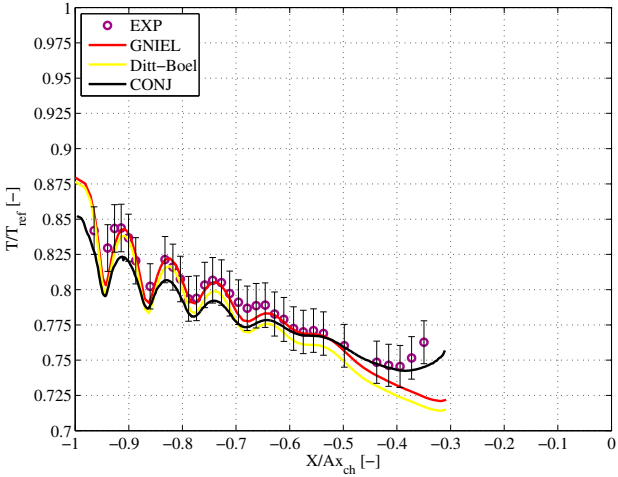

(a) Pressure side

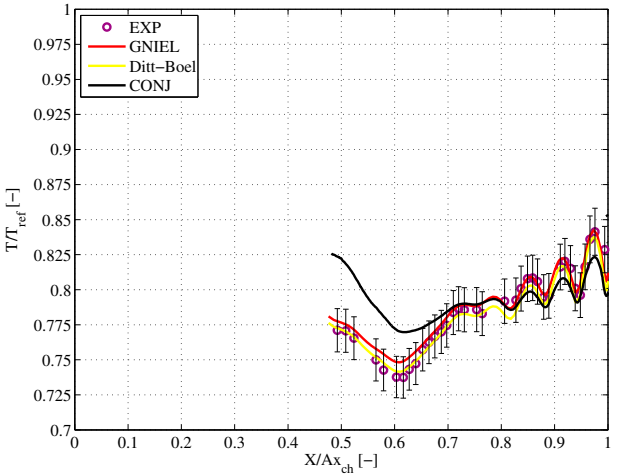

(b) Suction side

Figure 5.5: Film-cooled vane test case: span-wise averaged metal temperature profiles on airfoil

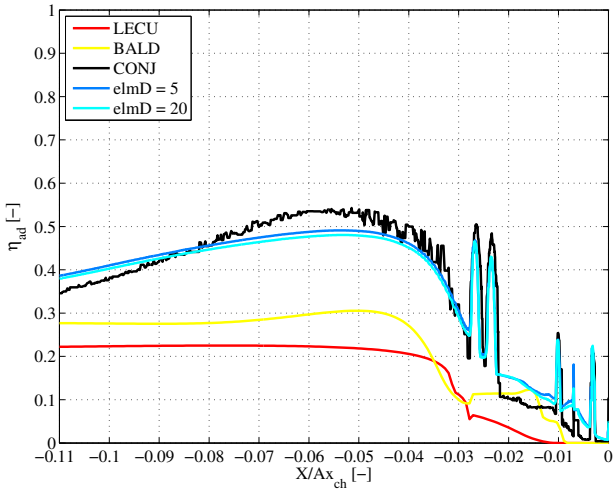

(a) Pressure side

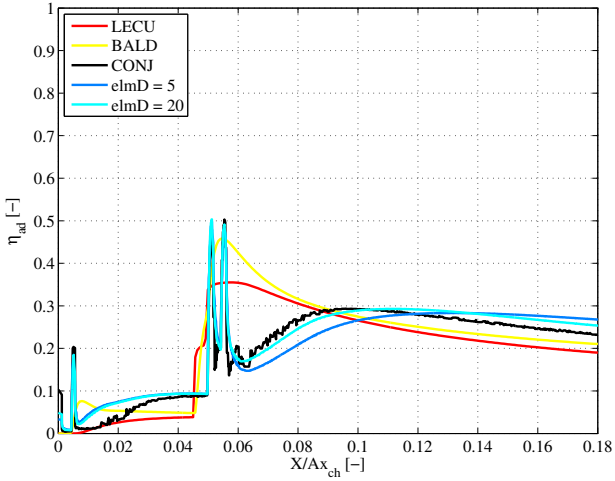

(b) Suction side

Figure 5.6: Film-cooled vane test case: span-wise averaged adiabatic effectiveness on airfoil

Figure 5.7, passive scalar distribution coming out the second showerhead row is presented. In this particular row (the one placed on the geometric LE of the airfoil), coolant has not enough momentum to develop along the span direction, being dragged away by the main flow along the blade: this is due to the high perforation angle (90°).

Moving toward the PS (Figure 5.6a), some differences between BANKS and the other CFD-based results arise. In Figure 5.8, the CFD coolant concentrations in a plane cutting the axes of near-midspan PS e SS holes is depicted. The adverse pressure gradient on the PS leads to a greater boundary layer, and a greater coolant protection predicted by CHT and *FCM* analysis, resulting in metal temperature differences in Figure 5.5 (only CHT case). The correlative-based approaches results to not be able to catch these strong 3D interactions. Going ahead towards the trailing edge, these effects softened leading to a very good agreement of the results.

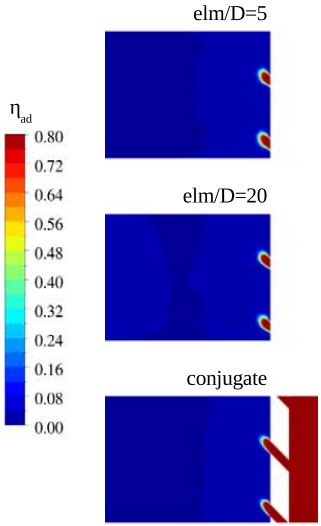

Figure 5.7: Film-cooled vane test case: coolant distribution on the second SH row

Furthermore, comparing the jet imprints related to film cooling model implementation to the full 3D CHT ones (Figure 5.6), it is possible to stress the film cooling model ability to reproduce the coolant injection

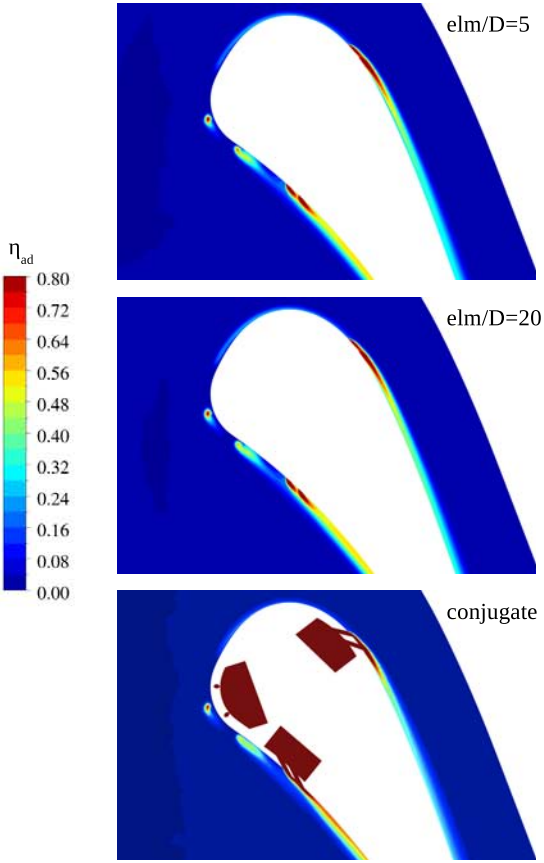

Figure 5.8: Film-cooled vane test case: coolant distribution on mid-plane of the domain

inside the main-flow and its development along the airfoil. In Figure 5.9a, the adiabatic effectiveness distribution on the portion of the vane studied in *FCM* implementation is reported: the FC model jet traces on the surface qualitatively well match the full 3D CHT results. From a quantitative point of view, looking at the span-wise averaged η_{aw} profiles in Figure 5.6a, film cooling model results show to well predict the same results of the fully CHT simulation.

Concerning the SS, looking at the η_{ad} profiles in Figure 5.6b, in the region right after the coolant injection, it is possible to observe a different behavior of the simulations: correlative approaches present greater values of η_{ad} than CFD-based predictions, leading to a better T_w/T_{ref} values agreement with experimental data (Figure 5.5). Conjugate CFD analysis predicts jets penetration regime as can be seen in Figure 5.8: this explains the differences in η_{ad} and so in metal temperatures with thermal procedure results. When jets reattach on the surface, for $X/Ax_{Ch} \geq 0.6$, the numerical agreement improves. In this case, mesh discretization injection volumes show different behaviours: the strong 3D jet development leads to different coolant distribution coming out the holes (Figure 5.8) and along the vane surface (Figure 5.9b), resulting in a different span-wise averaged η_{aw} profile in case of $elm/D = 5$ (Figure 5.6b). However, looking at $elm/D = 20$ profile, *FC* model well reproduces the full discretization results of full 3D CHT model.

5.3 Final remarks

In the last phase of validation activity, the prediction capability of the proposed film cooling model has been tested in a real film cooled vane: the studied test case is the well known internally and film cooled 1988 NASA C3X vane. In this case, the validation process has been expanded considering curvature effect, and a complete cooling system, comparing film cooling model predictions to both an in-house developed correlative approach and full CHT simulation.

Regarding the correlative approach, the applied procedure is the one

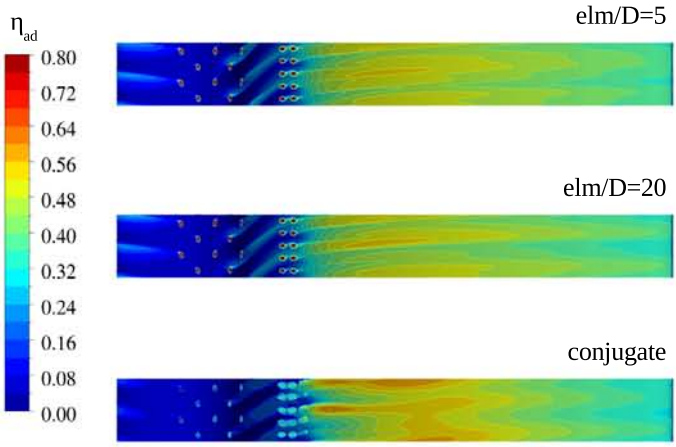

(a) Pressure Side

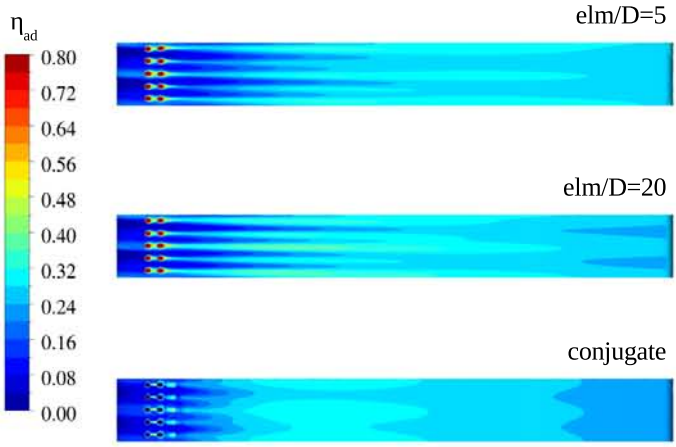

(b) Suction Side

Figure 5.9: Film-cooled vane test case: adiabatic effectiveness distribution on C3X airfoil: comparison between fully CHT and FCM results

described by Andreini et al. [87]: a segregated procedure aimed to predict cooling performances and metal temperatures of gas turbine blades and nozzles. Required inputs are evaluated by different tools: CFD, in-house fluid network solver and thermal FEM. In this particular application, attention has been focused on the film cooling adiabatic effectiveness evaluation through correlative approach. In particular, two correlations have been taken into account: the correlation proposed by L'Ecuyer and Soechting [21] and the one proposed by Baldauf et al. [25]. As regards the superposition effect, the model proposed by Seller [105] has been applied, modelling the effect of multi-rows ejections on the overall effectiveness distribution as a purely algebraic pattern.

Even in this case, results of film cooling model application with the most refined mesh, show a good agreement with the complete analysis study. Differences between CFD and correlative approach results can be ascribed to the inability of *BANKS-3D* to catch the strong 3D interactions in a complex flow as the one studied. Also, it is important to highlight that no correlation for adiabatic effectiveness evaluation available in open literature from the author knowledge, considers compound angle: this final consideration can explain the mismatch between results in the LE edge region.

Chapter 6

FCM application to a real case: nozzle of an actual engine

In order to test properly the developed methodologies, an actual test case will be presented. The investigated geometry represents a nozzle of a GE Oil & Gas heavy-duty gas turbine. For confidentiality agreement, all the details about geometry and boundary conditions are not reported.

6.1 Cooling scheme

The active central vane is composed by two cooled airfoils with inner and outer platforms: two foil cavities, one at the trailing edge and one at the leading edge are fed respectively from the hub and the tip by two different plenum chamber that surround the platforms (Figure 6.1). In each cavity an impingement system is used to provide the necessary internal cooling; the exhausted air is then discharged through a large number of film cooling holes, used to generate film protection on the whole foils surfaces.

The external cooling system is composed by a shower head, a set of film cooling holes on both the pressure side and the first part of suction side and several slots to protect the trailing edge. Summarizing, the surface of the foils are protected with the following film holes arrangement:

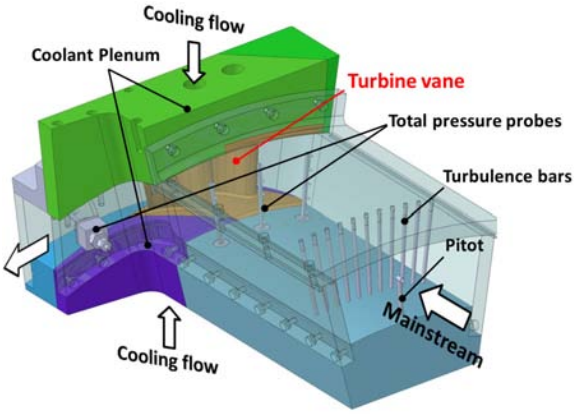

Figure 6.1: Real nozzle case: sketch of the test rig (Source [106])

- the leading edge is protected by 5 rows of 26 holes fed through the internal leading edge cavity (Shower Head). In the first half of the vane span the orientation of the holes is towards the outer platform while it is towards the inner on the second half close to the hub;

- several cylindrical film cooling holes are located on the PS up to the trailing edge region (total 103 holes arranged in 4 rows);

- the suction side is equipped with two rows of total 56 holes located near the leading edge downstream the shower head system;

- 17 slots with elongated pedestals are equally distributed in the TE foil cutback.

Concerning the platforms, 85 and 64 film cooling holes are present respectively on the outer and on the inner side, both distributed in rows starting from upstream the leading edge towards the vane throat. Each platform is also internally cooled by an impingement plate feeding the film cooling holes.

6.2 Test rig and experimental measurements

In this section, a brief explanation of the experimental technique exploited by [106], with the only purpose to present the geometry and clarify some aspects that will emerge during results discussion, since experiments are not subject of this thesis.

The experimental campaign was conducted in a transonic test facility of GE Oil & Gas in Florence. A screw compressor provide a maximum flow rate of 0.86 $kg\ s^{-1}$; pressurized and filtered air goes through an orifice, a control valve, a plenum chamber equipped with flow straighteners and an inlet mouth before entering in the cascade test section. The desired cascade inlet pressure and mainstream mass flow were set acting on two valves located upstream and downstream the test rig and throttling the bypass line.

The test section, reported in Figure 6.1, represents an annular cascade with three passages. The central passage is composed by the first stage vane of a heavy duty GT with complete internal and external cooling system. The axial chord of the vane is about 54 mm, while the inlet foil span is about 84 mm.

The design of the test rig was achieved through a CFD design procedure considering several configurations varying the angle of exhaust duct, shape of the tailboards and rotation of the vane with respect to the tailboards. The final aim was to match main-stream Reynolds and Mach number similarity and a relative pressure distribution over the blade surface similar to the engine condition. Since three vanes are not completely sufficient to impose the same flow condition expected in the engine, some discrepancies in the flow field are expected especially near the hub/tip and at the trailing edge. For these reasons, the CFD survey was conducted following two final goals: achieve the same air split between the three passages and obtain at the midspan a pressure distribution as close as possible to the engine reference condition. Following these guidelines, in the final design of the test rig the vanes are not centered with respect to the tailboard (0.7° rotation along radial axis); moreover the tailboards angles at the test

section outlet follow the shape of the vane and the outer of the exhaust duct has an additional 4° of opening angle.

The design of the test model considered the use of real engine hardware inside an annular cascade: this feature allows also to reproduce radial pressure gradients and the three dimensional effects in the main flow field [107].

For details about the PSP technique see Section 2.4.2.

6.2.1 Test condition

Main-stream Reynolds number was set around $1.18 \cdot 10^5$, while the inlet Mach number was ≈ 0.08. The value of Reynolds number reached in the cascade represents roughly the 50% of the Reynolds expected at design condition.

Concerning the cooling system, the main investigation parameter is the coolant consumption defined as:

$$W = \frac{\dot{m}_{cool;tot}}{\dot{m}_{main;tot}} \cdot \frac{3}{2} \tag{6.1}$$

where the factor 3/2 is used to take into account that the cascade has three passages for the main flow and two active foils for coolant injection. Adiabatic effectiveness test were carried out imposing different values of W: during the test the outer and inner coolant plenum chambers were fed setting the same static pressure in both chambers and mainstream and cooling flow were delivered to the rig at the same ambient temperature.

The coolant consumption is an important design parameter that can be considered proportional to the global Blowing Rate of the vane film cooling system:

$$BR = \frac{\dot{m}_{cool;tot} A_{main;inlet}}{\dot{m}_{main;tot} A_{cool}} \propto W \tag{6.2}$$

where A_{cool} is the total exit area of film holes manufactured on vane geometry.

According to the definition of L'Ecuyer and Soechting [21], the velocity ratio is considered the driving parameter of behaviour of film cooling jets

Table 6.1: Real nozzle case: test conditions

Re_{main}	$1.18 \cdot 10^5$
Ma_{main}	0.08
$T_{main} = T_{cool}$	300 K
$W = W/DR$	6%

working in the mixing regime, as it is for the conditions of the present survey. The global velocity ratio of the vane cooling system can be considered proportional to the ratio of W/DR:

$$VR = \frac{\dot{m}_{cool;tot} A_{main;inlet}}{\dot{m}_{main;tot} A_{cool}} \cdot \frac{\rho_{main}}{\rho_{cool}} \propto W/DR \tag{6.3}$$

Table 6.1 summarizes all the test conditions in terms of cooling and main mass flows compared with the actual design condition.

6.3 Numerical analysis

6.3.1 Correlative approach (*BANKS*)

Procedure-supporting CFD simulations Steady-state CFD RANS calculations have been performed with the commercial 3D Navier-Stokes solver ANSYS® CFX v.14. In Figure 6.2, the numerical domain is reported. Solid surfaces are treated as smooth, no-slip walls. Since the experiments are conducted in adiabatic way, all the surface are considered adiabatic. The flow path boundary conditions have been recovered from the experimental measurements, in terms of total pressure, total temperature, turbulence intensity and length scale values at the inlet, and outlet static pressure at the outlet.

ANSYS® ICEM-CFD has been used to generate hybrid computational grids (tetrahedral with 20 layers of prisms close to the wall). The result is a mesh of 16.5 million elements (with a y^+ on the blade below 0.5).

For more details about the numerical setup, see Section 2.1.

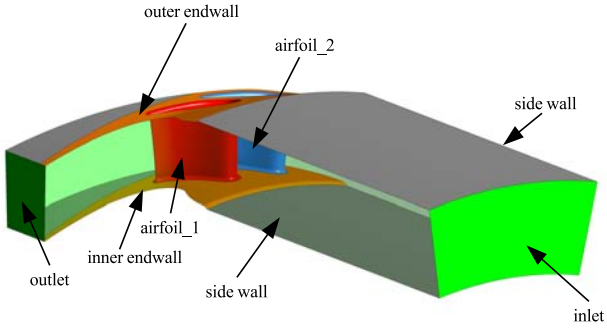

Figure 6.2: Real nozzle case: numerical domain

Fluid network setup In the fluid network solver, the cooling scheme is modelled through a pattern which discretizes all the cooling features of both blade and platform cooling. The coolant pattern from the internal impingement plate feeding showerhead, film cooling holes and trailing edge slots has been reproduced. All geometrical data required by the fluid network solver for defining the model, have been provided by GE Oil & Gas.

The one-dimensional fluid dynamics is resolved using correlations from a traditional set (see Appendix Heat transfer coefficient estimation correlations), for fully developed flows. In particular, for the evaluation of adiabatic effectiveness the two correlations presented in Section A.1: L'Ecuyer and Soechting [21] and Baldauf et al. [25]. The superposition criterion by Seller [105] has been applied (see Section A.1.3).

Coolant inlet boundary conditions, in terms of P_{tot} and T_{tot}, are retrieved from experimental data. External film cooling (related to the main flow) conditions are evaluated from the procedure-supporting CFD simulations.

6.3.2 Film cooling model

Regarding the numerical domain exploited in *FCM*, the vary same arrangement of test rig: this is pursued in order to better assess the presented methodology (Figure 6.2). It is the same domain exploited in *BANKS*-supporting CFD simulations.

Regarding mainflow boundary conditions, experimental derived data are retrieved (as for *BANKS*). Coolant conditions needed by the model, in terms of massflow rate, temperature and pressure are retrieved from correlative approach results.

Concerning the general numerical setup, the same considerations provided for correlative approach CFD are retrieved.

Following the validation procedure results, $elm/D = 5$ and $elm/D = 20$ hole discretization has been studied: it is been proved how intermediate condition ($elm/D = 10$) provides intermediate results. Regarding injection volume shape, only delimited cylinder shape has been retrieved as results of the model validation campaign. In this case too, the numerical grid is composed by an hybrid (tetra and 20 prism layers at the solid walls) unstructured mesh: the resulting meshes for the two studied cases move from a 19 million nodes mesh ($elm/D = 5$ case) to a 24 million nodes mesh ($elm/D = 20$ case).

Finally, only the airfoil (named $airfoil\_1$ in Figure 6.2), has been considered for the film cooling study, i.e. only in its surface are present injection volumes, since the two airfoils boundary conditions are the same, leading to a very similar behaviour in terms of coolant consumption and distribution. However, for the endwall cooling analysis purpose, both inner and outer film cooling rows have been considered. Totally, 500 injection volumes have been applied.

6.4 Results

First of all, general film cooling features of this vane are presented, comparing contour of adiabatic effectiveness resulting from experimental data and film cooling modelling.

Figure 6.3 shows the adiabatic effectiveness distributions over the airfoil. As shown in the picture, in correspondence of the stagnation point, the first row of showerhead holes of the PS is not able to generate a protective film around the leading edge. On the other hand, traces coming out from the other rows especially on the suction side can be detected on the vane: this indicates that, despite the fact that LE holes are mainly designed for metal cooling purposes, with a high radial orientation to increase their capability of heat removal by convection, they give a significant contribution to film protection.

Focusing on the pressure side, results highlight how the film cooling

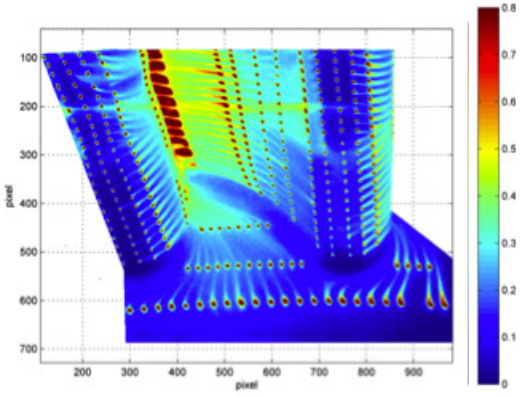

(a) PSP

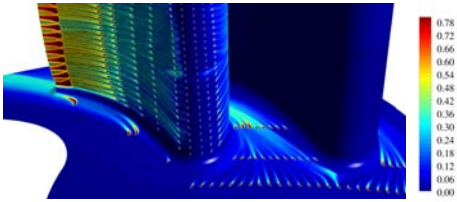

(b) FCM

Figure 6.3: Real nozzle case: coolant distribution on inner endwall and PS

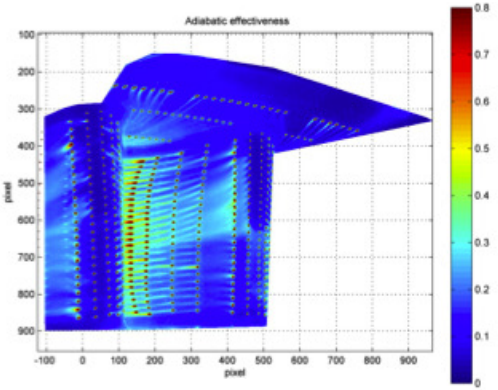

(a) PSP

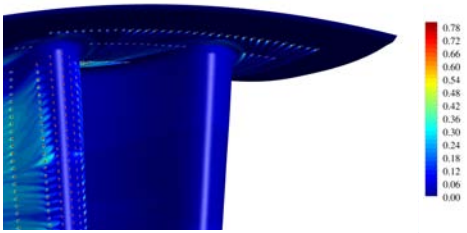

(b) FCM

Figure 6.4: Real nozzle case: coolant distribution on outer endwall and PS

superposition improves the wall protection: the adiabatic effectiveness growth row by row and after the 4^{th} row of FC-PS the airfoil is covered by a more homogeneous film distribution along the radial direction. Similarly to the behavior of the SS, the last row of showerhead on PS contributes to film cooling protection through the generation of straight coolant traces before the first FC row.

The film cooling distribution generated by showerhead holes allows

also to detect the position of the stagnation point along the span. Moving from the pressure to the suction sides, the first two rows of SH discharge coolant on the PS while the remaining three rows on the SS: this feature indicates that the stagnation line is located between the second and the third row.

At the trailing edge, the high amount of coolant coming from the upstream rows and moreover the presence of the slots guarantee a very efficient protection of this critical part of the vane. Looking at Figure 6.3a, it is possible to observe that the slot closest to the hub does not discharge coolant: in fact it was damaged and probably clogged during its functioning in a real HD gas turbine.

Figures 6.4 and 6.3 illustrate also the film behaviour on the outer and inner endwalls. The coolant is distributed around the leading edge, following the curvature of the airfoil; thanks to the film cooling superposition a good protection is obtained and an high-effectiveness area can be appreciated roughly from the location of the throat to the TE. The outer and inner fillets in the vane passage are subjected to a lower spread protection moving towards the vane throat while, due to the presence of well-know horseshoe vortex, the coolant injected trough the platform in front of the LE does not reach the foil and it left the fillet uncovered.

6.4.1 Blade film cooling

In this section, a more quantitative comparison between experimental data, BANKS and *FCM* results are presented.

Looking at Figure 6.6, the comparison has been performed in terms of span-averaged η_{aw} profile on the PS, only from the 2^{nd} row of Figure 6.5. As the upstream SH rows present an inclination angle from the profile higher than 90°, the considered correlations are not applicable. For this reason, it has been chosen to compare experimental and *BANKS* results only downstream the 2^{nd} row (Figure 6.5), where both correlations are inside their validity ranges. Hence, in order to take into account the film cooling effectiveness generated by the upstream showerhead holes, a starting η_{aw} value has been superimposed: this value has been retrieved

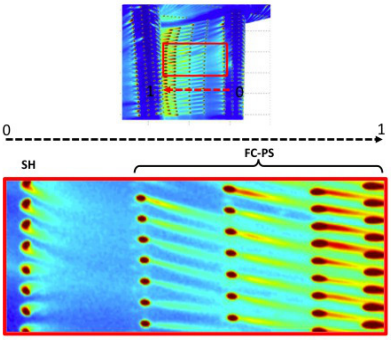

Figure 6.5: Real nozzle case: actual vane portion exploited in results comparison

from experimental results, looking at the adiabatic effectiveness measured immediately upstream the 2^{nd} row. However, for film cooling modelling, all the film cooling rows have been considered.

As depicted in Figure 6.6, predicted and measured values present a good agreement in terms of both η_{aw} trends and levels. It is important to stress that, since the position of cameras utilized in experimental tests leading to sensible stretched images, experimental effectiveness peaks result slightly placed upstream the numerical ones. Regarding the zone placed downstream the 3^{rd} row, it is possible to see a separation between the three profiles: the 4^{th} row presents an inclination angle below the minimum value accepted for both the correlations. Baldauf's correlation is more sensible to this parameter, showing a greater peak value, leading to an overestimation of cooling effectiveness. Looking at *FCM* profiles, $elm/D = 5$ hole discretization shows to same over-prediction of η_{aw} presented in the validation analysis, while $elm/D = 20$ results are in better agreement with experimental data. The two hole discretizations of film cooling model show a good prediction of both trends and levels especially from the second row.

In conclusion, correlative approach and *FCM* modelling are confirmed

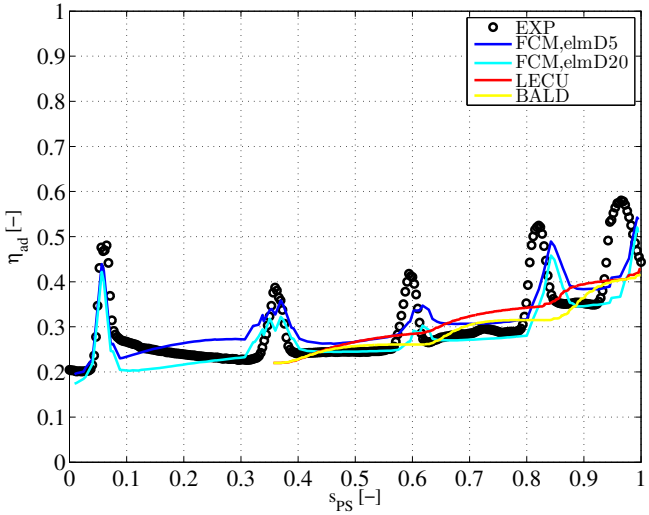

Figure 6.6: Real nozzle case: span-wise averaged η_{aw} profiles comparison

to be powerful and reliable tools in airfoil film cooling design.

6.4.2 Endwall film cooling

Regarding endwall film cooling analysis, the comparison has been performed along the same streamlines used during the platform film cooling estimation. Looking at Figure 6.7, the outer and inner platforms streamlines have been grouped in different portions: *Zone 1* covers the platform part between the SS of $airfoil\_2$ and the wall, *Zone 2* is related the central channel and *Zone 3* regards the portion of platform from the PS of $airfoil\_1$ and the side wall. Since there are two non-complete film cooling rows (*IN7* e *IN8* in Figure 6.7a), *Zone 2* has been divided in 2 parts: *Zone 2a* and *Zone 2b*. A span-wise average process has been applied to every portion to compare results.

In this case, a direct confrontation with experimental data was not possible, since the optical access of camera used to acquire images for

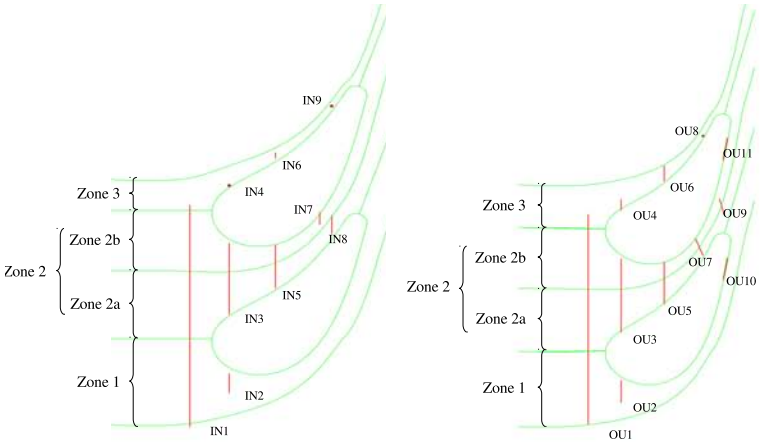

(a) Inner platform *(b) Outer platform*

Figure 6.7: Real nozzle case: endwall cooling scheme and zone definition

PSP technique. Hence, only a comparison between *BANKS-3D* and *FCM* model is presented.

In Figures 6.8 and 6.9, adiabatic effectiveness profiles for inner and outer platform are reported, respectively. As it is possible to observe in the zones associated to the central canal, there is an overestimation of *FCM* predictions compared to correlative results, localized around the last row of holes: this discrepancy is due to the particular geometry configuration and position (here not reported due to confidentiality agreement) of these rows, that are difficult to represent by a 1-D correlative approach. However, concerning the first part of the two endwalls, a good agreement between the proposed film cooling model and the correlative approach can be found. As said, differences are mainly related to the complex 3-D flow of the hot gas, not caught by *BANKS-3D*.

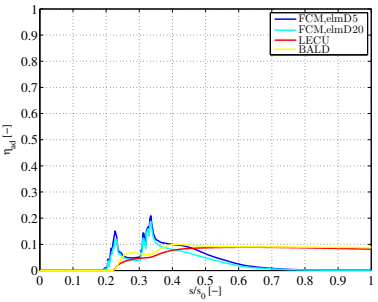

(a) Zone 1

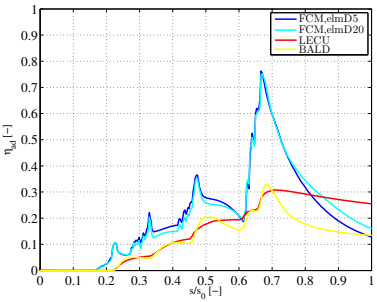

(b) Zone 2

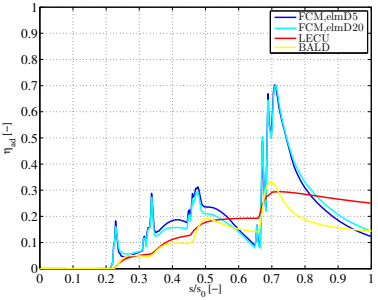

(c) Zone 2a

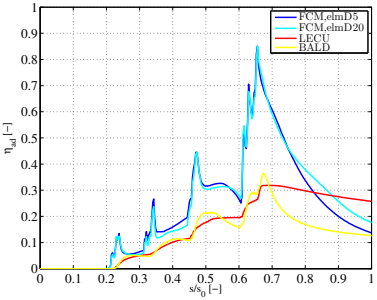

(d) Zone 2b

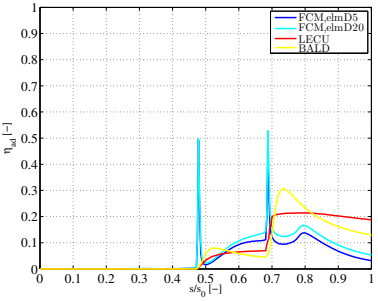

(e) Zone 3

Figure 6.8: Real nozzle case: span-wise averaged adiabatic effectiveness profiles on inner platform

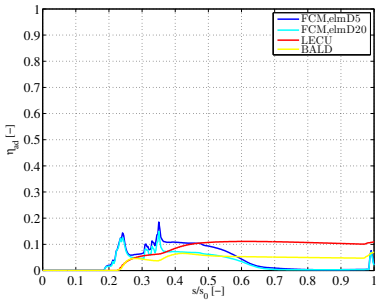

(a) Zone 1

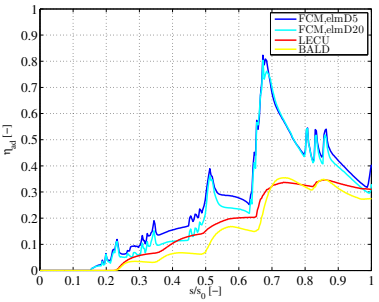

(b) Zone 2

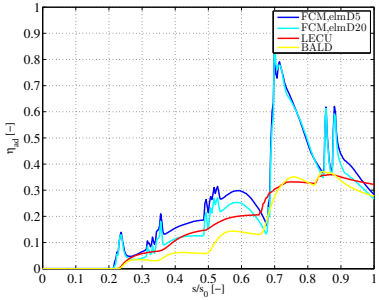

(c) Zone 2a

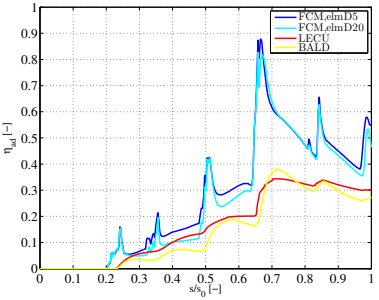

(d) Zone 2b

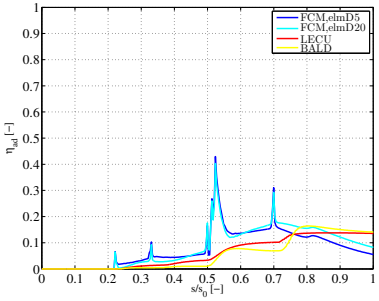

(e) Zone 3.

Figure 6.9: Real nozzle case: span-wise averaged adiabatic effectiveness profiles on outer platform

Conclusions

All the major components of gas turbines have reached a high level of development. Therefore, it became essential to efficiently integrate the design of cooling systems with thermal and structural analysis of the components, in order to verify the stress field and lifespan. The design of components such as gas turbine blades and vanes, requires specific procedures and several computational tools that must keep up with scientific development. In the framework of CFD, this has to be achieved with manageable computational effort.

For these reasons, a systematic analysis of the performance of unconventional RANS turbulence models specifically developed for film and effusion cooling applications has been performed under a wide range of coolant conditions including single and multi row film cooling geometries. This benchmark showed that compared with standard multi-purpose turbulence models, unconventional models usage improves the level of accuracy of the computations. Moreover from the results, it is not possible to indicate a single model able to predict the complex thermal field correctly at all conditions, even if the algebraic anisotropic correction to SST model proved to be the most reliable in case of multi perforated plate. On the other hand, the necessity of such turbulence formulation of a clear definition of development coolant streamlines to correct the lateral jet spreading, results in a difficult application to film-cooled blades and nozzles study, where the coolant pattern is not known a priori. It is important to highlight that mesh requirements for the study of only a hole are not compatible to industrial design requirements: in a real nozzle,

in fact, about 800 perforations are present.

Therefore, fully resolving real film cooling scheme is possible but not feasible in a design environment from an economical standpoint. The development of a method to simulate film cooling flows in 3D-CFD without having to fully resolve the flow inside the cooling holes promises to mitigate this issue.

This research work presents an innovative CFD model (called *FCM*) able to simulate flows ejected from cylindrical film cooling holes in 3D-CFD, describing the film-jet in terms of its shape and the distribution of temperature and velocity components within the film-jet body, avoiding the meshing process of perforations. The presented model couples low order models (correlative approaches) providing coolant boundary conditions, to 3D-CFD calculations, studying the evolution of the jet inside the hot gas flow path. The film cooling model is implemented in ANSYS® CFX, using user subroutines, available in the code in order to add additional features and physical models. Two injection volume shapes are considered: a cylindrical shape and a delimited cylinder shape. The first shape is a cylinder oriented along the same axis of the perforation and extended until the edge of the hole. The second shape is the same of the previous, but delimited from the surface of injection by a fixed distance of 5% of the hole diameter.

Regarding the correlative approach exploited to provide the coolant boundary conditions, it is a conjugate procedure (named *BANKS-3D*) aimed to predict cooling performances and metal temperatures of gas turbine blades and nozzles. Required inputs are evaluated by different tools: CFD, in-house fluid network solver and thermal FEM.

The *FCM* methodology has been tested in different configuration, in terms of ability to predict adiabatic effectiveness, showing to be a very powerful tool: tested film cooling configurations comprehend single and multi row film-cooled plates (the same tested during the turbulence model benchmark study) and complete complex cooling scheme of a vane. Results are compared against full hole discretization, experimental data and an in-house developed correlative approach. With the exception of

the single row case (due to the particular configuration), the film cooling model prediction are in good agreement with the respective full CFD ones in terms of both values and trends.

Finally, an actual test case has been studied. The component analysed in this work is a nozzle of a GE Oil & Gas heavy-duty gas turbine. In order to assess the model accuracy, results are compared to experimental results and correlative approach. Experiments were conducted using the PSP technique: the application of this measurement technique to a real nozzle is one of the most advanced and recent state-of-the-art result available in literature. Comparisons have been conducted both qualitatively and quantitatively, in terms of effectiveness distributions and profiles on studied airfoil and endwalls, confirming *FCM* to be a powerful and reliable tool in industrial film cooling design.

The next step is to improve the present film cooling model integrating it in a conjugate calculation, in order to evaluate thermal field and metal temperature: this will be possible following the same approach applied to coolant injection volumes, i.e. finding elements of the solid domain (representing the metal) associated to perforations, and applying them source terms, function of the removal of thermal power due to convection within the holes. Thermal boundary conditions inside the hole (heat transfer coefficients and adiabatic wall temperatures) will be evaluated through the same correlative approach exploited in the present work.

Appendix A

Correlations implemented in *BANKS-3D*

A.1 Adiabatic effectiveness estimation correlations

A.1.1 L'Ecuyer and Soechting correlation

Examining the trends from data presented by Pedersen et al. [22], L'Ecuyer and Soechting [21] provide an effectiveness equation capable of representing the varied effectiveness distributions from all the above regimes. They arrived at a correlation for film effectiveness based on the moving energy sink solution presented by Kadotani and Goldstein [108]:

$$\overline{\eta}_{aw} = \eta_p \left(\frac{\beta}{\beta_p}\right)^{\frac{a-1}{2}} e^{\frac{1}{2}\left[1-\left(\frac{\beta}{\beta_p}\right)^{a-1}\right]} \tag{A.1}$$

where η_p is the peak effectiveness value, β is the local effectiveness location, β_p is the peak effectiveness location, and the term a represents the exponent corresponding to the power law decay of the turbulent thermal diffusivity. The above equation is modified based on local effectiveness

location in relation to peak effectiveness location, so that:

$$\beta < \beta_p \longrightarrow \overline{\eta}_{aw} = \eta_p \left(\frac{\beta}{\beta_p}\right)^{\frac{a-1}{2}} e^{\frac{1}{2}\left[1-\left(\frac{\beta}{\beta_p}\right)^{a-1}\right]} \tag{A.2}$$

$$\beta > \beta_p \longrightarrow \overline{\eta}_{aw} = \eta_p \left(\frac{\beta}{\beta_p}\right)^{-\frac{1}{2}} e^{\frac{1}{2}\left[1-\left(\frac{\beta}{\beta_p}\right)^{-1}\right]} \tag{A.3}$$

$$\beta \gg \beta_p \longrightarrow \overline{\eta}_{aw} = \eta_p \sqrt{\beta_p} e^{\frac{1}{2}} \beta^{\frac{1}{2}} \tag{A.4}$$

Three empirical constants (η_p, $\eta_p\sqrt{\beta_p}$) and a) are required for curve fit measured effectiveness data. The term a was selected to obtain the best fit for the data. Curve fitting the data of Pedersen et al. [22], Gold-

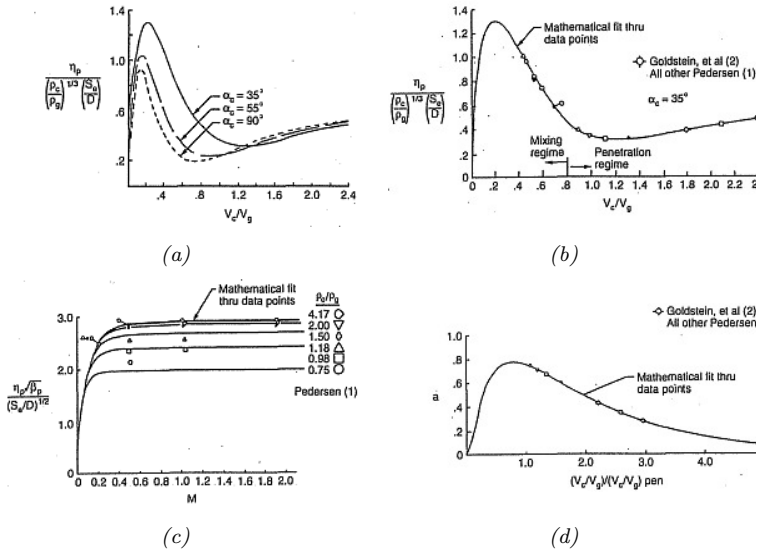

Figure A.1: Correlation of the peak effectiveness, downstream effectiveness and thermal diffusivity parameters using experimental data (a,b,c). Adjustments required in correlating peak effectiveness as a function of velocity ratio (d) (Source [21])

Table A.1: Validity range for L'Ecuyer and Soechting correlation

Injection angle (α)	$35^\circ < \alpha < 90^\circ$
VR	$0 < VR < 2.4$
BR	$0 < BR < 2$
DR	$0.75 < DR < 4.2$
VR over VR_{pen}	$0 < VR/VR_{pen} < 5$

stein et al. [109], Blair and Lander [110] and Muska et al. [111] resulted in the constants shown in their paper. Figure A.1a, Figure A.1b and Figure A.1c show the correlation of the peak effectiveness parameter, the downstream effectiveness parameter and the thermal diffusivity parameter using the above correlation. Figure A.1d shows the adjustments required in correlating peak effectiveness (η_p) as a function of velocity ratio for the effect of hole injection angle. A decrease of peak effectiveness is observed at low velocity ratios as the injection angle is decreased. Two important points to highlight are that at high velocity ratios, peak effectiveness is insensitive to injection angle (penetrative regime). Also, the downstream effectiveness constant ($\eta_p\sqrt{\beta_p}$) is insensitive to the injection angle. However, the critical velocity ratio, defining the onset of the penetration regime and the peak effectiveness, was determined to be directly affected by changes in injection angle. Finally, in Table A.1, ranges of validity for the correlation are reported.

A.1.2 Baldauf et al. correlation

Baldauf et al. [25] presented a detailed study representing a database covering a large range of all dominating ejection parameters at consistent and carefully controlled experimental conditions. Also they developed a laterally averaged adiabatic effectiveness correlation for a single cylindrical hole in function of geometrical and fluid dynamic parameters:

$$\overline{\eta}_{aw} = f\left(BR, DR, Tu, \frac{x}{D}, \alpha, \frac{s}{D}, \frac{t}{D}, \frac{L}{D}\right) \tag{A.5}$$

where x is the distance from the hole, D is the hole diameter, α is the injection angle, s hole distance.

In this work the authors concluded that the development of the cooling effectiveness is governed by the interplay of two phenomena: the single jet in crossflow mixing and the adjacent jet interaction. The cooling film development is distinctively determined by the ejection geometry, characterized by hole angle and spacing, and influenced by the density ratio. Therefore, even the modeling of basic effects needs to account for the whole database. The characteristic feature of the large majority of all measurements is the peak of the laterally averaged effectiveness curves due to the single jet in crossflow behaviour. The correlation of L'Ecuyer and Soechting [21] already demonstrated that effectiveness curves of different ejection situations often can be considered similar, and the laterally averaged effectiveness level can be characterized by the peak value. Using these findings, the new effectiveness correlation was set up as follows:

- The basic jet in crossflow behaviour forms a typical base curve. It displays rising effectiveness towards a peak value, due to coolant spreading and closed cooling film formation, followed by an exponential decay. The typical height of this peak depends on the ejection situation and needs a systematic description of the specific peak value and position. Normalizing all single curves by their maxima should bring all similar curves of jet in crossflow characteristic on top of each other. The collapsed curves should yield the laws for the effectiveness rise and decay of the base curve.

- The ejection cases, dominated by the adjacent jet interaction, must deviate from this base curve after normalization. Especially their maximum peaks are not expected to match the description lined out before. The systemized divergence of the maximum peaks should allow formulating a common description of all cases on one base curve.

- With all curves pinched to common maximum values, deviations of

Table A.2: Validity range for Baldauf et al. correlation

Injection angle (α)	$30° < \alpha < 90°$
BR	$0.2 < BR < 2.5$
DR	$1.2 < DR < 1.8$
hole pitch over diameter	$2 < s/D < 5$

the downstream decay due to the adjacent jet interaction will remain. A final systemization of these deviations should yield one common curve and correlation of laterally averaged adiabatic effectiveness.

Quantifying the effects of the jet in crossflow and the adjacent jet interaction, a complete correlation was processed to evaluate the average spanwise effectiveness trend:

$$\overline{\eta}_{aw} = \eta_c \frac{DR^{\frac{0.9}{s/d}}}{sin\alpha^{0.06\frac{s}{d}}} \tag{A.6}$$

Definition and description of the parameters considered in the correlation can be retrieved in Baldauf et al. [25]. In Table A.2 ranges of validity for the correlation are reported.

A.1.3 Sellers superposition model

Technical literature does not offer open theoretical expressions to predict film effectiveness in multi-rows configurations. Therefore, it is necessary to adopt theoretical approaches to take into account film superposition. Among the few published works concerning film superposition, the most relevant is the model proposed by Seller [105] which is observed to be sufficiently accurate to predict the adiabatic effectiveness distribution at least for the first rows of holes (see for example the works by Harrington et al. [112], Ceccherini et al. [113]).

The principle of Seller's superposition method, originally formulated for slot cooling, can be summed up, in the case of two rows of film cooling

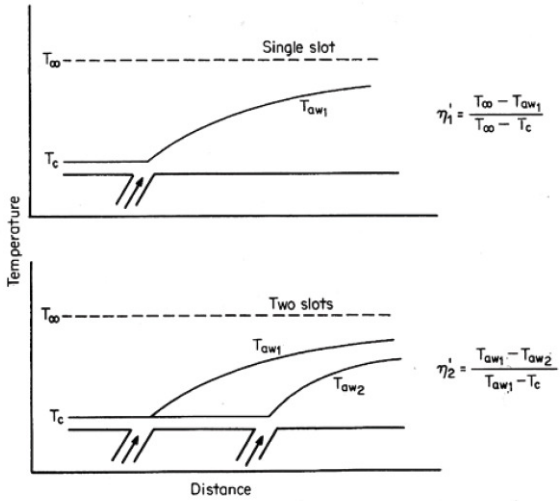

Figure A.2: Adiabatic wall temperature: Sellers superposition principle (Source [105]).

(Fig.A.2), in the following expression :

$$\eta_2 = \eta'_1 + \eta'_2 \left(1 - \eta'_1\right) \tag{A.7}$$

with:

$$\eta_2 = \frac{T_{aw2} - T_\infty}{T_c - T_\infty} \tag{A.8}$$

and:

$$\eta'_1 = \frac{T_\infty - T_{aw1}}{T_\infty - T_c} \tag{A.9}$$

$$\eta'_2 = \frac{T_{aw1} - T_{aw2}}{T_{aw1} - T_c} \tag{A.10}$$

where η'_1 is the adiabatic effectiveness of the first row of holes calculated in the axial position downstream of the second row, while η'_2 is the effectiveness of the second row without the presence of the first one.

The implicit assumption of this method is that, in the region downstream of the second slot injection, the adiabatic wall temperature of the first slot can be considered as the gas temperature T_g. This is shown schematically in Figure A.2.

So, for N rows of holes, an expression for the effectiveness of the region placed between the i^{th} and the i^{th+1} line is necessary ($i = 1 \dots N$). Equation A.11, formulated for modelling the coverage effect of two slots of film-cooling, can be generalized for N slot in the following way:

$$\begin{aligned}\eta_N = \eta'_1 + \eta'_2 \cdot \left(1 - \eta'_1\right) + \eta'_3 \cdot \left(1 - \eta'_1\right) \cdot \left(1 - \eta'_2\right) + \dots \\ \dots + \eta'_N \cdot \left(1 - \eta'_1\right) \cdot \left(1 - \eta'_2\right) \cdot \dots \cdot \left(1 - \eta'_{N-1}\right)\end{aligned} \tag{A.11}$$

so:

$$\eta'_i = \frac{T_{aw,i-1} - T_{aw,i}}{T_{aw,i-1} - T_c} \qquad (i = 1, 2, \dots N-1) \tag{A.12}$$

and, as above-mentioned, the adiabatic temperature which derives from the i^{th-1} line upstream, is assumed as the mainstream temperature downstream of the i^{th} row.

This model proposed by Seller is a purely algebraic pattern, which however well fits the phenomenon guaranteeing, a value of η_N always lower than the unit, respecting so the physical meaning of the parameter.

Generally, for the case of rows of holes, the presence of strongly three-dimensional interactions leads to get worse the performance prediction of the superposition method.

A.2 Heat transfer coefficient estimation correlations

Here are presented the heat transfer coefficient correlations for turbulent flow in circular tubes implemented in *BANKS-3D*.

Since the analysis of heat transfer to turbulent flow is much more complex than that for laminar flow, during the years a large number of empirical correlations have been developed to determine heat transfer coefficient.

Among the implemented correlations, some of the most well-known and widely used, are introduced:

- the *Colburn correlation*
- the *Nusselt correlation*
- the *Dittus and Boelter correlation*
- the *Gnielinski correlation*

A.2.1 Colburn correlation

The Colburn [114] equation is based on the *Reynolds-Colburn analogy* which refers to the theory and equations elaborated to describe fluid dynamic conditions inside the boundary layer and in this case readapted to the study of boundary layer in a circular tube. From an engineering point of view, the interest in boundary layer behaviour is directed principally toward dimensionless parameters such as friction coefficient C_f, Nusselt number Nu and Stanton number St. From the knowledge of these parameters, it is possible to compute the wall shear stress and the convection heat and mass transfer rates. It is therefore understandable that expressions that relate C_f, Nu and St to each other can be useful tools in convection analysis. Such expressions are available in the form of boundary layer analogies.

For a laminar flow along a flat plat, a relation between the local heat transfer coefficient HTC_x and the local friction coefficient has been

developed, as shown by Equation A.13 (for more details see [115, 116]):

$$St_x \, Pr^{2/3} = \frac{C_f}{2}. \tag{A.13}$$

where:

$$St_x = \frac{Nu_x \, Re_x}{Pr} = \frac{HTC_x}{\rho \, c_p \, u_\infty} \, . \tag{A.14}$$

St_x is the Stanton number on the surface, and C_f is the friction coefficient whose expression, obtained from the boundary layer analysis for external flows on a flat plat, is [115]

$$C_f = \frac{\tau_s}{\rho \, {u^2}_\infty / 2} \tag{A.15}$$

where the subscript ∞ is used to designate conditions in the free stream outside the boundary layer, and τ_s represents the surface shear stresses acting in planes that are parallel to the fluid velocity.

For turbulent flow inside a circular tube a similar expression is given by Equation A.16 [116]:

$$St_x \, Pr^{2/3} = \frac{f}{8} \qquad \text{for} \quad 0.6 < Pr < 60 \tag{A.16}$$

where:

$$St = \frac{Nu \, Re}{Pr} = \frac{HTC}{\rho \, c_p \, u_m} \, . \tag{A.17}$$

f is the friction factor inside the tube and it is correlated to the other quantities of the boundary layer through the Equation A.18:

$$\frac{f}{8} = \frac{\tau}{\rho \, {u^2}_m / 2} \tag{A.18}$$

which is analogous to the equation of C_f for flow along a flat plat [116].

Equation A.16 is known as the Reynolds analogy for heat transfer, and it relates the key engineering parameters of the velocity, thermal, and concentration boundary layers. If the velocity parameter is known, the analogy may be used to obtain the other parameters, and vice versa. The analogy is applicable at every point on a surface and it may be applied to

the surface average coefficients [115].

The friction factor f can be estimated using the Moody chart, but for turbulent flow in smooth pipes it is possible to use as a first approximation the Equation A.19 [116]:

$$f = 0.184\, Re^{-0.2} \qquad \text{for} \quad 2 \cdot 10^4 < Re < 3 \cdot 10^5 \tag{A.19}$$

Substituting Equation A.19 into Equation A.16, it results:

$$St\, Pr^{2/3} = 0.023\, Re^{-0.2} \tag{A.20}$$

and considering that:

$$St = \frac{Nu\, Re}{Pr} \tag{A.21}$$

the Colburn equation for turbulent flow inside a smooth tube is [116]:

$$Nu_D = 0.023\, Re^{0.8}\, Pr^{1/3} \tag{A.22}$$

whose range of applicability is:

$$\begin{bmatrix} 0.7 < Pr < 160 \\ Re_D > 10000 \\ \frac{L}{D} > 10 \end{bmatrix}$$

$$Q = HTC \cdot A \cdot (T_w - T_{ref}) \tag{A.23}$$

The equation may be used for small to moderate temperature differences ΔT, with all properties evaluated at the bulk mean fluid temperature T_m [116]. Referring to Equation A.23 it is useful to introduce at the place of T_{ref}, the parameter T_m which represents the mean temperature of the flux and which is a convenient reference temperature for internal flows, playing much the same role as the free stream temperature T_g for external. However, there is an essential difference between T_m and T_g. Whereas T_g is assumed to be constant at infinite distance from the surface, and it remains like that in the flow direction, T_m must vary in this direction. That means, (dT_m/dx) is never zero if heat transfer is occurring. The

value of T_m increases with x if heat transfer is from the surface to the fluid ($T_w > T_m$); it decreases with x if the opposite is true ($T_m > T_w$)[115].

A.2.2 Nusselt correlation

The Nusselt [117] equation derives from the necessity to evaluate what appends from a fluid dynamic point of view for length to diameter ratios $L/D < 60$, since the earliest correlations were evaluated for $L/D > 60$, including the Sieder and Tate [118], Petukhov [119] and the Colburn [114] correlations.

Nusselt studied the experimental data supplied by Sieder and Tate [118] for L/D from 10 to 100 and concluded that HTC, in this region, is approximately proportional to $(D/L)^{1/8}$. So Nusselt elaborated the following correlation [116]:

$$Nu_D = 0.036\, Re^{0.8}\, Pr^{1/3} \left(\frac{D}{L}\right)^{0.055} \tag{A.24}$$

where L is the length measured from the beginning of the heat transfer section, and the fluid properties are evaluated at the bulk mean fluid temperature. This equation is applicable for:

$$\begin{bmatrix} 0.7 < Pr < 16700 \\ Re_D > 10000 \\ 10 < \frac{L}{D} < 400 \end{bmatrix}$$

A.2.3 Dittus-Boelter correlation

A slightly different form of Equation A.22 is the *Dittus and Boelter correlation*. For fully developed (hydrodynamically and thermally) turbulent flow in a smooth circular tube, the local Nusselt number may be

obtained from the following equation [1]:

$$Nu_D = 0.023\, {Re_D}^{4/5}\, Pr^n \tag{A.26}$$

where $n = 0.4$ for heating ($T_w > T_m$) and 0.3 for cooling ($T_w < T_m$). These equations have been confirmed experimentally for the range of conditions:

$$\begin{bmatrix} 0.6 \leq Pr \leq 160 \\ Re_D \geq 10000 \\ \frac{L}{D} \geq 10 \end{bmatrix}$$

The equations may be used for small to moderate temperature differences ΔT, with all properties evaluated at T_m [115].

A.2.4 Gnielinski correlation

Although Equations A.25 are easily applied and are certainly satisfactory for a first estimation, in general, errors as large as 25% may result from their use. Such errors may be reduced to less than 10% through the use of more recent, but generally more complex, correlations. One correlation, valid for smooth tubes over a large Reynolds number range including the transition region, is provided by Gnielinski [115]:

$$Nu_D = \frac{(f/8)\,(Re_D - 1000)\,Pr}{1 + 12.7\,(f/8)^{1/2}\,(Pr^{2/3} - 1)} \tag{A.27}$$

where the value of the friction factor f is evaluated by the fluid network solver using an internal tabular implementation of the Moody chart. The

[1] Although it has become common practice to refer to Equation A.26 as the Dittus-Boelter equation, the original equation forms are actually:

$$Nu_D = 0.0243\, {Re_D}^{4/5}\, Pr^{0.4} \qquad \text{(Heating)}$$
$$Nu_D = 0.0265\, {Re_D}^{4/5}\, Pr^{0.3} \qquad \text{(Cooling)} \tag{A.25}$$

correlation is valid for:

$$\begin{bmatrix} 0.5 \leq Pr \leq 2000 \\ 3000 \leq Re_D \leq 5 \cdot 10^6 \\ \frac{L}{D} \geq 10 \end{bmatrix}$$

and using Equation A.27 properties should be evaluated at T_m.

Equation A.25 through A.27 pertain to smooth tubes. For turbulent flow in rough tubes, the heat transfer coefficient increases with wall roughness, and, as a first approximation, it may be computed by using Equation A.27. However, although the general trend is one of increasing HTC with increasing f, the increase in f is proportionately larger, and when f is approximately four times larger than the corresponding value for a smooth surface, HTC no longer changes with additional increases in f [115].

Gnielinski correlation is widely used because of its large range of applicability and its higher level of accuracy. Also it have to be considered that a correlation developed for fully turbulent conditions ($Re_D > 10^4$), may be used as a first approximation, at smaller Reynolds numbers too, with the understanding that the convection coefficient will be overpredicted, while, on the contrary, caution should be exercised when applying a correlation developed for $Re_D < 10^4$ to a turbulent flow.

A.2.5 Entry region treatment in circular tubes

Heat transfer correlations, based on experimental results, are typically divided into those applicable in the thermal entrance region, and those that apply in the "fully developed" region. The behaviour and characteristics of the flow in the entrance region are different from the case of a fully developed one, and different treatments have to be applied for the evaluation of the heat transfer coefficient along the tubes according to their length.

A.2.5.1 Long and short tubes

Entry lengths for turbulent flow are typically short, $10 \leq (x_{fd}/D) \leq 60$, and for cooling application it is generally assumed fully developed turbulent flow for $(x/D) > 10$. Fully developed flow implies that the tube is long compared with the entrance length in which the velocity distribution at the inlet adjusts itself to the geometry and no longer changes with distance along the tube. Therefore it is often reasonable to assume that the average Nusselt number for the entire tube is equal to the value associated with the fully developed region, $\bar{Nu}_D \approx Nu_{D,fd}$. Typically, errors of less than 15% are associated with assuming $\bar{Nu}_D = Nu_{D,fd}$, for $(L/D) > 60$ [115].

However, for short tubes, i.e. ducts with $L/D < 10$, $\overline{Nu}_D$ will exceed $Nu_{D,fd}$ and may be calculated from an expression of the form [100]:

$$\frac{\overline{Nu}_D}{Nu_{D,fd}} = 1 + \left(\frac{C}{x/D}\right)^m \tag{A.28}$$

where C and m depend on the nature of the inlet (e.g., sharp-edged or nozzle) and entry region (thermal or combined), as well as on the Prandtl and Reynolds numbers.

A.2.5.2 Kreith correction

Kreith equation [120] is used to scale correlation written for tubes with $L/D > 10$ in order to make them usable also for short tubes. In these cases, as already mentioned in the previous paragraph, the Nu expression for a fully developed boundary layer has to be corrected to account the entrance region effects. The Kreith correction, written for this aim, assumes the form shown in Equation A.29:

$$Nu_D = Nu_0(1 + (D/L)^{0.7}) \tag{A.29}$$

where Nu_0 is the value calculated for the short tube with any correlation among those for long tubes $(L/D > 10)$.

In particular Equation A.29 can be useful to estimate the heat removed

by the passage of the coolant inside the holes. Considering the outlet hole as a duct, the correlations used for channels can be scaled by the Kreith correction to estimate the heat transfer. As the Equation A.29 suggests, the Nusselt number in a short tube is incremented compared to the case of Nusselt in long tubes: heat transfer is increased by a reduction of L.

Bibliography

[1] Moustapha, J., Zelesky, M. F., Baines, N., and Japikse, D. Axial and radial turbines. *Concepts NREC*, 2003.

[2] DeLuca, D. P. and Annis Jr., C. G. Fatigue in single crystal nickel superalloys. *Office of Naval Research*, (FR-23800), 1995.

[3] Arakere, N. J. High-temperature properties of single crystal superalloys in air and hydrogen. *ASME IGTI*, (2001-GT-0585), 2001.

[4] Naik, R. A., DeLuca, D. P., and Shah, D. M. Critical plane fatigue modeling and characterization of single crystal nickel superalloys. *ASME Journal of Engineering for Gas Turbines and Power*, (2001-GT-30300), 2004.

[5] Maclachlan, D. W. and Knowles, D. M. The effect of material on the analysis of single crystal turbine blades: Part i - material model. *Fatigue and Fracture Engineering Material Science*, (25):385–398, 2002.

[6] Maclachlan, D. W. and Knowles, D. M. The effect of material on the analysis of single crystal turbine blades: Part ii - component analysis. *Fatigue and Fracture Engineering Material Science*, (25): 385–398, 2002.

[7] Seetharaman, V. Thickness debit properties of pw1484. *Pratt and Whitney Materials and Processes Engineering, Interim Report*, 2002.

[8] Sims, C. t., Stoloff, N. S., and Hagel, W. C. *Superalloys II.* John Wiley & Sons, 1980.

[9] Torbidoni, L. and Horlock, J. H. A new method to calculate the coolant requirements of a high temperature gas turbine blade. *ASME Paper*, (GT2004-53729), 2004.

[10] Schlichting, H. *Boundary-Layer Theory.* McGraw-Hill, 1979.

[11] Cunha, F. J., Abdel-Messeh, W., and Chyu, M. K. Thermal analyis and durability design strategies for gas turbine airfoils. *Proceedings of ASME Turbo Expo*, (GT2006-91013), 2006.

[12] Goldstein, R. J. Film cooling. *Advances in Heat Transfer*, 7:357–358.

[13] Chyu, M. K. Heat transfer and pressure drop for short pin-fin arrays with pin-endwall fillet. *ASME Journal of Heat Transfer*, 112: 926–932, 1990.

[14] Zukauskas, A. A. Heat transfer from tubes in cross flow. *Advances in Heat Transfer*, 8:116–133, 1972.

[15] Goldstein, R. J., Eckert, E. R. G., and Burggraf, F. Effects of hole geometry and density on three-dimensional film cooling. *ASME J. Heat Transfer*, 1974.

[16] Han, J. C. Turbine blade cooling studies at texas a & m university - 1980-2004. *The 2004 AIAA Thermophysics Award Lecture*, 2005.

[17] Albert, J. E., Bogard, D. G., and Cunha, F. Adiabatic and overall effectiveness for a film cooled blade. *IGTI-ASME*, (GT2004-53998), 2004.

[18] Cunha, F. J., Dahmer, M., and Chyu, M. K. Analysis of airfoil trailing edge heat transfer and its significance in thermal mechanical design and durability. *ASME Journal of Turbomachinery*, (GT2005-68107), 2006.

[19] Bogard, D. G. Airfoil film cooling. *The Gas Turbine Handbook*, 2007.

[20] Han, J. C., Dutta, S., and Ekkad, S. *Gas Turbine Heat Transfer and Cooling Technology*. Taylor & Francis, 2000.

[21] L'Ecuyer, M. R. and Soechting, F. O. A model for correlating flat plate film-cooling effectiveness for rows of round holes. *AGARD-CP-390*, 1985.

[22] Pedersen, D. R., Eckert, E., and Goldstein, R. Film cooling with large density differences between the mainstream and the secondary fluid measured by the heat-mass transfer analogy. *ASME Journal of Heat Transfer*, 99:620–627, 1977.

[23] Dees, J. E., Bogard, D. G., Ledezma, G. A., and Laskowski, G. M. Overall and adiabatic effectiveness values on a scaled up, simulated gas turbine vane. *ASME J. Turbomach.*, 135, 2013.

[24] Mouzon, B. D., Terrell, E. J., Albert, D. G., and Bogard, D. G. Net heat flux reduction and overall effectiveness for a turbine blade leading edge. *ASME paper*, (GT2005-69002), 2005.

[25] Baldauf, S., Scheurlen, M., Schulz, A., and Wittig, S. Heat flux reduction from film cooling and correlation of heat transfer coefficients from thermographic measurements at enginelike conditions. *ASME J. TURBOMACH*, 124:699–709, 2002.

[26] Thole, K. A., Sinha, A. K., Bogard, D. G., and Crawford, M. E. Mean temperature measurements of jets with a crossflow for gas turbine film cooling application. *Rotating Machinery Transport Phenomena*, 1992.

[27] Sinha, A. K., Bogard, D. G., and Crawford, M. E. Film cooling effectiveness downstream of a single row of holes with variable density ratio. *ASME J. Turbomach*, 113:442–449, 1991.

[28] Cutbirth, J. M. and Bogard, D. Effects of coolant density ratio on film cooling. *ASME Gas Turbine Expo*, (GT2002-38582):1–10, 2003.

[29] Ethridge, M. I., Cutbirth, J. M., and Bogard, D. Scaling of performance for varying density ratio coolants on an airfoil with strong curvature and pressure gradients. *ASME Journal of Turbomachinery*, 123(GT2002-38582):231–237, 2001.

[30] Mayle, R.E., Kopper, F.C., Blair, M.F., and Bailey, D.A. Effect of streamline curvature on film cooling. *ASME Journal of Engineering for Power*, 99:77–82, 1977.

[31] Boyle, R. G. and Ameri, A. A. A correlation approach to predicting film cooled turbine vane heat transfer. *Proceedings of ASME Turbo Expo*, (GT2010-23597), 2010.

[32] Ito, S., Goldstein, R.J., and Eckert, E.R.G. Film cooling of a gas turbine blade. *ASME Journal of Engineering for Power*, 100: 476–481, 1978.

[33] Goldstein, R. J. and Taylor, J. R. Mass transfer in the neighborhood of jets entering a crossflow. *ASME J Heat Trans*, (104), 1982.

[34] Andreini, A., Facchini, B., Picchi, A., Tarchi, L., and Turrini, F. Experimental and theoretical investigation of thermal effectiveness in multi-perforated plates for combustor liner effusion cooling. *Proceedings of ASME Turbo Expo*, (GT2013-94667), 2013.

[35] Baldauf, S., Scheurlen, M., Schulz, A., and Wittig, S. Heat flux reduction from film cooling and correlation of heat transfer coefficients from thermographic measurements at enginelike conditions. *ASME J. Turbomach.*, 124:699–709, 2002.

[36] Acharya, S. Numerical modeling methods for film cooling. film cooling science and technology for gas turbine: State-of-the-art experimental and computational knowledge. *Von Karman Lecture Series*, (06), 2007.

[37] Andreopulos, J. On the structures of jets in cross-flows. *J. Fluid Mech*, (157):163–197, 1985.

[38] Walters, D. K. and Leylek, J. H. A detailed analysis of film-cooling physics: Part i-streamwise injection with cylindrical holes. *ASME J. Turbomach.*, (122), 2000.

[39] Leylek, J. H. and Zerkle, R. D. Discrete jet film cooling: A comparison of computational results with experiments. *ASME J. Turbomach.*, (116):358–368, 1994.

[40] Fric, T. F. and Roshko, A. Vortical structure in the wake of a transverse jet. *J. Fluid Mech.*, (279):1–47, 1994.

[41] Crabb, D., Durao, D. F. G., and Whitelaw, J. H. A round jet normal to a crossflow. *Trans. ASME: J. Fluids Eng*, (103), 1981.

[42] Galeazzo, F. C. C., Donnert, G., Habisreuther, P., Zarzalis, N., Valdes, R. J., and Krebs, W. Measurements and simulation of turbulent mixing in a jet in crossflow. *Proceedings of ASME Turbo Expo*, (GT2010-22709), 2010.

[43] Schluter, J. U. and Schonfeld, T. LES of jets in cross flow and its application to a gas turbine burner. *Flow, Turbulence and Combustion*, 65(2):177–203, 2001.

[44] Mendez, S. and Nicoud, F. An adiabatic homogeneous model for the flow around a multi-perforated plate. *AIAA Journal*, 10(46): 2623–2633, 2008.

[45] Hoda, A. and Acharya, S. Predictions of a film coolant jet in crossflow with different turbulence models. *ASME J. Turbomach.*, 122:558–569, 2000.

[46] Harrison, K. L. and Bogard, D. G. Comparison of RANS turbulence models for prediction of film cooling performance. *Proceedings of ASME Turbo Expo*, (GT2008-51423), 2008.

[47] Bacci, A. and Facchini, B. Turbulence modeling for the numerical simulation of film and effusion cooling flows. *Proceedings of ASME Turbo Expo*, (GT2007-27182), 2007.

[48] Holloway, D. S., Walters, D. K., and Leylek, J. H. Computational study of jet-in-crossflow and film cooling using a new unsteady-based turbulence model. *Proceedings of ASME Turbo Expo*, (GT2005-68155), 2005.

[49] Bergeles, Gosman, G., and Launder, A. D. The turbulent jet in a cross stream at low injection rates: a three-dimensional numerical treatment. *Numerical Heat Transfer*, 1:217–242, 1978.

[50] Azzi, A. and Lakehal, D. Perspectives in modeling film cooling of turbine blades by transcending conventional two-equation turbulence models. *ASME J. Turbomach.*, 124:472–484, 2002.

[51] Mangani, L. and Andreini, A. Application of an objectoriented cfd code to heat transfer analysis. *Proceedings of ASME Turbo Expo*, (GT2008-51118), 2008.

[52] Andreini, A., Bianchini, C., Ceccherini, A., Facchini, B., Mangani, L., Cinque, G., and Colantuoni, S. Investigation of circular and shaped effusion cooling arrays for combustor liner application - Part 2: numerical analysis. *Proceedings of ASME Turbo Expo*, (GT2009-60038), 2009.

[53] Boust, B., Lalizel, G., Bianchini, C., Ceccherini, A., Cinque, G., and Colantuoni, S. Dual investigations on the improvement of effusion cooling by shaped holes. *7th World Conference on Experimental Heat Transfer, Fluid Mechanics and Thermodynamics*, 2009.

[54] Andreini, A., Bianchini, C., Facchini, B., Mangani, L., and Maritano, M. Heat transfer performances of fan-shaped film cooling holes. Part II - numerical analysis. *Proceedings of ASME Turbo Expo*, (GT2010-22809), 2010.

[55] Cottin, G., Laroche, E., Savary, N., and Millan, P. Modeling of the heat flux for multi-hole cooling applications. *Proceedings of ASME Turbo Expo*, (GT2011-46330), 2011.

[56] Li, X., Ren, J., and Jiang, H. Algebraic anisotropic eddy-viscosity modeling application to the turbulent film cooling flows. *Proceedings of ASME Turbo Expo*, (GT2011-45791), 2011.

[57] Walters, D. K. Development of novel turbulence modeling techniques for turbomachinery applications. *Clemson University, PhD thesis*, 2000.

[58] Weller, H. G., Tabor, G., Jasak, H., and Fureby, C. A tensorial approach to computational continuum mechanics using object-oriented techniques. *Computational Physics*, 12(6):620–631, 1998.

[59] Patankar, S. V. *Numerical Heat Transfer and Fluid Flow.* Taylor & Francis, 1980.

[60] Jasak, H. *Error Analysis and Estimation for the Finite Volume Method With Applications to Fluid Flows.* PhD thesis, Imperial College of Science, Technology and Medicine, London, 1996.

[61] Andreini, A., Bianchini, C., Facchini, B., and Mangani, L. Development and validation of a C++ object oriented CFD code for heat transfer analysis. *ASME-JSME 2007 Thermal Engineering and Summer Heat Transfer Conference*, 08-12/07/2007.

[62] Azzi, A. and Jubran, B. A. Numerical modeling of film cooling from short length stream-wise injection holes. *Heat and Mass Transfer*, 39:345–353, 2003.

[63] Lakehal, D., Theodoris, G. S., and Rodi, W. Computation of film cooling of a flat plate by lateral injection from arow of holes. *International Journal of Heat and Fluid Flow*, 19:418–430, 1998.

[64] Lakehal, D. Near-wall modeling of turbulent convective heat transport in film cooling of turbine blades with the aid of direct numerical simulation data. *ASME J. Turbomach.*, 124:485–498, 2002.

[65] Kim, J., Moin, P., and Moser, R. Turbulence statistics in fully developed channel flow at low reynolds number. *J. Fluid Mech.*, 177:133–166, 1987.

[66] Lien, F. S. *Computational modeling of* 3*-D flow in complex ducts and passages*. PhD thesis, University of Manchester, Institute of science and technology, 1992.

[67] Andrei, L., Andreini, A., Bianchini, C., and Facchini, B. Numerical benchmark of nonconventional RANS turbulence models for film and effusion cooling. *ASME J. Turbomach*, 135, 2013.

[68] Andrei, L., Andreini, A., Bianchini, C., Facchini, B., and Mazzei, L. Numerical analysis of effusion plates for combustor liners cooling with varying density ratio. *Proceedings of ASME Turbo Expo*, (GT2013-95039), 2013.

[69] Andrei, L., Andreini, A., Bianchini, C., Caciolli, C., Facchini, B., Mazzei, L., Picchi, A., and Turrini, F. Effusion cooling plates for combustor liners: Experimental and numerical investigations on the effect of density ratio. *Energy Procedia*, (45):1402–1411, 2014.

[70] Andreopoulos, J. Measurements in a jet-pipe flow issuing perpendicularly into a cross stream. *ASME J. Fluids Eng.*, 26:493–500, 1983.

[71] Andreini, A., Facchini, B., Picchi, A., Tarchi, L., and Turrini, F. Experimental and theoretical investigation of thermal effectiveness in multi-perforated plates for combustor liner effusion cooling. *Proceedings of ASME Turbo Expo*, (GT2013-94667), 2013.

[72] Jones, T. V. Theory for the use of foreign gas in simulating film cooling. *International Journal of Heat and Fluid Flow*, 20:349–354, 1999.

[73] Han, J. C. and Rallabandi, P. Turbine blade film cooling using PSP technique. *Frontiers in Heat and Mass Transfer*, 1, 2010.

[74] Charbonnier, D., Ott, P., Jonsson, M., Cottier, F., and Köbke, Th. Experimental and numerical study of the thermal performance of a film cooled turbine platform. *ASME Conference Proceedings*, (GT2009-60306):1027–1038, 2009.

[75] Kline, S. J. and McClintock, F. A. Describing uncertainties in single sample experiments. *Mechanical Engineering*, 75:3–8, Jan 1953.

[76] Goormans-Francke, C., Carabin, G., and Hirsch, C. Meah generation for conjugate heat transfer analysis of a cooled high pressure turbine stage. *Proceedings of ASME Turbo Expo*, (GT2008-50660), 2008.

[77] Crawford, M. E., Kays, W. M., and Moffat, R. J. Full coverage film-cooling-Part II: Heat transfer data and numerical simulation. *ASME J. Eng. Power*, 4(102):1006–1012, 1980.

[78] Miller, K. L. and Crawford, M. E. Numerical simulation of single, double, and multiple row film cooling effectiveness and heat transfer. *ASME Paper*, (84-GT-112), 1984.

[79] Heidmann, J. D. and Hunter, S. D. Coarse grid modeling of turbine film cooling flows using volumetric source terms. (NASA/TM-2001-210817), 2001.

[80] Burdet, A., Abhari, R. S., and Rose, M. G. Modeling of film cooling-Part II: Model for use in three-dimensional computational fluid dynamics. *ASME J. Turbomach.*, (129):221–231, 2005.

[81] Tartinville, B. and Hirsch, C. Modelling of film cooling for turbine blade design. *Proceedings of ASME Turbo Expo*, (GT2008-50136), 2008.

[82] auf dem Kampe, T. and Völker, S. A model for cylindrical hole film cooling-Part II: Model formulation, implementation and results. *ASME J. Turbomach*, (134), 2012.

[83] auf dem Kampe, T., Völker, S., and Zehe, F. A model for cylindrical hole film cooling-Part I: A correlation for jet-flow with application to film cooling. *ASME J. Turbomach*, (134), 2012.

[84] Andreini, A., Da Soghe, R., Facchini, F., Mazzei, L., Colantuoni, S., and Turrini, F. Local source based CFD modeling of effusion cooling holes: Validation and application to an actual combustor test case. *ASME J. Turbomach*, (136), 2014.

[85] Menter, F. R. Two-equation eddy-viscosity turbulence models for engineering applications. *AIAA Journal*, 32(8):1598–1605, 1994.

[86] Ansys, Inc. *ANSYS CFX-Solver Modeling Guide*. 2011.

[87] Andreini, A., Bonini, A., Carcasci, C., Facchini, B., Innocenti, L., and Ciani, A. Conjugate heat transfer calculations on GT rotor blade for industrial applications. Part I: equivalent internal fluid network setup. *Proceedings of ASME Turbo Expo*, GT2012-69846, 2012.

[88] Andreini, A., Bonini, A., Soghe, R. Da, Facchini, B., Ciani, A., and Innocenti, L. Conjugate heat transfer calculations on GT rotor blade for industrial applications. Part II: improvement of external flow modeling. *Proceedings of ASME Turbo Expo*, GT2012-69849, 2012.

[89] Hylton, L. D., Nirmalan, N. V., Sultanian, B. K., and Kaufman, R. M. The effects of leading edge and downstream film cooling on turbine vane heat transfer. Technical report, 1988.

[90] Hylton, L. D., Mihelc, M. S., Turner, E. R., Nealy, D. A., and York, R. E. Analytical and experimental evaluation of the heat transfer distribution over the surfaces of turbine vanes. Technical report, 1983.

[91] Hylton, L. D., Turner, E. R., Wilson, M. D., and M., Kaufman R. Turbine Vane External Heat Transfer. NASA CR-174827, 1985.

[92] Garg, V. K. and Gaugler, R. E. Effect of velocity and temperature distributionat the hole exit on film cooling of turbine blades. *Journal of Turbomachinery*, 119:347–351, 1997.

[93] Garg, V. K. and Gaugler, R. E. Leading edge film cooling effects on turbine blade heat transfer. Technical report, 1995.

[94] Laskowski, G. M., Ledezma, G. A., Tolpadi, A. K., and Ostrowski, M. C. Turbulence model assessment for conjugate heat transfer in a high pressure turbine vane model. *ASME Turbo Expo 2008*, 2008.

[95] Laskowski, G. M., Ledezma, G. A., Tolpadi, A. K., and Ostrowski, M. C. Heat transfer predictions of film cooled stationary turbine airfoils. *Proceedings of ASME Turbo Expo, GT2007-27497*, 2007.

[96] Mangani, L., Cerutti, M., Maritano, M., and Spel, M. Conjugate heat transfer analysis of nasa c3x film cooled vane with an object-oriented cfd code. *Proceedings of ASME Turbo Expo*, GT2010-23458: 413–422, 2008.

[97] Hall, E. J., Topp, D. A., Delaney, R. A., Walker, G. J., Hodson, H. P., and Shin, H.W. Aerodynamic/heat transfer analysis of discrete site film-cooled turbine airfoils. *AIAA*, 94-3070, 1994.

[98] Sarkar, S., Das, K., and Basu, D. Two-dimensional Navier-Stokes analysis of an internally cooled turbine blade. *Proc Instn Mech Engrs*, 214, Part A, 2000.

[99] Sarkar, S., Das, K., and Basu, D. Film cooling on a turbine guide vane: a numerical analysis with a multigrid technique. *Proc Instn Mech Engrs*, 215, Part A:39–53, 2001.

[100] Kays and Crawford. *Convective Heat and Mass Transfer*. McGraw-Hill, Second edition, 1980.

[101] Rohsenow, M. W., Hartnett, J. P., and Cho, Y. I. *Handbook of Heat Transfer*. McGraw-Hill Handbooks, 1998.

[102] York, W. D. and Leylek, J. H. Three-dimentional conjugate heat transfer simulation of an internally-cooled gas turbine vane. *Proceedings of ASME Turbo Expo*, GT2003-38551, 2003.

[103] Laskowski, G. M., Ledezma, G. A., Tolpadi, A. K., and Ostrowski, M. C. Cfd simulations and conjugate heat transfer analysis of a high pressure turbine vane utilizing different cooling configurations. *ISROMAC12-2008-20065*, 2008.

[104] Facchini, B., Magi, A., and Scotti Del Greco, A. Conjugate heat transfer simulation of a radially cooled gas turbine vane. *ASME Turbo Expo*, GT2004-54213, 2004.

[105] Seller, J. P. Gaseous film cooling with multiple injection stations. *AIAA Journal*, 1:2154–2156, 1963.

[106] Andrei, L., Facchini, B., Caciolli, G., Picchi, A., Tarchi, L., D'Ercole, M., Innocenti, L., and Russo, A. Film cooling adiabatic effectiveness measurements on first stage vanes in representative engine conditions. *Proceedings of ASME Turbo Expo*, (GT2014-26894), 2014.

[107] Luque, S. and Povey, T. A novel technique for assessing turbine cooling system performance. *Proceeding of ASME Turbo Expo*, (GT2009-60022), 2009.

[108] Kadotani, K. and Goldstein, R. J. Effect of mainstream variables on jets issuing from a row of inclined round holes. *ASME, Gas Turbine Conference and Products Show*, 1978.

[109] Goldstein, R. J., Eckert, E. R. G., and Ramsey, J. W. Film cooling with injection through holes: adiabatic wall temperature downstream of a circular hole. *J. Eng. Power*, (90):384–395, 1968.

[110] Blair, M. F. and Lander, R. D. New techniques for measuring film cooling effectiveness and heat transfer. *ASME, Thermophysics and Heat Transfer Conference*, 1974.

[111] Muska, J. F., Fish, R. W., and Suo, M. The additive nature of film cooling from rows of holes (for gas turbine airfoils). *ASME, Winter Annual Meeting*, 1975.

[112] Harrington, M., McWaters, M., Lemmon, C. A., and Thole, K. A. Full-coverage film cooling with short normal injection holes. *ASME J. Turbomach*, (123):798–805, 2001.

[113] Ceccherini, A., Facchini, B., Tarchi, L., and Toni, L. Combined effect of slot injection, effusion array and dilution hole on the cooling performance of a real combustor liner. *Proceedings of ASME Turbo Expo*, (GT2009-60047), 2009.

[114] Colburn, A. P. A Method of Correlating Forced Convection Heat Transfer Data and a Comparison With Liquid Friction. *Transactions of the AIChE*, 29:741–210, 1933.

[115] Bergman, T. L., Lavine, A. S., Incropera, F. P, and Dewitt, D. P. *Foundamentals of Heat and Mass Transfer*. John Wiley and Sons, 2011.

[116] Necati Ozisik, M. *Heat Transfer. A basic Approach*. McGraw-Hill, 1985.

[117] Nusselt, W. Der Warmeaustausch Zwischen Wand and Wasser im Rhor. *Forsch. Geb. Ingenieurwes*, page 309, 1931.

[118] Sieder, E. N. and Tate, G. E. Heat Transfer and Pressure Drop of Liquid in Tubes. *ind. Eng. Chem.*, 28:1429–1435, 1936.

[119] Petukhov, B. S. Heat Transfer and Friction in Turbulent Pipe Flow with Variable Physical Properties. pages 504–564, 1970.

[120] Kreith, F., Manglik, R., and Bohn, M. *Principles of Heat Transfer*. Cengage Learning, 2010.